Fall 2014

Droplet behavior on superhydrophobic surfaces: Interfaces, interactions, and transport

Susmita Dash
Purdue University

Graduate School Form 30
(Revised 08/14)

PURDUE UNIVERSITY
GRADUATE SCHOOL
Thesis/Dissertation Acceptance

This is to certify that the thesis/dissertation prepared

By Susmita Dash

Entitled

DROPLET BEHAVIOR ON SUPERHYDROPHOBIC SURFACES: INTERFACES, INTERACTIONS, AND TRANSPORT

For the degree of Doctor of Philosophy

Is approved by the final examining committee:

Suresh V. Garimella

Jong Hyun Choi

Jayathi Murthy

Jeffrey Youngblood

To the best of my knowledge and as understood by the student in the Thesis/Dissertation Agreement, Publication Delay, and Certification/Disclaimer (Graduate School Form 32), this thesis/dissertation adheres to the provisions of Purdue University's "Policy on Integrity in Research" and the use of copyrighted material.

Suresh V. Garimella

Approved by Major Professor(s): _____

_____

Approved by: Ganesh Subbarayan 10/10/2014

Head of the Department Graduate Program Date

DROPLET BEHAVIOR ON SUPERHYDROPHOBIC SURFACES: INTERFACES, INTERACTIONS, AND TRANSPORT

A Dissertation

Submitted to the Faculty

of

Purdue University

by

Susmita Dash

In Partial Fulfillment of the

Requirements for the Degree

of

Doctor of Philosophy

December 2014

Purdue University

West Lafayette, Indiana

To Nana, Maa and Pratikash

ACKNOWLEDGEMENTS

I would like to thank my advisor and mentor, Prof. Suresh V. Garimella for his support and motivation during the course of my graduate studies. I am grateful to him for his invaluable guidance, encouragement, and his confidence in me. I have learnt a lot from him, and will seek to incorporate them as I move ahead. I am thankful to my committee members, Prof. Jayathi Murthy, Prof. Jong Hyun Choi, and Prof. Jeffrey Youngblood for their comments and suggestions for this dissertation work. Prof. Murthy has been a source of inspiration for me.

I extend my gratitude towards the wonderful faculty members in the School of Mechanical Engineering. I appreciate the help of staff at Birck Nanotechnology Center, particularly, Mr. William Sheldon. I am thankful to my lab members, who are ever helpful, and nice. Special thanks to Dr. Justin Weibel, Dr. Karthik Bodla, Dr. Zhenhai Pan, Dr. Xuemei Chen, Dr. Niru Kumari, Dr. Ravi Annapragada, Dr. Tim Persoons, Niki Ritchey, Mercy Dicuangco, Aditya Chandramohan, Mathew Rau, and Ravi Patel. The friendly environment in the research group, and insightful discussions provided a positive ambience for research work.

I thank my friends, Suchi, Aarti, Prabhakar, Nikhil, Arun, Poornima, Kayal, Romila, Kritika, Neha, Gaurav, Prasoon, Sugi, Vinod and others who made my entire stay at Purdue so memorable. I would not have achieved what I have without the hard work,

and blessings of my parents, teachers, and unconditional love and support of my husband, and my sister and brother. I am thankful to my in-laws for their support and blessings.

TABLE OF CONTENTS

Page

Page

Page

LIST OF TABLES

LIST OF FIGURES

Figure Page

Figure Page

Figure Page

Figure Page

Figure Page

Appendix Figure Page

ABSTRACT

Dash, Susmita. Ph.D., Purdue University, December 2014. Droplet Behavior on Superhydrophobic Surfaces: Interfaces, Interactions, and Transport. Major Professor: Suresh V. Garimella, School of Mechanical Engineering.

The primary objective of the present work is to study droplet dynamics on smooth hydrophobic and textured superhydrophobic surfaces, and to understand the dependence of interfacial interaction mechanisms on surface morphology.

A detailed understanding of the dynamics of droplet response to an applied electric field is essential for implementation of electrowetting techniques in various devices. In the first part of the thesis, a systematic study of the transient response in terms of contact angle and contact radius of a sessile droplet on a smooth hydrophobic surface under electrical actuation is presented. A scaling analysis predicts the response time of a droplet during step actuation. It is shown that during time-varying electrical actuation of a droplet, in addition to the primary frequency response at the electrical forcing frequency, the droplet oscillation exhibits sub-harmonic oscillation at half the forcing frequency.

The remaining part of the thesis focuses on the design, fabrication and characterization of superhydrophobic surfaces, and droplet behavior on such surfaces. A simple yet highly effective concept of fabricating hierarchical structured surfaces using a single-step deep reactive ion etch process is proposed. The surfaces show enhanced anti-wetting characteristics, and lower contact angle hysteresis compared to single-roughness

surfaces. A novel hybrid surface morphology incorporating communicating and non-communicating air gaps is proposed to enhance capillary pressure. The pressure balance during droplet impingement indicates that the effective water hammer is dependent on the surface morphology, and is significantly lower compared to that on smooth surfaces.

The last part of the thesis includes evaporative phase change on flat and textured surfaces. An understanding of the evaporation characteristics of the droplet, and accompanying convection flow field on hydrophobic and superhydrophobic surfaces is important to several applications. In this dissertation, droplet evaporation characteristics on unheated and heated hydrophobic and superhydrophobic surfaces with negligible contact angle hysteresis are investigated systematically. A vapor-diffusion-only model is shown to overpredict the rate of evaporation on superhydrophobic surfaces, and the disparity increases with substrate heating. The evaporation characteristics are explained in terms of the evaporative cooling, and vapor buoyancy induced convection.

Improved understanding of the convective flow mechanism inside an evaporating droplet can assist in non-intrusive particle manipulation inside a micro-droplet. The recirculating convective flow field inside a water droplet evaporating on hydrophobic and superhydrophobic surfaces is attributed to the thermal buoyancy induced convection. The flow pattern inside the droplet enables understanding of the dependence of flow behavior on the nature of the substrate. High recirculating flow velocity in droplets evaporating on superhydrophobic surfaces is proposed to enable ‘on-the-spot’ mixing in droplets for microfluidics application.

CHAPTER 1. INTRODUCTION

Microfluidics-based devices have applications in diverse areas including 'lab on a chip' systems, biomedical devices and MEMS-based sensors and detectors. Handling fluids at the microscale presents significant challenges, as conventional fluid handling techniques do not apply well to the microscale. Electrowetting-based control for the actuation of droplets has received significant recent attention because of its lack of moving parts, low power consumption and amenability to on-chip integration. Understanding of the transient response of a droplet when subject to electrical actuation is important for accurate estimation of response time of the devices implementing electrical actuation of droplet.

At length scales on the order of micro- and nano- meter, surface tension forces surpass the body forces, and play a significant role in resisting fluid flow. One approach to mitigate this resistance is designing special surfaces that reduce the solid-liquid contact, and minimize surface energy. These special surfaces are termed as 'superhydrophobic surfaces'. Devising cost efficient and scalable methods for fabricating superhydrophobic surfaces is important for widespread applications of these surfaces. Robust superhydrophobic surfaces should be designed so that they retain superhydrophobicity under dynamics conditions. Superhydrophobic surfaces, being structured surfaces exhibit different evaporation characteristics compared to smooth surfaces. The exact nature of

flow behavior in a liquid during evaporation on such surfaces is not well-studied and requires careful attention.

1.1 Electrowetting-Induced Droplet Actuation

Electrowetting on a dielectric (EWOD) refers to electrowetting on a conducting surface separated from the droplet by an insulating layer, either using AC or DC actuation voltages. Microscale manipulation of droplets by electrical actuation has significant applications in the areas of microfluidics and lab-on-chip devices. Electrowetting-based control for the actuation of droplets has received significant recent attention because of its lack of moving parts, low power consumption and amenability to on-chip integration. The steady-state contact angle of a droplet under DC actuation has been well studied and has been shown to follow Lippmann's equation [1] at lower voltages. Most of the available literature on DC EW has targeted prediction of the steady-state contact angle, while the transient response of the droplet is less well understood. Detailed analysis of the transient response of the droplet under DC actuation is necessary for regulating the response time of EW-based devices. The flow field generated during droplet oscillation under actuation at low AC frequencies can be utilized for enhancing the mixing in a droplet which has potential biomedical applications. The oscillation of the contact line of the droplet has been employed to avoid the pinning of the contact line, as will be explained later in this report. The wide range of applications of the oscillation induced by time-varying electrical actuation necessitates careful investigation of the oscillation dynamics.

1.2 Superhydrophobic Surfaces

Superhydrophobic surfaces refer to surfaces that repel water. These surfaces are characterized by a very high contact angle (> 150 deg), and allow droplets to roll off at a very low inclination angle. A common example of a superhydrophobic surface found in nature is the lotus leaf. Figure 1.1 shows a SEM image of the lotus leaf [2]. The hierarchical surface morphology and the paraffin layer covering the surface of the lotus leaves make them repel water and thus remain dry [2, 3]. These surfaces occurring in nature have been the motivation for extensive research towards the design and fabrication of artificial superhydrophobic surfaces.

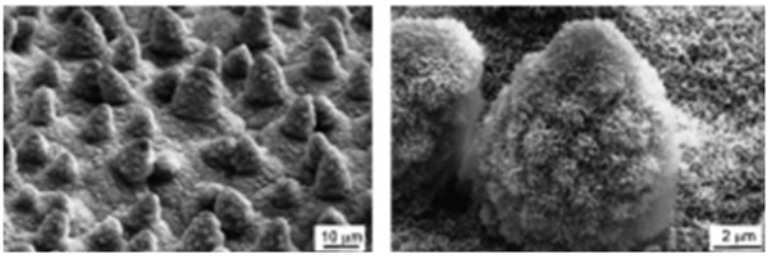

Figure 1.1. SEM images of Lotus (*Nelumbo nucifera*) leaf surface consisting of microstructure formed by papillose epidermal cells covered with epicuticular wax tubules on surface, which create a nanostructure [2].

The contact angle of a liquid droplet on a surface is determined by the surface energy as well as the surface morphology [4]. The morphology of the surface determines whether a droplet will remain in a Cassie (non-wetting) or a Wenzel (wetting) state (Figure 1.2a and Figure 1.2b respectively). Superhydrophobicity may be imparted to a surface by carefully engineering the surface topology and controlling the ratio of areas of the top surface of the pillars to the total base surface (ϕ), thereby controlling the extent of the liquid-air interface [5]. This property of superhydrophobic surfaces helps reduce the

drag force offered to fluid transport, and is being studied extensively for microchannel-based and other applications [6]. These surfaces have a wide range of applications, for example in water-proof wind shields, resisting icing, corrosion, and microarray biochips, owing to the high contact angle and extremely low roll-off angles.

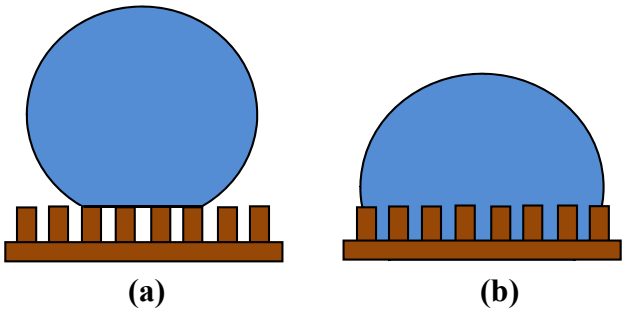

Figure 1.2. Schematic illustration of droplet wetting states: (a) Cassie, and b) Wenzel.

Very high contact angles may be obtained by increasing the liquid-air interfacial area when a droplet is placed on the surface, *i.e.*, by increasing the air gap between the roughness elements. However, larger air gaps result in reduced capillary pressure; with a corresponding reduction in the external actuation force required for the Cassie-to-Wenzel transition. The transition to a Wenzel state due to external forces displaces the air gaps with liquid and significantly increases the drag force incurred in transporting a droplet on the surface. Surface designs must therefore be optimized such that they sustain high contact angles with low contact angle hysteresis, without compromising the anti-wetting property of the surfaces.

Higher capillary pressures can be achieved by scaling down the feature size of the roughness elements on the surface, as well as by employing hierarchical roughness structures. The challenge is to design surfaces that enhance the capillary pressure at the

level of single roughness elements for a particular feature size while preserving a high contact angle. This will be addressed in the present work.

1.3 Evaporation on Superhydrophobic Surfaces

Droplet evaporation is relevant to a variety of applications including inkjet printing [7], hot spot cooling [8, 9], surface patterning [10], droplet-based microfluidics [11], paints [12, 13], and DNA mapping [14, 15]. The nature of deposition of solute particles in an evaporating droplet is dependent on the evaporation dynamics, which in turn depends on the wettability and roughness of the surface. Droplet evaporation characteristics depend on surface wettability [16], contact angle hysteresis (CAH) [17], and surface roughness [18]. An understanding of the evaporation characteristics of a droplet in terms of the rate of evaporation, localized solute-deposition on a substrate, flow pattern in the droplet, and variation of contact angle (CA) and contact radius (CR) is necessary for the design of practical droplet-based applications.

Although droplet evaporation on smooth surfaces has been widely studied with liquids of different properties, and some work has been reported on superhydrophobic surfaces with very high contact angle hysteresis, droplet evaporation on superhydrophobic surfaces with negligible contact angle hysteresis (CAH) with and without substrate heating has not received much attention. Recently, evaporation-based solute localization was proposed on superhydrophobic surfaces [19]. Potential application of droplet evaporation on superhydrophobic surfaces necessitates understanding of dynamics of evaporation on superhydrophobic surfaces.

1.4 Flow Behavior in Droplets Evaporating on Hydrophobic and Superhydrophobic Surfaces

The non-uniform evaporation rate along the interface of a sessile droplet, and nature of the substrate and the liquid droplet affect the internal fluid convection inside an evaporating droplet. The fluid convection influences the rate of evaporation, and the evaporative particle deposition in a sessile droplet. Prediction and control of evaporation-driven convection patterns, and the resulting spatial distribution of particulate deposits, during droplet evaporation is crucial for colloidal crystallization [20], ink jet printing [21], paint drying [12,13], nanofabrication [22,23], sensors [24,19], and bioengineered tissues [25]. Improved understanding of the physics of flow inside an evaporating sessile droplet and its dependence on the substrate properties can assist in the development of non-intrusive methods for manipulating particles inside micro-droplets to control deposit morphologies.

1.5 Objectives

The objective of this dissertation is to study the dynamics of droplets on a smooth hydrophobic surface under electrical actuation, and to explore various aspects of the robustness of superhydrophobic surfaces and the droplet behavior on such surfaces. The primary objectives and the approach pursued are as follows:

1. Understanding the transient dynamics of microliter-sized droplets under electrowetting-induced actuation. The response under step actuation and time-varying actuation is studied. The characteristic time scale for droplet response to electrical actuation is predicted based on experimental observations and theoretical

analysis. This data is useful for devices which rely on electrowetting of liquid drops as the working principle, such as liquid-based displays.

2. Devising simple methods for fabrication of hierarchical superhydrophobic surfaces. Hierarchical roughness surfaces comprise two levels of roughness, usually attained using multiple fabrication steps. A methodology for fabrication of hierarchical surfaces using a single step is proposed. The benefits of using hierarchical surfaces compared to single roughness surfaces are experimentally demonstrated. Careful experiments to determine the roll-off angle, contact angle hysteresis, characteristics of droplet evaporation and impact are carried out on the superhydrophobic surfaces.
3. Investigation of surface designs that maximize superhydrophobicity by enhancing the anti-wetting pressure. Hollow pillars which incorporate both communicating and non-communicating air gaps are analytically shown to exhibit higher capillary (or non-wetting) pressure compared to solid pillars with only communicating air gaps and are fabricated. Based on pressure based transitions during droplet impingement tests, the water hammer pressure is predicted. The mechanics of water hammer pressure on superhydrophobic surfaces is explained. The results can aid in more accurate estimation of the robustness of air gaps of surfaces subject to liquid impact.
4. Study of evaporation dynamics of droplets on unheated and heated superhydrophobic surface that display very high contact angle (CA ~ 160 deg) and negligible contact angle hysteresis (< 1 deg). The rate of evaporation on a superhydrophobic surface is shown to be underpredicted by the isothermal vapor-diffusion model, across all droplet volumes. The disparity increases with increase in substrate temperature. A simple diffusion model taking into account the thermal conduction through the

droplet is used to understand the transport phenomena in play during droplet evaporation.

5. Physics-based analysis and quantification of the recirculating flow field inside a sessile droplet evaporating on a heated smooth hydrophobic surface and textured superhydrophobic surface using Particle Image Velocimetry. The dependence of the convective flow behavior inside the droplet on the surface wettability is determined. The evaporative particle localization on smooth hydrophobic surface and superhydrophobic surface is explained in terms of the mode of evaporation, and flow field inside the droplet. Evaporation-induced convection inside a sessile droplet is shown to be suitable for droplet mixing applications.

1.6 Organization of the Thesis

The report is organized as follows. Chapter 2 contains a review of the literature in the areas of electrowetting-based actuation on smooth and structured surfaces, design and fabrication of superhydrophobic surfaces, and the various applications. The transient response of a droplet to an applied electrical actuation force with step and time-varying actuation is presented in Chapter 3. Chapter 4 discusses the fabrication of hierarchical superhydrophobic surfaces using a single-step methodology. The surface is characterized in terms of dynamic pressure, evaporation properties of droplets on the surfaces. A novel design of hybrid superhydrophobic surfaces implementing both communicating and non-communicating air gaps so as to enhance anti-wetting pressure is discussed in Chapter 5, followed by analysis of pressure balance during droplet impingement. Chapter 6 presents the diffusion-driven evaporation on unheated and heated, hydrophobic and superhydrophobic surfaces with a constant contact angle mode, and discusses the unique

properties that contrast with hydrophilic surfaces. In Chapter 7, an evaporative flow field visualization and analysis is reported for droplets evaporating on heated hydrophobic and superhydrophobic substrates. A summary of the present work and avenues for future research are provided in Chapter 8

CHAPTER 2. LITERATURE SURVEY

2.1 Electrical Actuation of Liquid Droplets

Electrical actuation serves as a viable option for droplet manipulation in microscale devices [1]. Droplet transport, breakup and merging using electrowetting-based actuation have been demonstrated for lab-on-chip applications in the literature [26-30]. Other key applications that exploit enhanced control of droplet morphology include electrowetting-based optics [31] and liquid displays [32]. Electrowetting (EW) also has application in altering the wetting characteristics of a surface [33-35]. The use of EW in conjunction with changes in surface morphology provides enhanced control of droplet wetting states. The relative stabilities of the Cassie and the Wenzel states on rough surfaces may be manipulated through EW [34, 35].

The steady-state contact angle of a droplet under DC actuation has been well studied and has been shown to follow Lippmann's equation [1] at lower voltages. Saturation of the contact angle occurs when the applied voltage exceeds a certain value depending on the liquid and dielectric properties [36,37]. Within the working range of actuation voltage, DC electrowetting has been employed in the design of optical displays [38]. In recent studies, the unsteady motion of a sessile droplet under DC actuation has been reported in terms of the contact radius [39,40].

Electrowetting using AC actuation voltages has also drawn attention [41-43]. The main advantages of using AC over DC voltage include reduction of the chemical reactions in the droplet [28] and decrease in the contact-angle hysteresis [44]. Kumar *et al*. [42] studied the contact angle variation of aqueous salt droplets under an AC voltage. Time varying electrical actuation of a droplet can be implemented in enhancing mixing in a droplet for lab on chip applications. Mugele *et al*. [45] studied the frequency dependence of the internal flow field in a droplet using tracer particle tracking. Paik *et al*. [46] studied the mixing caused by droplet motion between parallel plates, while Miraghaie *et al*. [47] focused on the shape oscillations to study the internal mixing pattern. Mixing inside a droplet can also be effected by changing the droplet morphology [48]: the droplet is initially in contact with a top electrode when not actuated and detaches from this electrode when actuated. Upon detachment, the droplet is no longer actuated and returns to its original shape at which time it touches the top electrode again. Repetition of this cycle can cause continuous droplet oscillation. Recently, Sen and Kim [40] reported contact angle and radius variations at lower AC frequencies but the experiments were performed for a single actuation voltage. Ko *et al.* [49] used particle image velocimetry to visualize the flow field inside a conducting droplet oscillating under the influence of an AC voltage and attributed the flow at low frequencies to the oscillation of the contact line.

In summary, electrical actuation of droplet is a powerful tool for manipulation of droplet shape, and for facilitating droplet motion at small length scales. Inspite of the vast literature on the topic, there are fundamental questions regarding droplet dynamics during incipience of electrowetting induced motion that need careful study. Investigation

of physical parameters of a droplet during time-varying actuation electrical actuation can provide significant insight into the induced mixing in the droplet.

2.2 Hierarchical Superhydrophobic Surfaces

The development of superhydrophobic surfaces has attracted significant attention over the past decade because their promise in applications such as hydrophobic windshields, microfluidics-based technologies such as lab-on-chip devices [50,51,52], microelectromechanical systems (MEMS), water-proof clothing [53], and ice-repellent surfaces [54]. The ability of superhydrophobic surfaces to repel water and provide minimum drag resistance is contingent on the retention of air gaps; i.e., the Cassie state must be sustained. Dynamic switching from the Cassie to the Wenzel state may be attained by means of electrical actuation [34, 35,-56, 57], application of pressure on the droplet, or dropping the droplet from a height [58].

Superhydrophobic surfaces are non-wetting surfaces characterized by high contact angles (> 150 deg), a low sliding angle, and low contact angle hysteresis (CAH) [59-62]. A large droplet contact angle is not the sole criterion to characterize the superhydrophobicity of a surface. It is important to design surfaces such that they are also robust enough to prevent impalement by droplets. A higher capillary pressure enhances the robustness of the air gap between the roughness elements of a surface [63]. Sub-micron scale roughness coupled hierarchically with microscale roughness can render a surface superhydrophobic and impart improved non-wetting properties relative to single-tier roughness. Hierarchical roughness is commonly encountered in nature; the extreme water-repellent characteristic of lotus leaves arises from a double-roughness structure consisting of nanoscale waxes on microscale bumps [3].

Surfaces with such extreme hydrophobicity have important applications in the development of artificial self-cleaning surfaces and water-proof clothing [64], and offer a wide range of promising applications including their use in microfluidic-based technologies such as lab-on-chip devices, microelectromechanical systems (MEMS), and microarray biochips. An important heat transfer application lies in the development of surfaces for dropwise condensation. Dropwise condensation is desirable since the associated heat transfer coefficient is an order of magnitude higher than that with filmwise condensation. Dropwise condensation is, however, not readily achieved on single-tier roughness structures [65]. It was recently demonstrated that condensation on hierarchical roughness structures leads to condensation in the form of drops [66]. Since hydrophobic surfaces resist the formation of a liquid film, surface corrosion is also mitigated.

The wide range of applications of hierarchical hydrophobic surfaces has encouraged active research in this field. Different methods of fabricating such hierarchical surfaces [59, 67] to attain superhydrophobicity have been demonstrated in the literature. Fabrication of double-roughness structures typically involves the fabrication of the larger features on a substrate (by standard lithography methods) followed by the deposition of smaller roughness elements on these larger features [59, 67, 68]. Efforts at fabricating and testing robust superhydrophobic surfaces which can be easily fabricated and commercially used continue to be reported.

In summary, hierarchical superhydrophobic surfaces have their applications in numerous areas. The challenge is devising scalable and cost effective methods of making such surfaces, which requires significant research efforts.

2.3 Hybrid Surface Design for Robust Superhydrophobicity

A high contact angle is not the sole criterion that characterizes the superhydrophobicity of a surface. It is important to design surfaces that are sufficiently robust to prevent impalement by droplets when subjected to external force. A higher capillary pressure within the interstices of roughness elements on a surface enhances the stability of the air gaps therein [63,69]. Higher capillary pressures can be achieved by scaling down the feature size of the roughness elements on the surface, as well as by employing hierarchical roughness structures [70,71]. However, scaling down feature size (thinner pillars) may compromise with mechanical robustness of the structures, and shorter feature sizes render the surface susceptible to a wetting transition, since the hanging curvature allows a droplet to more readily contact the bottom surface [72]. The challenge, therefore, is to design surfaces that enhance the capillary pressure at the level of single roughness elements for a particular feature size. Park *et al*. [73] reported the use of a cylindrical nanoshell array to generate a superhydrophobic surface, even without the use of a hydrophobic coating. Bahadur and Garimella [74] demonstrated that structured surfaces with non-communicating craters offered greater resistance to electrowetting-induced droplet transition compared to equivalent communicating pillared structures.

Analytical and experimental research has corroborated the strong effect of surface morphology on the impact behavior of a water droplet and its ability to bounce off the surface [75-78]. Bhushan *et al.* [59] demonstrated improved water-repellence on hierarchical surfaces as compared to single roughness elements. Based on the Laplace pressure and the Bernoulli pressure, they formulated an expression for the critical velocity of the droplet beyond which it transitions to a Wenzel state on textured surfaces.

Deng *et al.* [63] developed a pressure-balance model to arrive at a condition for droplet infiltration into the air gaps in the surface structures. They accounted for the water hammer pressure that acts on the surface during droplet impingement. Denser textured surfaces were expected to provide greater capillary pressure and superior resistance to Wenzel wetting of impacting droplets.

The water hammer pressure was first proposed by Cook [79] as $P_{WH} = \rho c V$ where ρ is the density of the impinging droplet, c the speed of sound in the liquid, and V the velocity of impingement. This expression was validated by Engel [80] through droplet impingement experiments on different substrates and by the use of a Schlieren technique to determine the time dependence of the impact force. He proposed a correction to Cook's expression: $P_{WH} = k\rho c V$, where the coefficient k varies depending on the type of the substrate and impact velocity. While the water hammer pressure is relatively well defined for a flat, rigid surface [80,81], it is less well understood during droplet impact on superhydrophobic surfaces.

In summary, it is important to ensure sufficient anti-wetting pressure so that the superhydrophobicity of the surface is retained under dynamic conditions. This can be attained by exploring alternate surface designs that enhance capillary pressure. Accurate estimation of the pressure based Cassie-Wenzel transitions requires knowledge of the coefficient of the water hammer pressure, which has not been studied for superhydrophobic surfaces in the literature.

2.4 Droplet Evaporation Dynamics on Hydrophobic and Superhydrophobic Surfaces

A liquid droplet suspended in air evaporates uniformly at a rate proportional to its radius, and its size continuously diminishes [82]. Evaporation characteristics of a sessile droplet placed on a substrate, on the other hand, are influenced by the wettability as well as the roughness of the substrate. Picknett and Bexon [82] were among the first researchers to study the evaporation of a droplet placed on a substrate in still air. They identified two modes of evaporation of a droplet resting on a smooth homogeneous surface, namely, the constant contact angle (CCA) mode and the constant contact radius (CCR) mode. The rate of evaporation in both modes of evaporation was reported to be dependent on the contact radius and the contact angle of the droplet. A theoretical solution for the evaporation rate was derived based on a similarity between the diffusive concentration field around a droplet and the electrostatic potential field of a conducting body of the same size and shape as the droplet [82]. Evaporation was reported to occur in a CCR mode until the droplet reached its receding contact angle, at which point it continued in a CCA mode [82]. The duration of each phase varied depending upon the substrate and liquid used [82].

The interplay between factors such as interface temperature and saturated vapor concentration coupling, conduction through the substrate, droplet, and gas phases, convection in the liquid and gas domains, and the spherical-cap shape of the droplet, all complicate the determination of an exact solution for droplet evaporation rate. Most models in the literature treat evaporation as being induced only by vapor diffusion under isothermal conditions, subject to several simplifications in terms of the evaporative flux [16, 83, 84]. McHale *et al.* [83] concluded that the evaporation rate on a hydrophobic

surface is proportional to the droplet height during evaporation and that the mode of evaporation is determined by the initial contact angle of the droplet. Yu *et al.* [84] also reported the droplet evaporation rate on a hydrophobic surface to be proportional to the droplet height. Deegan [12] and Popov [13] drew attention to the non-uniformity of evaporative flux along the droplet surface. Popov [13] developed a closed-form solution to describe the rate of evaporation by vapor diffusion valid over the entire range of contact angles. In recent studies, the substrate conductivity has been identified as being important in determining the evaporation rate of pinned sessile droplets [85,86]. Dunn *et al.* [86] proposed a model that included the effect of substrate thermal conductivity for a pinned sessile droplet with very low contact angle. Although the model could predict evaporation rates of volatile droplets, it under-predicted the evaporation rate for a water droplet.

Evaporation on an 'ideal' surface with no surface deformities is expected to occur in a CCA mode. However, molecular-scale interactions between the liquid and substrate, as well as inherent roughness/deformities of real surfaces, induce contact angle hysteresis which inhibits the CCA mode of evaporation. The transient evaporation of a droplet is affected by the initial contact angle of the droplet [13] as well as the contact angle hysteresis [17]. Most prior studies have focused on droplet evaporation in a CCR mode [9,12,13,87]. Deegan *et al.* [88] suggested that the peripheral deposition of suspended particles in a droplet by the 'coffee-ring' effect is attributable to a pinned contact line during evaporation and a non-uniform evaporation flux on the droplet surface (concentrated near the contact line). In many applications including inkjet printing [7],

spotting of biofluids [89], and surface coating [90], the highly inhomogeneous solute deposition resulting from capillary-induced flow [12] is undesirable.

Methods such as AC electrowetting [91] have been demonstrated to suppress this effect. One other way to manipulate the deposition of particles suspended in sessile droplets may be by employing a superhydrophobic surface with low contact angle hysteresis. De Angelis *et al.* [19] demonstrated the use of superhydrophobic surfaces combined with plasmonic nanostructures to allow molecule detection in femtomolar-concentration solutions by localizing the molecule in a specific position. The droplet in this case remained in the Cassie or non-wetted state during most of the period of evaporation. Such application in bio-sensors requires a detailed understanding of the droplet evaporation dynamics on superhydrophobic surfaces as well as an accurate estimation of the total time of evaporation.

McHale *et al.* [92] and Dash *et al.* [71] reported droplet evaporation on a superhydrophobic surface to follow three distinct phases: Constant contact area mode, constant contact angle mode in which the contact angle remains almost fixed and the droplet interface slides, and mixed mode in which both the contact angle and contact radius change. An initial high droplet CA on a surface was earlier reported to be the criterion for droplet evaporation in the CCA mode [93, 94]. However, droplet evaporation on superhydrophobic lotus leaves and biomimetic polymer surfaces, in spite of exhibiting a high contact angle (~ 150 deg), has been reported to follow the constant contact area mode [95]. Indeed, the mode of evaporation of a droplet has been shown to depend instead on the contact angle hysteresis of the surface rather than the initial contact angle of the droplet [17]. The mode of evaporation is instrumental in determining the

various physical parameters of the droplet (height, contact radius, and contact angle) during evaporation, the rate of mass loss, and the total time for evaporation.

The vapor diffusion model proposed by Popov [13] has been shown to predict the evaporation dynamics of droplets on hydrophilic substrates [12], hydrophobic substrates with sliding [96] and pinned [97] contact lines, and superhydrophobic substrates with pinned contact line [98]. However, the diffusion-only model of Popov [13] has not been experimentally validated on superhydrophobic surfaces with negligible contact angle hysteresis. Recently, Erbil [99] presented a comprehensive review of droplet evaporation on different surfaces and emphasized the need to study droplet evaporation on relatively unexplored superhydrophobic surfaces.

A survey of the literature indicates that studies concerning the concentration of suspended particles by means of droplet evaporation on superhydrophobic surfaces rely on diffusion-driven evaporation from an unheated substrate [19,100]. This results in long evaporation times (on the order of thousands of seconds). Applications such as molecule detection in biosensors [19] require a detailed understanding of the droplet evaporation dynamics on superhydrophobic surfaces, *viz.*, the rate of evaporation and transient variation of contact angle or radius. Detection time can be reduced significantly upon the application of external heat to the droplet, but requires characterization of the evaporation characteristics (*e.g.*, evaporation rate and transient droplet geometry) under heated conditions.

In summary, although droplet evaporation on smooth surfaces has been widely studied with liquids of different properties, and some work has been reported on superhydrophobic surfaces with very high contact angle hysteresis, droplet evaporation

on superhydrophobic surfaces with negligible contact angle hysteresis (CAH) has not received much attention. There has been limited investigation of the effect of substrate heating on the evaporation characteristics of droplets with a sliding contact line on hydrophobic and superhydrophobic substrates in the literature. The potential applications of droplet evaporation on superhydrophobic surfaces necessitate knowledge of the physics of evaporation dynamics on such surfaces.

2.5 Flow Behavior inside Droplet Evaporating on Hydrophobic and Superhydrophobic Surfaces

For hydrophilic surfaces, a non-uniform evaporative flux along the surface of the droplet with the highest value at the contact line, in combination with a pinned contact line, leads to an outward capillary flow within the droplet [12] and a ring-like deposition pattern. The second flow pattern that may be observed is driven by recirculating Marangoni convection caused by a surface tension gradient along the droplet interface due to a non-uniform temperature [101,102]. The direction of the interface temperature gradient, which determines the direction of flow, depends on fluid type, size, and droplet contact angle [12], as well as the ratio of substrate-to-liquid thermal conductivity [103] and the shape of the particles inside the droplet [104]. While Marangoni convection has been theoretically predicted to occur in several fluids, its realization in water has not been consistently validated in experiments [101,105,106]. Marangoni flow-based recirculation in an organic liquid droplet was reported to arrest peripheral deposition, instead causing a localized deposition pattern [101,105,107]. Besides these capillary- and Marangoni-driven flows, a third possible kind of flow in the droplet is buoyancy-driven Rayleigh-Benard convection resulting from a temperature- or concentration-induced density

gradient inside the droplet [108]. Solutal density-driven Rayleigh convection in a binary mixture has been reported in several studies [108,109,110]. An oscillatory behavior was observed in the convection pattern when buoyancy forces affected Marangoni convection; this was explained by the coupling between interfacial temperature gradients and the flow within the liquid [111].

The recirculating flow inside droplets can be used as a means for mixing and manipulating particles. Efficient mixing is extremely important in various microfluidic devices for biological and chemical applications [112]. However, the low Reynolds numbers characteristic of microfluidic flows [48] renders mixing of particles in a microscale droplet challenging. In lab-on-a-chip devices, the rate of chemical reactions is often limited by the mass diffusion. Different mechanisms that achieve fast mixing by promoting chaotic advection include flow through irregularly winding channels [113], magnetic stirring [114], and acoustic excitation [115]. Obtaining 'on-the-spot' mixing in droplets, which is of significant importance to digital microfluidic systems, is even more challenging. Convection arising from electrowetting-induced oscillation of a droplet was recently reported to enhance mixing [45]. Manipulation of the recirculating flow field in an evaporating droplet through modification of the surface wetting properties has not been investigated to date as a method for enhancing mixing.

A majority of the studies investigating the flow pattern inside a droplet and the resulting deposition have been restricted to hydrophilic substrates featuring a pinned contact line. The literature related to droplet evaporation on hydrophobic or superhydrophobic surfaces, for which a minimal contact angle hysteresis causes evaporation to predominantly occur in a constant contact angle mode, is limited and

includes the studies done as a part of the present thesis. Studies have indicated a localized, central deposit being formed during evaporation on hydrophobic surfaces [116], a phenomenon that has been employed in aptasensors for protein detection [24]. Localized deposition was reported during evaporation on superhydrophobic surfaces [116]; tuning of surface geometry achieved a minimum deposit size as small as 0.9% of the initial droplet base area [116]. A quantitative estimate of the internal flow characteristics, and identification of the governing mechanism that establishes the flow field inside a droplet evaporating on non-wetting surfaces, are needed to understand the relationship with the localized deposition pattern realized. Tam *et al*. [117] derived an analytical solution for droplet evaporation on a superhydrophobic surface based on the assumption of Marangoni convection in the droplet. The governing mechanism that establishes the flow field inside a droplet evaporating on a heated hydrophobic surface has not yet been experimentally investigated.

In summary, the goal of the present work is to determine qualitatively as well as quantitatively the flow behavior inside droplets evaporating on smooth hydrophobic and superhydrophobic substrates.

CHAPTER 3. FREQUENCY-DEPENDENT TRANSIENT RESPONSE OF AN OSCILLATING ELECTRICALLY ACTUATED DROPLET

This chapter reports an investigation of the transient nature of the step response of droplets as well as the important characteristics of the frequency response of the droplet over a range of applied voltages. The first set of experiments maps out the transient response of a millimeter-sized sessile droplet under DC actuation. The response of the droplet, in terms of contact angle (CA) and contact radius (CR) measurements before it attains a steady-state profile, is studied and the characteristic time scale of a droplet during step response analyzed. Droplet dynamics under low-frequency AC actuation are then investigated in detail in terms of the time-varying CR and CA with the root-mean-square voltage (V_{rms}) varying from 40 V to 80 V and frequencies ranging from 5 Hz to 200 Hz. The characteristics of the droplet behavior upon contact angle saturation are discussed. The experimental observations map out the different modes of oscillation and also identify the distinct droplet dynamics corresponding to each intermediate frequency regime between two consecutive oscillation modes. The principal as well as the sub-harmonic frequency response of the droplet are identified. The sub-harmonic response is explained in terms of the parametric electrowetting force that governs the droplet oscillation. The material presented in this chapter was published in *Journal of Micromechanics and Microengineering* (**22**(7), 075004, 2012) [118].

3.1 Experimental Setup

A schematic diagram of the experimental setup used for droplet actuation and data acquisition is shown in Figure 3.1. A highly conducting silicon wafer with a 1 μm thick thermally grown oxide layer was utilized as the substrate. The substrate was spin-coated with a 1% Teflon solution (DuPont) to impart hydrophobicity. An aluminum wire of 125 μm diameter is inserted into the droplet from the top as shown in Figure 3.1. A voltage difference applied between the silicon wafer and this wire actuates the droplet. De-ionized (DI) water droplets of volume 5 ± 0.1 μl are used in all the experiments. The initial contact angle and the contact radius of the droplet under no electrical actuation are 119° ± 2° and 0.97 ± 0.03 mm, respectively. The gravitational effects on the droplet shape are negligible as the Bond number (*Bo*, the ratio of the gravitational and surface tension forces) is approximately 0.17 and hence the droplet can be assumed to be a spherical cap.

The DC voltage for droplet actuation was provided using a high voltage DC power supply (Kepco BHK 2000- 0.1MG), while the AC voltage was supplied by a variable-frequency signal generator (Tektronix AFG 3022) and a voltage amplifier (Piezo Amplifier EPA-104, Piezo Systems Inc.). The droplet response to the applied actuation was recorded at 1000-2000 fps using a high speed camera (Photron 1024 PCI). All the images were processed using an in-house MATLAB [119] program to determine the dynamic contact angle and interfacial contact radius. The code includes an algorithm to determine the edge of the droplet. The intersection of the droplet image with the corresponding reflected image is used to define the point of contact. A second-order polynomial fit to the detected edge near the contact point gives the best estimate of the

droplet profile near the contact. The derivative of the tangent to the curve at the contact point is subsequently used to determine the contact angle. The reported contact angle is the average of the right and the left contact angles. The pixel resolution is 10 microns per pixel. The experimental uncertainties in the measured contact angle and contact radius arising from the imaging and image processing are approximately ± 2° and ± 0.03 mm, respectively. Each experiment was repeated three times, and the variation in measurements was found to be within experimental uncertainty; results from representative cases are presented in the following section. Liquid loss due to evaporation is negligible since the time period of each experiment is on the order of milliseconds.

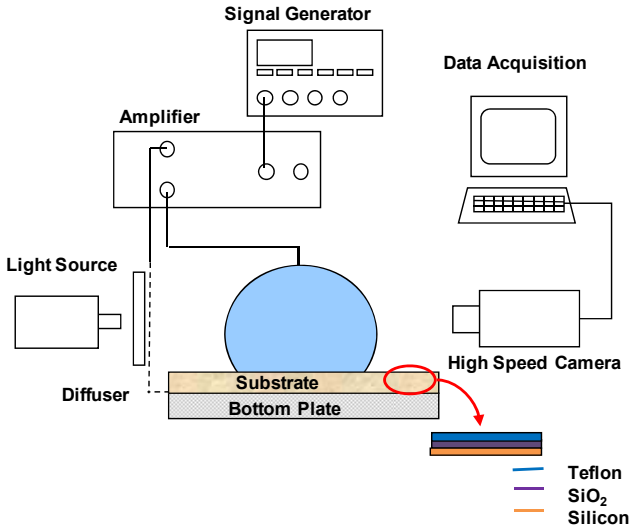

Figure 3.1. Schematic diagram of the experimental setup.

3.2 Results and Discussion

3.2.1 DC Actuation

The transient step response of a sessile droplet under DC voltage actuation is studied in the first set of experiments. DC voltages in the range of 40 V to 120 V (in increments

of 10 V) are applied to the droplet. The measured steady-state contact angle θ at each voltage is lower than Young's contact angle θ_Y as predicted by Lippmann's equation,

$$\cos\theta = \cos\theta_Y + \frac{1}{2\gamma} c V^2 . \tag{3.1}$$

where V is the applied actuation voltage, γ is the surface tension of the liquid (0.072 N/m for water), and $c = \frac{\varepsilon_0 \varepsilon_r}{d}$ is the capacitance of the dielectric layer, with ε_0 being the vacuum permittivity, ε_r the permittivity constant of the dielectric layer (3.9 for the oxide layer), and d the dielectric thickness (1 μm in the present work). Equation (3.1) can be written as $\cos\theta = \cos\theta_Y + \left(\frac{V}{V_L}\right)^2$, in which V_L refers to the voltage up to which the Lippmann equation can be used to predict the steady-state droplet contact angle during electrowetting. V_L is defined as $\sqrt{\frac{2\gamma}{c}}$ and is the characteristic voltage scale [48], equal to 65 V for the given experimental conditions. Equation (3.1) does not apply to the transient variation of droplet contact angle (prior to its attaining a steady shape).

A quantitative comparison of the different dissipation forces involved in electrowetting by Ren *et al*. [120] determined that the contact line friction contributes the dominant dissipative effect. The transient response of the droplet can be modeled in terms of the major horizontal forces acting on the contact line, i.e., surface tension forces, electrowetting force and contact line friction. A simplified mathematical model to understand the transient radial motion of the droplet contact line was developed by Annapragada *et al*. [121]. The droplet transport equation is obtained by equating the rate of change of momentum per unit length to the sum of all the forces acting at the contact line per unit length.

Figure 3.2a and Figure 3.2b show the transient step response of droplet contact angle and contact radius (normalized with respect to the initial contact radius), respectively. The normalized contact radii are used to provide the relative magnitude of droplet spreading with respect to the initial contact radius. At each of the actuation voltages, the contact angle decreases to a steady-state value that depends on the applied DC voltage; the contact radius correspondingly increases during the transient period. The steady-state contact angle decreases as the applied voltage is increased to 80 V, beyond which it saturates. The average steady-state contact angles corresponding to 80 V, 100 V and 120 V are 72.4 ± 0.6°, 73.2 ± 0.3°, and 71.2 ± 1.2°, respectively. Thus the average saturated contact angle of the droplet is 72.2° ± 1.2°. The contact radius has a similar trend, with the steady-state droplet radius reaching approximately 1.54 ± 0.03 mm at voltages higher than or equal to 80 V. The time taken for the droplet to attain a steady shape is approximately 35 ms and varies somewhat depending upon the magnitude of actuation voltage.

An interesting phenomenon of droplet oscillation is observed at high DC voltages. Figure 3.2b shows that the contact radius increases monotonically to 1.1 mm and 1.4 mm, respectively, at the lower actuation voltages of 40 and 60 V; however, at actuation voltages of 80 V and higher, the contact radius overshoots its equilibrium wetted radius due to higher inertia and induces oscillation in the contact radius and contact angle. Droplet shapes at the actuation voltage of 100 V at different time instances are included in Figure 3.2b to illustrate this oscillation. For this case, the droplet displays a maximum contact radius of 1.58 mm at t = 9 ms and then recoils to a smaller radius of 1.44 mm at t = 13 ms. The contact line oscillation continues until the droplet attains its equilibrium

contact radius of 1.5 mm at t = 25 ms. Similar observations have been made by Oh *et al*. [39] and Sen *et al*. [40]. Independent of the applied voltage, the droplet takes 8 to 9 ms to attain a maximum contact radius, which we define as the characteristic time scale (τ).

The dependence of the characteristic time scale (τ) on the governing parameters – liquid surface tension (γ), liquid density (ρ), droplet radius (R), coefficient of contact line friction (ξ), contact line velocity (v_{CL}), and applied electrical force (Fe) – is determined using the Buckingham Pi theorem with γ, R, ρ as the recurring variables. The resulting nondimensional terms are $\left(\frac{\gamma}{\rho R^3}\right)^{1/2}\tau$, $\left(\frac{1}{\gamma\rho R}\right)^{1/2}\xi$, $\left(\frac{\rho R}{\gamma}\right)^{1/2}v_{CL}$, $\left(\frac{1}{\gamma R}\right)F_e$. After minor rearrangements, the time scale can be represented as a product of $\left(\frac{\rho R^3}{\gamma}\right)^{1/2}$ and a function of the ratios of electrical force and contact line friction with respect to surface tension as: $\tau = \left(\frac{\rho R^3}{\gamma}\right)^{1/2} f\left(\frac{F_e}{\gamma R}, \frac{\xi v_{CL}}{\gamma}\right)$, where F_e/R is the electrical force per unit length and ξv_{CL} is the contact line friction per unit length. The contact line velocity (v_{CL}) increases with increasing actuation voltage (Figure 3.2). Since the actuation force and the friction force act against each other, it can be assumed that the effect of increased voltage is nullified due the increased friction resulting in $f\left(\frac{F_e}{\gamma R}, \frac{\xi v_{CL}}{\gamma}\right)$ to be more or less a constant. This explains the observed voltage independence of the time scale. A constant prefactor multiplied with $\left(\frac{\rho R^3}{\gamma}\right)^{1/2}$ describes the experimentally observed time scale for maximum

wetted diameter reasonably well. The characteristic time (τ) of the droplet under the present experimental conditions is ~ 9 ms, from which the constant of proportionality is deduced to be ~ 2.4. Thus the characteristic time constant can be written as $2.4\left(\frac{\rho R^3}{\gamma}\right)^{1/2}$. It is interesting to note here the similarity in the expression of this characteristic time scale and the contact time of the droplet impinged on a surface. Richard *et al*. [122] used a scaling analysis between kinetic energy per unit volume of droplet and pressure gradient to study the contact time when a droplet is impinged on a surface and determined the time scale to be independent of its velocity. The time scale was determined to be proportional to $\left(\frac{\rho R^3}{\gamma}\right)^{1/2}$ as well and was independent of the velocity of impingement.

At voltages lower than 60 V (a value that agrees well with the predicted characteristic voltage of 65 V), the electrical actuation force quasi-statically balances the net contact line friction and surface tension, whereas at higher voltages (> 60 V), the higher inertia causes the contact line to overshoot its equilibrium position and undergo damped oscillation under the action of contact line friction. While the contact radius is essentially pinned after one cycle of oscillation, the contact angle continues to oscillate for a longer period as seen in Figure 3.2a. This can be explained in terms of the two different damping mechanisms namely the contact line friction and viscous dissipation. The contact radius oscillation is damped significantly by the contact line friction, accompanied by a dampening of the contact angle oscillation. The internal flow generated within the droplet due to motion of the contact line and capillary waves on the

surface of the droplet takes a much longer time to reach a steady state due to the low viscous dissipation in water resulting in under-damped oscillations of the contact angle and height of the droplet even when the contact radius is pinned. The viscous dissipation is extremely low in comparison to the contact line friction and the ratio is given as $\frac{\xi}{\mu_{water}} = \frac{0.4\,N.s.m^{-2}}{0.001N.s.m^{-2}} = 400$, where ξ is the coefficient of friction; $\xi = 0.4$ Ns/m^2 is based on the experimental data for the water/Teflon combination from Wang and Jones [123]. This value was also used by Annapragada *et al.* [121] for numerical modeling of droplet dynamics during DC actuation and gave excellent agreement with the present experimental results. The effect of both contact line friction and viscous dissipation in overall dampening as well as suppression of contact angle oscillation due to hysteresis effects explains the time scale for contact angle oscillation not being 400 times greater than the time scale over which the contact radius oscillates before attaining a constant value. The time required to attain the steady-state droplet profile depends on the extent of contact line oscillation which varies with the applied voltage; for example the contact angle oscillation continues for a longer period when actuation voltage is greater than 60 V.

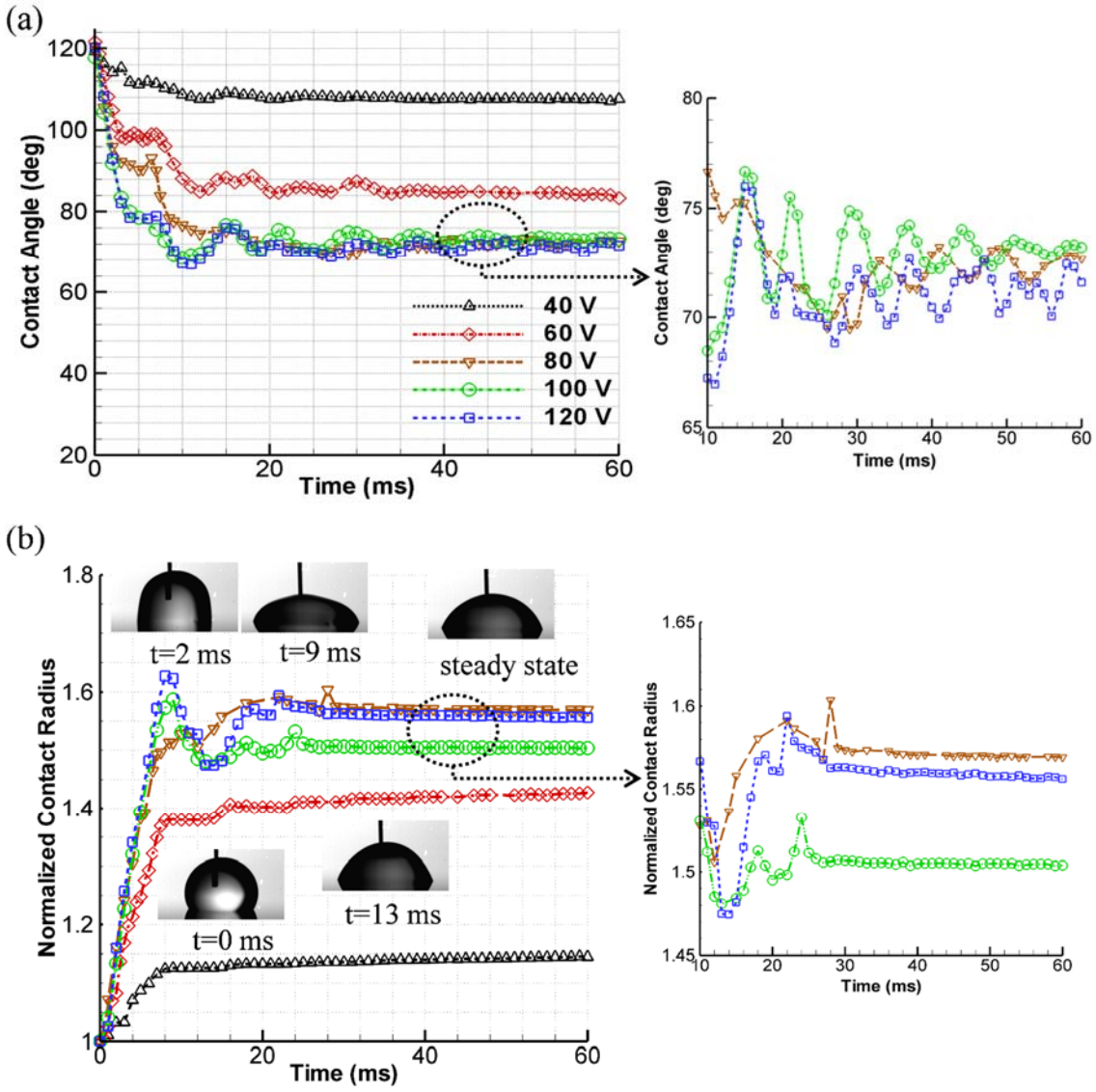

Figure 3.2. Transient (a) contact angle, and (b) contact radius of the droplet illustrating the step response. The insets on the right show the zoomed-in data points for actuation voltages of 80 V and greater, at which contact angle saturation occurs.

3.2.2 AC Actuation

3.2.2.1 Contact Angle and Contact Radius

Droplet oscillation at sinusoidal AC actuation voltages of 40, 60, and 80 V_{rms} is now explored to determine the combined effects of frequency and applied voltage. The range

of frequency of the electrical signal used for the experiments is such that the droplet is able to respond to the electrical force acting at the triple contact line (TCL). The frequency is varied from 5 Hz to 200 Hz in steps of 5 Hz. Results are presented here at representative frequencies of 5, 20, 60, 80, and 120 Hz which reveal the characteristic droplet behavior in the frequency range.

Figure 3.3a and Figure 3.3b show the time variation of contact angle and normalized contact radius, respectively, for the three actuation voltages at a frequency of 5 Hz. Results are shown after the first half cycle of droplet oscillation to omit uncertainties involved during the initiation of droplet motion. The symbols show the experimental data and the dashed lines show Fourier-series based curve-fits to the data. At the low frequency (5 Hz), the droplet follows the sinusoidal signal well as the characteristic time scale (9 ms) is much smaller than the time period of the applied electrical force (100 ms). As the electrical forces are proportional to the square of the applied voltage, one cycle of applied signal produces two cycles of droplet oscillation. For the case of 40 V_{rms} the contact angle variation has a sinusoidal shape with a minimum contact angle of 84^0 (Figure 3.3a). This lower contact angle compared to the measured value of 107^0 for 40 V DC actuation (as seen in Figure 3.3a) is due to the higher peak voltage of 56 V in the AC signal. As the actuation voltage is increased to 60 V_{rms}, the contact angle is seen to saturate at approximately 70^0 when the instantaneous voltage exceeds 80 V (between 240 ms and 260 ms in Figure 3.3b). The contact angle saturation occurs at a higher actuation voltage compared to the case of DC actuation (70 V). The saturation effect is more prominent at the higher voltage of 80 V_{rms} (Figure 3.3b) between the instantaneous values of 80 V and 113 V (corresponding to the time interval from 225 ms to 275 ms). During

this period, the CR and CA remain relatively unchanged with time. The main difference in the characteristics of the contact line of the droplet at the 60 V_{rms} and 80 V_{rms} actuation voltages is the velocity at which the droplet reaches its maximum contact radius as derived from the slope of the graph as the droplet reaches the maximum wetted radius (Figure 3.3**.**b). The measured droplet contact radii for the three cases follow similar trends as the contact angles, as shown in Figure 3.3b. The contact radius is in phase with the contact angle, i.e., the contact radius increases with a decrease in contact angle. The insets in Figure 3.3b show the droplet shapes at 150 ms for all three actuation voltages; this time instant corresponds to the maximum spreading.

The non-dimensional contact radius is slightly greater than 1 at the instant of zero actuation due to the effect of contact angle hysteresis. The higher inertia at 60 V_{rms} and 80 V_{rms} as compared to 40 V_{rms} results in a non-dimensional CR equal to 1.01 ± 0.02 as compared to 1.05 ± 0.02 in the latter case (Figure 3.3b).

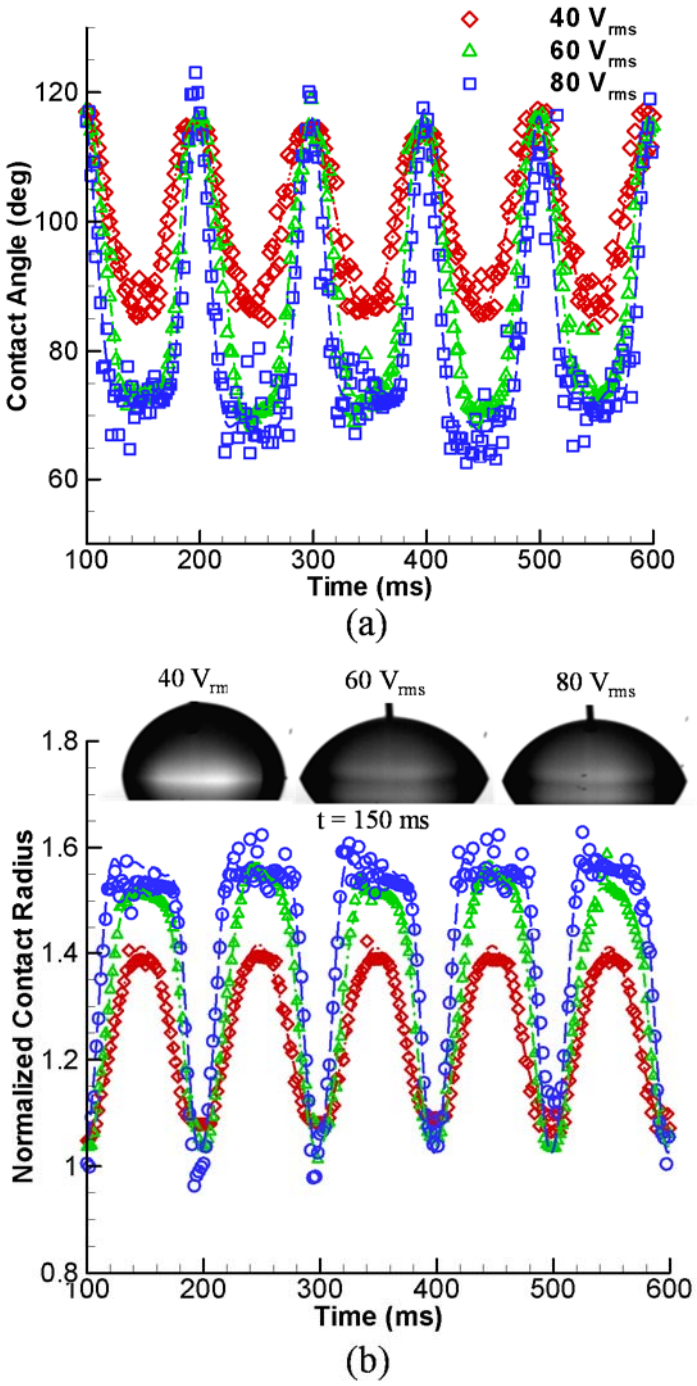

Figure 3.3. Transient variation of (a) contact angle, and (b) contact radius for an AC frequency of 5 Hz and V_{rms} = 40 V, 60 V, and 80 V; insets in (b) show the corresponding droplet shapes at 150 ms.

To understand the effect of actuation frequency on droplet oscillation, the transient contact angles and contact radii for droplet actuation at frequencies of 20, 60, 80, and 120 Hz with AC actuation voltages of 40 V_{rms} and 60 V_{rms} are shown in Figure 3.4a and Figure 3.4b, respectively. As before, the plot is shown after the first cycle of the droplet oscillation to omit uncertainties during droplet motion initiation; the symbols show the data as obtained from the experiments, while the dashed lines are Fourier-series fits. While the droplet oscillations are periodic in nature because of the sinusoidal voltage applied, a number of interesting effects of the actuation frequency are observed. At a constant voltage, the amplitude of oscillation decreases with increasing frequency since the decreased time period of oscillation increases the influence of the characteristic response time. From the step response of the droplet, it is seen that the droplet takes ~ 9 ms to reach its maximum wetted position (Figure 3.2b). It can be interpreted that the droplet can respond fully to the applied force till a forcing frequency of 111 Hz (with a corresponding signal frequency of 55 Hz). This explains the higher wetted diameters reached at lower actuation frequencies (5 Hz and 20 Hz) as compared to those at frequencies higher than 60 Hz. For example at 120 Hz, the time before the droplet can attain its maximum electrowetted radius is 2.1 ms and is lower than the characteristic time scale. Moreover, oscillation of the droplet is manifested not only as movement of the contact line but also as shape oscillations [125]. Hence the quasi-static response of the contact line to the electrical force as the voltage increases from 0 V to the maximum value in each signal cycle may no longer be assumed. The spherical cap assumption is no longer valid during the droplet oscillation. The plot of the variation of the contact radius with time (Figure 3.4) suggests an overlap of multiple frequency responses.

At 60 Hz, the contact angle and contact radius are out of phase by a finite angle of 0.75 radians. On the other hand, droplet oscillations at close to resonant frequencies significantly influence the droplet response as will be discussed in the next section. For example, the amplitude of the contact radius oscillation at 120 Hz is seen to be higher than that at 60 Hz (normalized values of 0.08 and 0.06, respectively, for 40 V_{rms}). Moreover, the droplet contact radii and contact angles are in-phase at 80 Hz and out-of-phase by approximately 0.94 radians at 120 Hz, for both 40 V_{rms} and 60 V_{rms}. The contact radius always follows the applied signal; a small time delay is observed at the highest actuation voltage, consistent with the characteristic time constant for complete response. The analysis to follow presents the phase lag between the contact angle and contact radius. It is also noted that the phase lag does not depend on the applied actuation voltage, but only on the actuation frequency; however there is some difference in the behavior of the contact radius at 40 V_{rms} and 60 V_{rms} corresponding to 60 Hz and 80 Hz actuation frequency in terms of the magnitude, but the phase difference remains unchanged. More details regarding the droplet shape dependence on frequency are discussed in the next section.

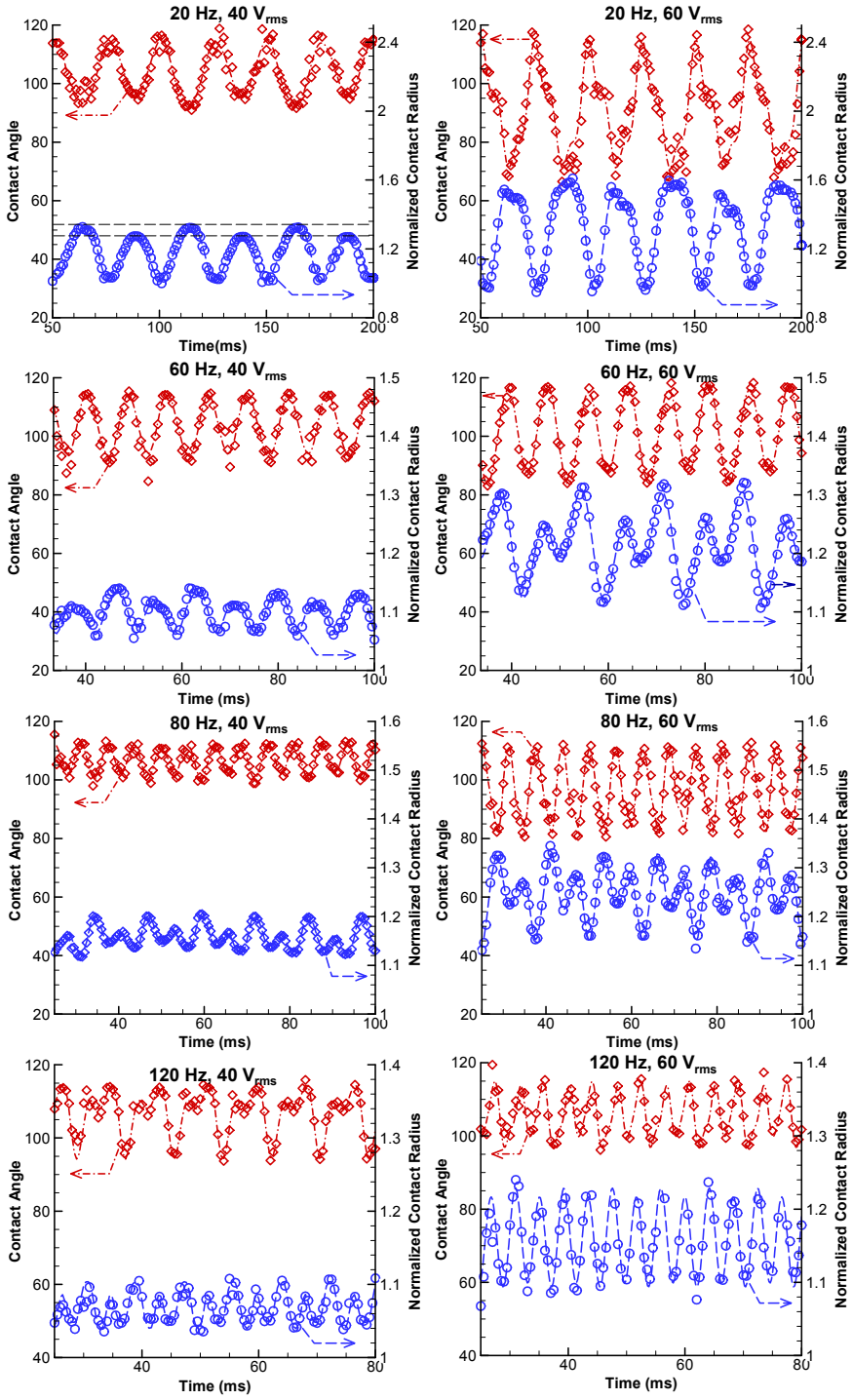

Figure 3.4. Variation of contact angles and contact radii for actuation frequencies of 20, 60, 80 and 120 Hz at (a) 40 V_{rms}, and (b) 60 V_{rms}.

3.2.2.2 Sub-harmonic Oscillation

An interesting feature seen in the droplet oscillation (Figure 3.4) is the sub-harmonic behavior of the droplet contact radius; i.e., the maximum contact radii in successive droplet spreading cycles oscillate between two values. For example, at 40 V_{rms} and 20 Hz, the two values of the maximum contact radii are 1.3 and 1.24 as highlighted in Figure 3.4. The relative difference between these pairs of maximum contact radii increases as the actuation is AC frequency increased at the same actuation voltage. It is also observed that this behavior is not as pronounced in the contact radius variation at 40 V_{rms} and low frequencies of 20 Hz; however, at 40 V_{rms} with 80 Hz and 120 Hz, the contact radii do clearly exhibit such sub-harmonic behavior. Such behavior was also noted by Sen *et al*. [40] for one frequency, but was not explored in detail. Ko et. al. [124] observed the primary response of the droplet at the actuation frequency, i.e., at half the frequency of the applied electrical force during electrowetting driven oscillations of bubble. However such a droplet response has not been fully explained.

A Fast Fourier transform is performed on the raw data for contact angle and contact radius corresponding to the cases in Figure 3.4. The results are plotted in Figure 3.5 in order to capture the frequency response of the droplet oscillation under electrical actuation. The quality of the FFT plots is influenced by the finite number of data points used in the analysis. An integer number of oscillations are considered during the analysis, and random chopping off of the response data is avoided. All contact angles and radii have a maximum response at the frequency corresponding to that of the electrical force acting on the droplet, which is twice the applied actuation frequency (i.e, $2f_v$ where f_v is the actuation frequency). However, a significant response is also seen at the frequency (f_v)

of the imposed signal in most cases. A super-harmonic response (less dominant than the sub-harmonic component) is observed in cases with high actuation voltage; the droplet response corresponding to 5 Hz and 60 V_{rms} demonstrates a stronger super-harmonic than 40 V_{rms}. At higher frequencies, the super-harmonic oscillation is suppressed. The ratios of the harmonic and the sub-harmonic responses for all cases are listed in Table 3.1 which clearly shows that the sub-harmonic response at the actuation frequency f_v increases with frequency and actuation voltage and is stronger in the contact radii traces as compared to the contact angle traces. Table 3.1also includes the ratio of frequency responses corresponding to actuation at 5 Hz, 80 V_{rms} and 80 Hz, 80 V_{rms} which are not shown in Figure 3.4 and Figure 3.5 to avoid cluttering of the data points.

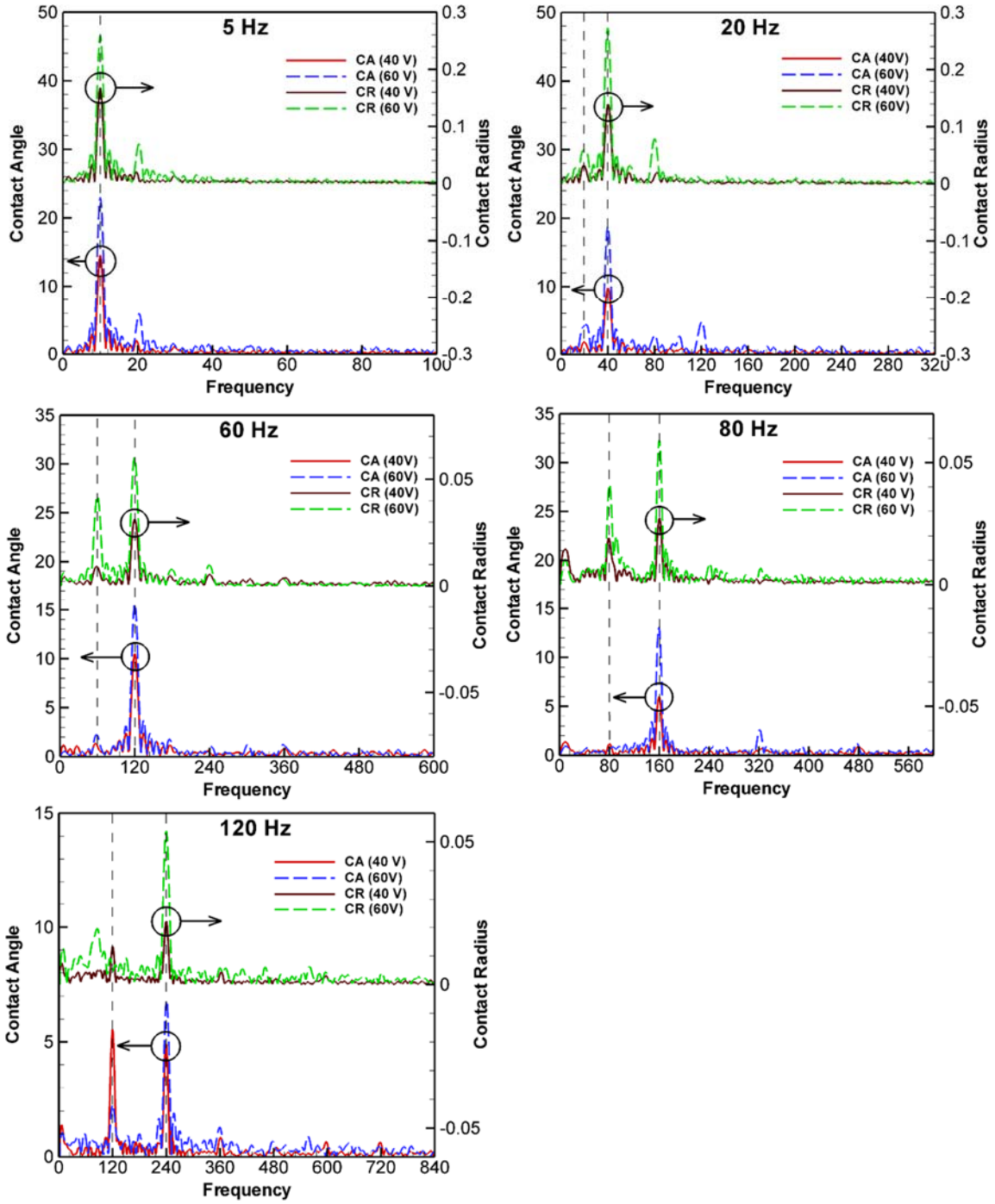

Figure 3.5. Fast fourier transforms for droplet response corresponding to actuation frequencies of 5, 20, 60, 80, 120 Hz at applied voltages of 40 V_{rms} and 60 V_{rms}.

Table 3.1. Droplet response at forcing and sub-harmonic frequencies.

Frequency (Hz)	**Applied Voltage (V_{rms})**	**Ratio of frequency response of CR at sub-harmonic (f_v) and harmonic frequencies ($2f_v$)**	**Ratio of frequency response of CA at sub-harmonic (f_v) and harmonic frequencies ($2f_v$)**
5	40	0.06	0.04
	60	0.05	0.04
	80	0.10	0.10
20	40	0.23	0.19
	60	0.22	0.22
60	40	0.29	0.11
	60	0.70	0.14
80	40	0.69	0.20
	60	0.69	0.05
	80	1.90	0.06
120	40	0.60	1.13

In order to investigate the reason for the sub-harmonic oscillation observed, experiments are carried out under the application of both positive as well as negative potential at the substrate to determine the dependence of the polarity of the substrate on the electrowetted contact angle. The dependence of contact angle on the polarity at the substrate during electrowetting is determined by the material of the dielectric, which in our experiments is silicon dioxide. The contact angle variations with respect to applied voltage for both the polarities almost overlap (Figure 3.6). The average contact angle once saturation is reached is 72.9° ± 1.5° with positive potential at the substrate, and 73.9° ± 1.2° with negative potential at the substrate, which are essentially identical. This

polarity independence of contact angle with the substrate used in the experiments is in agreement with the work of Cho *et al*. [26] who also observed the polarity-independence of a silicon dioxide substrate coated with Teflon. Hence it is unlikely that the electrical force has a secondary component.

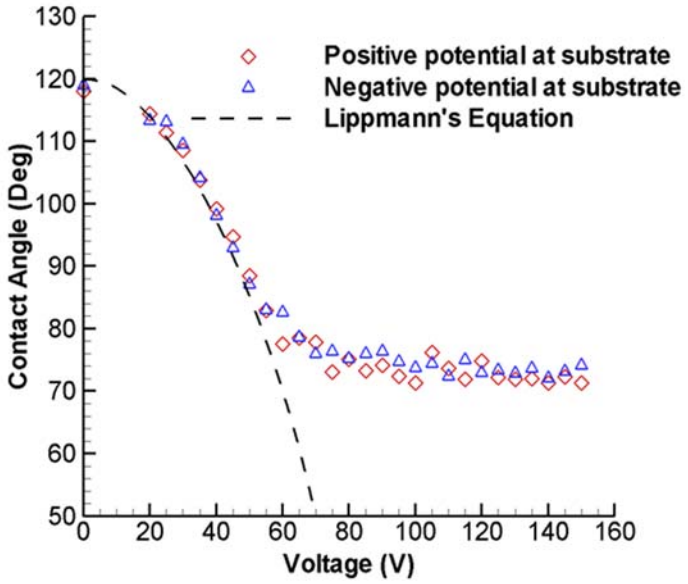

Figure 3.6. Contact angle of the droplet with the substrate maintained at positive and negative potentials.

When the electrical force acts at the TCL, it drives droplet oscillation and may excite several modes [125] depending upon the frequency of actuation. We present here an approach similar to that by Baret *et al*. [126] to determine the governing equation for droplet oscillation at the TCL and give a possible explanation for the sub-harmonic response of the droplet. The terms accounting for the modes (n) are neglected so as to give a simple expression for the transport equation. The Navier-Stokes equation representing balance of forces acting on the droplet can be written as

$$\frac{\partial u}{\partial t} + u \cdot \nabla u = \frac{1}{\rho}\left(\mu \nabla^2 u - \nabla p + f_e - \frac{F_f}{\forall} \right) \tag{3.2}$$

where $\forall$ is the droplet volume, f_e the electrical body force density and F_f the contact line friction. For water, the viscous dissipation can be neglected in comparison to the other forces acting during electrowetting [126]. For small oscillation, i.e., when the displacement of the contact line (x) is very small compared to the initial droplet radius ($x << R_c$), the non-linear convection term can be neglected [126]. The pressure gradient across the drop (∇p) can be approximated as $\nabla p = -\frac{\gamma}{R_c^2}\left(1 - \frac{2x}{R_c}\right)$. With an assumption that significant voltage drop occurs across the dielectric layer, the negative derivative of the stored energy (E) gives the electric force (F_e) acting on the droplet as

$$E = \frac{\varepsilon_0 \varepsilon_r A(r) V^2}{2d} \tag{3.3}$$

$$F_e = -\frac{dE}{dr} = -k' r (1 - \cos(2\omega t)) . \tag{3.4}$$

where r is the contact radius $(r = R_c + x)$, $A(r)$ is the instantaneous interfacial area, $V = U \sin(\omega t)$ is the applied voltage; U is the amplitude of applied voltage, and $k' = \frac{\varepsilon_0 \varepsilon_r \pi}{2d} U^2$; the contact line friction is proportional to the velocity of the contact line [120, 123] ($F_f = \xi \dot{x}(2\pi r)$), where ξ is the contact line friction coefficient.

Assuming that a constant mass, m is involved in the oscillation of the droplet, the final simplified expression for the droplet oscillation at the contact line, i.e., at $\theta = \pi/2$ takes the form,

$$\ddot{x}+\left(\frac{2\pi\xi}{m}(x+R_c)\right)\dot{x}+\left(\frac{2\gamma}{\rho R_c{}^3}-\frac{k'}{m}(1-\cos(2\omega t)\right)x=\frac{k'}{m}\left(1-\cos(2\omega t)\right)R_c+\frac{\gamma}{\rho R_c{}^2}. \qquad (3.5)$$

As is obvious from Eq. (3.5), the force acting on the TCL is parametric, i.e., it is a time-dependent force which also depends upon the magnitude of displacement (x).

This governing equation (Eq. (3.5)) is in the form of a parametrically excited and nonlinearly damped nonlinear equation [127]. The damping force, which is contact line friction in this case, as well as the forcing term are dependent on the instantaneous displacement of the contact line with respect to the initial contact radius. Depending upon the forcing amplitude (a function of the applied voltage), the governing equation is expected to have a sub-harmonic frequency as a solution together with the response at the forcing frequency (which is twice the frequency of the periodic input applied) in a particular range of frequency. The most convincing explanation for the sub-harmonic response of the droplet with periodic actuation at certain frequencies (> 20 Hz) is the Faraday instability [128], which is a characteristic outcome of the parametric excitation at the contact line. In the modified Pellat's experiment by Wang and Jones [123], a vigorous side-to-side sloshing motion of the liquid surface was observed when an electrical signal with frequency < 200 Hz was used to actuate the liquid (DI water) column. This phenomenon might be attributed to the parametric nature of the electrical force. Sub-harmonic oscillations have been studied in liquid droplets when a vertical oscillation is provided [129] and also in the case of magnetic actuation [77]. The important implication of this finding is that this phenomenon must be considered in droplet dynamics models for unsteady electrowetting-driven actuation

3.2.2.3 Droplet Oscillation Regimes

The droplet contact line motion is significantly influenced by the frequency of actuation and the modes of oscillation as discussed in the previous section. In this section we determine the resonant frequencies of the droplet using Lamb's expression [130] and compare the values against the experimentally observed resonant frequencies, and determine the length scale appropriate for the determination of the same. The frequency regimes for in-phase and out-of-phase behavior of the droplet contact radius and contact angle are reported.

The bulk of the liquid can be treated as inviscid due to the low kinematic viscosity of 10^{-6} m^2/s of water. The natural oscillation of an inviscid liquid droplet in a gaseous medium has been well studied in the literature and the resonant frequency for the n^{th} mode oscillation is given by Lamb's expression [130] given by

$$f = \frac{1}{2\pi}\left[n(n-1)(n+2)\frac{\gamma}{\rho l^3} \right]^{1/2}. \tag{3.6}$$

where ρ is the liquid density and l the characteristic droplet length. The characteristic droplet length for a droplet resting on a solid surface is not well-defined and hence, three lengths are considered: the droplet contact radius (R_c), the initial droplet radius before actuation (R_o), and the initial droplet height (h). For a droplet of volume 5 μl, using droplet contact angle as 120°, R_c = 0.9722 mm, R_o = 1.123 mm and h = 1.68 mm. All the length scales used are calculated using the spherical cap assumption of the droplet. Resonance occurs when the frequency of the electrical force (which is twice the frequency of the applied signal) matches the natural frequency of the droplet. The

resonant frequencies for a 5 μL water droplet corresponding to these characteristic lengths are given in Table 3.2.

Table 3.2. Natural frequencies for the n^{th} oscillation mode using Lamb's expression.

Mode, n	$l = R_c$		$l = R_o$		$l = h$	
	Resonant frequency of the droplet (Hz)	**Corresponding freq. of the applied voltage (Hz)**	**Resonant freq. of the droplet (Hz)**	**Corresponding freq. of the applied voltage (Hz)**	**Resonant freq. of the droplet (Hz)**	**Corresponding freq. of the applied voltage (Hz)**
2	126.0	63.0	101.6	50.8	55.3	*27.6*
3	244.0	122	196.7	98.3	107.0	53.5
4	378.0	189.0	304.7	152.3	165.8	*82.9*
5	527.1	263.6	424.8	212.4	231.2	115.6
6	690.2	345.1	556.2	278.1	302.8	*151.4*

Droplet oscillation at 60 V_{rms} and frequencies from 5 Hz to 200 Hz in steps of 5 Hz is documented in Figure 3.7 to show the distinct frequency regimes and the effect of resonance on droplet oscillation dynamics within each regime. The figure shows four quantities as function of the frequency of the applied signal: the maximum displacement in the contact radius (defined as difference between the maximum and minimum contact radii for a given applied frequency; the CR prior to actuation is not used as the reference since a lower minimum contact radius is observed at frequencies close to resonance); the maximum contact radius attained; the instantaneous contact angle observed at the time instant when the maximum displacement in the contact radius is attained; and the minimum contact angle corresponding to each frequency. The displacement of the

contact radius was used to experimentally determine the resonance frequencies. Intuitively, the instant of maximum contact radius of the droplet should correspond to the minimum contact angle (and *vice versa*). This in-phase behavior of the CR and CA is observed, for example, when the frequency is between 5 and 30 Hz. At these low frequencies (5 - 20 Hz), the droplet oscillates quasi-statically in response to the sinusoidal signal; a spherical cap assumption can be made for the droplet shape during oscillation. During the initiation of droplet motion, video recordings reveal that the bulk of the liquid droplet moves downwards, thereby increasing contact radius. The droplet oscillation increases drastically at 40 Hz. Interestingly, the oscillation is more prominent in the height of the droplet rather than the radius of the droplet although the main electrical force is concentrated at the TCL.

The non-overlapping plots of instantaneous CA corresponding to maximum CR and the minimum CA at certain frequencies indicate the phase lag between the contact line motion and the contact angle. For actuation frequencies between 40 Hz and 70 Hz, the contact radius and contact angle become out-of-phase with the droplet oscillating in its 2^{nd} mode (as shown in the droplet shape at 40 Hz in the inset in Figure 3.7). The arrows around the droplet photograph show the nodal points. This is in agreement with the results of Lai *et al.* [131] who also observed out-of-phase behavior between the applied voltage and the droplet motion at the droplet resonant frequencies. The droplet reverts to its in-phase behavior at a frequency of approximately 70 Hz. However, the contact line oscillation is much reduced at these frequencies. The magnitude of oscillation is at its minimum until the frequency of the AC signal is increased to a value of approximately 100 Hz, at which the contact line movement increases significantly and the droplet

continues to oscillate with the contact angle being in-phase with the contact radius. Beyond 100 Hz, a prominent 4^{th} mode of oscillation is observed in the droplet (Figure 3.7). The droplet oscillation exhibits out-of-phase behavior beyond a frequency of 115 Hz until the 6^{th} mode of oscillation becomes dominant at frequencies higher than 180 Hz. Figure 3.7 shows the droplet oscillating in the 6^{th} mode of oscillation at a frequency of 190 Hz. The closest agreement between the experimentally obtained resonance frequencies and those predicted using Eq. (3.6) is found when droplet height is selected as the characteristic length; this is consistent with the experimental observations of Kim [132].

An interesting correlation is seen between the contact angle and contact radius as a function of the frequency of AC actuation. After the droplet attains a resonance frequency, the CR and CA go out of phase; this continues till the next higher level of resonance frequency is dominant. The change in phase is accompanied by minimal contact line movement; the contact line is almost pinned during this time and the oscillation takes the form of varying contact angle. Whether the droplet oscillates in-phase or out-of-phase is a characteristic of the droplet that is directly related to the resonance phenomenon. The magnitude of oscillation and the phase angle between the CR and CA is also a result of the interaction between the different modes of oscillation of the droplet. Accordingly, droplets of different volumes will show in-phase or out-of-phase behavior corresponding to different values of actuation frequencies. Further study of the interaction between different modes during oscillation of a constrained droplet would help in understanding the detailed dynamics in terms of analytical determination of the exact magnitude of oscillation and corresponding contact angle.

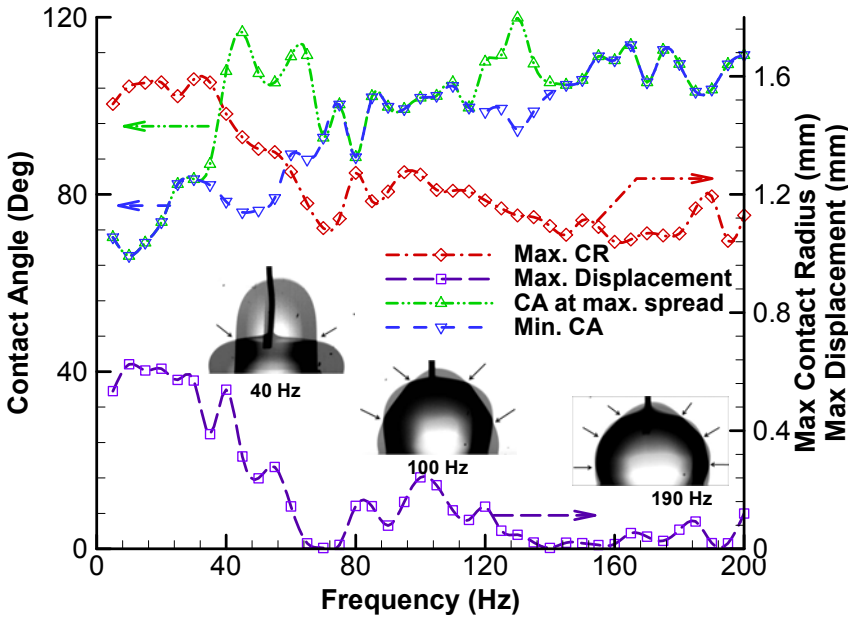

Figure 3.7. Droplet oscillation at 60 V_{rms} over a 5 Hz to 200 Hz frequency range. The images shown as insets demonstrate distinct modes of droplet oscillation corresponding to three different frequencies (40 Hz, 100 Hz and 190 Hz).

3.3 Summary

The transient response of a droplet to step actuation has been experimentally demonstrated. The local oscillations induced in the droplet result in a finite delay in the droplet achieving its steady-state profile. The droplet takes approximately 9 ms for a 5 μl droplet to reach the maximum contact radius irrespective of the voltage applied. It is demonstrated that the characteristic time scale is dependent upon the radius, density and surface tension of the droplet and should be taken into account in designing practical systems that exploit electrowetting actuation.

A detailed experimental study of the droplet dynamics reveals the dependence of the contact angle and contact radius on the applied frequency and voltage of a periodic sinusoidal signal. The droplet follows the signal at low AC frequencies and the

oscillations are mostly electrowetting-induced. At higher frequencies, distinct shape oscillation modes are induced which, along with resonance, determines the magnitude of oscillation and phase angle between contact angle and contact radius. The contact angle and contact radius show an alternating in-phase and out-of-phase behavior between successive resonant frequencies. The experimentally determined resonance frequencies are shown to be well estimated by Lamb's expression for natural frequency of a droplet when the height of the droplet is taken as the characteristic length scale in the prediction. Sub-harmonic oscillations of the droplet contact radius and contact angle during electrowetting are identified and are explained in terms of the parametrically excited nonlinear equation governing the droplet oscillation. These sub-harmonic oscillations are attributed to the nonlinear damping forces and the parametric excitation force acting on the droplet during electrowetting.

CHAPTER 4. ONE-STEP FABRICATION AND CHARACTERIZATION OF HIERARCHICAL SUPERHYDROPHOBIC SURFACES

This chapter describes a one-step fabrication methodology for hierarchical, two-tier roughness surfaces. This methodology eliminates the complexities of producing the second sub-micron roughness layer. Pillars of square cross-section are carefully engineered so that the single-roughness features inherently maintain the droplets in a stable Cassie state. The double-roughness surfaces are fabricated with the same primary roughness as the single-roughness pillars using a single-step Deep Reactive Ion Etch (DRIE) method. The hydrophobicity enhancement imparted by the second roughness layer is quantified by comparing the properties of the double-roughness (DR) surfaces to those of single-roughness (SR) surfaces. The static contact angle and the roll-off angle of millimeter-sized sessile droplets on such surfaces are experimentally determined and compared to the results from the corresponding single-roughness substrates. The behavior of the contact angle and the contact diameter during the evaporation of sessile droplets on both single- and double-roughness surfaces is investigated in the absence of surface heating. Droplet impingement experiments are then conducted on the double-roughness surfaces to test the robustness of their hydrophobicity and understand droplet dynamics on single tier and double tier roughness surfaces. The material presented in this chapter was published in *Journal of Micromechanics and Microengineering* (**21**, p. 105012, 2011) [71].

4.1 Sample Preparation and Experimental Setup

4.1.1 Sample Preparation

The fabrication procedure developed in the present work circumvents the conventional two-step process to create double-roughness structures. Silicon pillars constitute the larger roughness element. Photoresist residue forms on the pillars during the DRIE process; this residue is in the form of ~1 μm strands stacked on top of the silicon pillars and provides the second-tier roughness. The advantage of this method is that a double-roughness surface is obtained with a single deep reactive ion etching step. All fabrication for this work was carried out at the Birck Nanotechnology Center at Purdue University.

Silicon wafers with 1 μm thermally grown oxide layers were used as the substrates. A layer of positive photoresist AZ 1518 was spin-coated and lithographically patterned on the wafer. A wet-etch process is used to selectively etch the oxide layer from the surface. The oxide layer along with the photoresist acts as the etch mask for the deep reactive ion etch (Bosch) process. The Bosch process uses SF_6 for etching and C_4F_8 for the passivation steps. During etching the silicon is selectively etched to form the pillars. A higher passivation time and a lower O_2 gas flow during etching aids in retaining a fraction of the polymers formed during passivation. This results in the small roughness elements on the pillars which lead to the second-tier roughness. Table 4.1 lists the process parameters used for fabrication of the double-roughness surfaces. The etch rate for silicon was observed to be approximately 4 μm per minute. A minimum of 4 minutes of etch time was required for the formation of the second-tier roughness structures.

Table 4.1. DRIE process parameters.

Parameters	Value	
	etching	**passivation**
Switching time	5 sec	3 sec
Gas flow	450 sccm SF_6 15 sccm O_2	200 sccm C_4F_8
RF coil power	1500 W	1000 W

The surfaces are then spin-coated with 0.1% solution of Teflon-AF 1600 (DuPont, Wilmington, DE) in FC-77 (3M, St. Paul, MN) to impart hydrophobicity. The thickness of the Teflon layer is approximately 50 nm and hence the overall roughness of the primary roughness as well as the sub-micron roughness is not affected by the Teflon coating. The single-roughness surfaces SR-1, SR-2, and SR-3 used for comparison against the results from double-roughness surfaces are fabricated with the primary geometrical parameters held identical to those for the double-roughness surfaces DR-1, DR-2, and DR-3, respectively, using the negative photoresist SU-8 with standard lithography. The pillars are subsequently coated with Teflon to impart superhydrophobicity. The pillar geometry of the double-roughness surfaces fabricated is outlined in Table 4.2. The table also shows the two parameters utilized to quantify the primary surface roughness, namely, $\phi = \left(a^2 / p^2 \right)$ and $r_m = \left(1 + 4ah / p^2 \right)$, where a is the width of the square pillars, p is the pitch, b is the width of the air gap between the pillars such that $p = a + b$, and h is the height of the primary roughness elements. The dimensions of the pillars are chosen such that the Cassie state is energetically more

favorable [34]. Figure 4.1 shows SEM images of the double-roughness surfaces 1, 2, and 3.

Table 4.2. Parameters of the hierarchical surfaces.

Surface	**Pillar size, *a* (μm)**	**Pillar pitch, *p* (μm)**	**Pillar height, *h* (μm)**	***ϕ***	***b/a***	***r_m***	**Sub-micron roughness,R_a (μm)**
DR-1	27	42	32	0.41	0.56	2.96	0.33
DR-2	13	25	32	0.27	0.92	3.66	0.27
DR-3	33	47	32	0.49	0.42	2.9	0.33

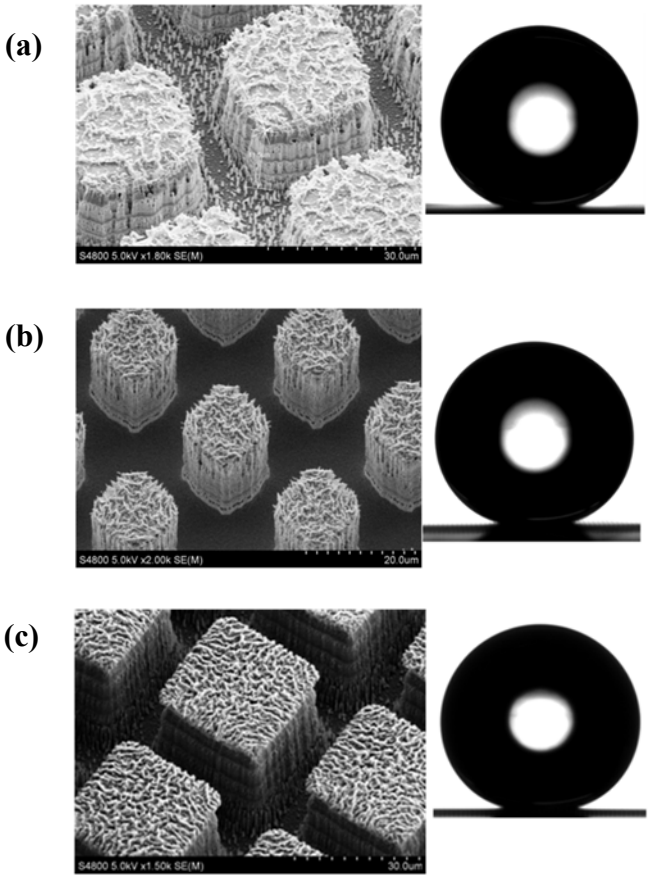

Figure 4.1. SEM images of hierarchical surfaces (a) DR-1, (b) DR-2, and c) DR-3. The images to the right show the static shape of a 3 μL water droplet placed on the corresponding surface.

4.1.2 Experimental Setup

Deionized (DI) water droplets of volume 3 μL ± 0.1 μL are used for all the characterization experiments (except the droplet impingement tests). The static contact angle of the droplets on the surfaces is measured using a goniometer (Model 290, Rame Hart), equipped with an automated tilt stage. For the droplet roll-off experiments, the stage is tilted slowly (0.8 deg/sec) to prevent inadvertent addition of momentum to the droplet. Images are simultaneously captured to analyze the advancing and the receding contact angles and the roll-off angle (α, the tilt angle at which droplet motion is initiated) of the droplet on the substrate (Figure 4.3). Three sets of tests are carried out on each substrate. The reported static contact angle is the average of the contact angles measured at five different locations on the substrate. The deviation in static contact angle is within $\pm 2^0$. The roll-off results are repeatable to within the standard deviation as described in a later section.

The droplet evaporation experiments help to characterize the behavior of the droplet contact line and the contact angle during evaporation on the hierarchical surfaces. Experiments are carried out without external heating under controlled temperature and humidity conditions of 21^0 C and 32%, respectively. A 3 μL droplet of water dispensed using a carefully calibrated microsyringe on to the test surfaces is visualized using the goniometer imaging system till it evaporates completely. A cold light source used for backlighting ensures improved contrast but does not affect the droplet evaporation rate. The contact diameter and the contact angle are measured during evaporation on the DR surfaces and compared to the evaporation characteristic of a droplet on the SR surfaces.

Finally, droplet impingement tests are carried out on the double- and the single-roughness surfaces to quantify the enhanced superhydrophobicity under impact imparted to the substrate by the secondary roughness layer. Droplet impingement was also tested with a smooth hydrophobic silicon substrate coated with Teflon to provide a baseline for comparison. A single droplet of volume 4.40 μL ± 0.25 μL is released from a height of 10 mm and 100 mm by means of a high-precision automated dispensing system fitted with a micro-syringe as shown in Figure 4.3. The impact dynamics of the droplet are visualized with a high-speed camera (1024 Photron PCI) at 3000 to 3750 frames per second. As in evaporation experiments, backlighting is used along with a diffuser for improved contrast. The images are subsequently analyzed using MATLAB [119] and Image J (an image processing program available from the National Institutes of Health). The advancing and the receding interface of the droplet, as well as the velocity at which the droplet leaves the substrate, are tracked.

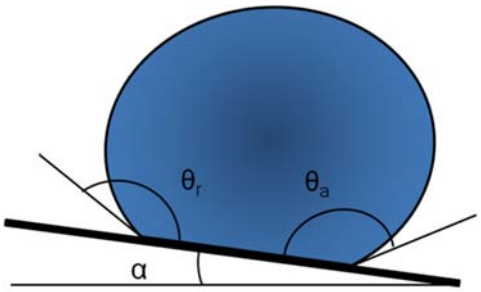

Figure 4.2. Schematic diagram of the sessile droplet and the angles measured.

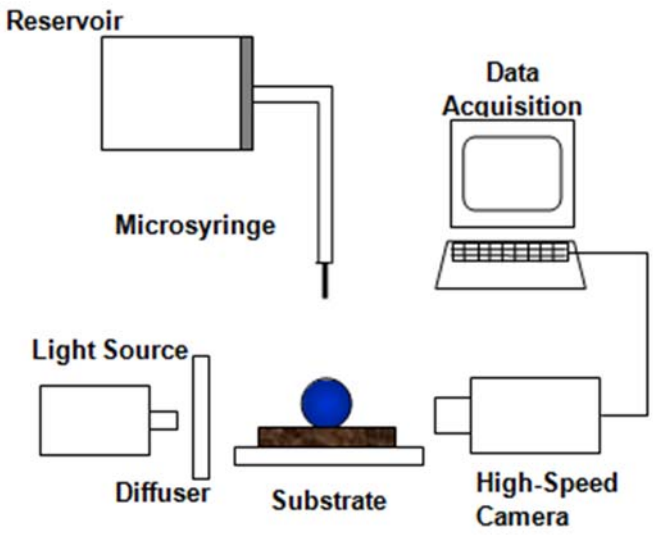

Figure 4.3. Experimental setup for droplet impingement test.

4.2 Results and Discussion

4.2.1 Static Contact angle and Roll-off Angle

When a droplet gently placed on a substrate is in its Cassie state (Figure 1.2a), the static contact angle θ_c can be approximated using the Cassie equation [4] as

$$\theta_c = \cos^{-1}\left(-1+\phi\left(1+\cos\theta_0\right)\right). \tag{4.1}$$

where θ_0 is the Young's contact angle on the smooth surface (measured to be 120^0 for water droplet on a smooth surface coated with Teflon). Table 4.3 lists the predicted and experimentally observed static contact angles of the droplet on the single-roughness surface and the observed static contact angles on the double-roughness surfaces. Good agreement is observed between the theoretical contact angles from the Cassie expression (Eq. (4.1)) and the experimentally observed contact angles. The observed value of contact angle on the double-roughness surfaces is greater than 160^0. This significant increase in the static contact angle of the droplet on the double-roughness surfaces

relative to the single-roughness surfaces (Table 4.3) is the first proof of their enhanced ultrahydrophobicity due to the presence of the sub-micron features.

Table 4.3. Static contact angle measured on the test surfaces.

	Static contact angle	
	predicted	**observed**
SR-1	142^0	$142^0 \pm 3.5^0$
SR-2	150^0	$147^0 \pm 3.0^0$
SR-3	139^0	$144^0 \pm 2.0^0$
DR-1	_	$161^0 \pm 2.5^0$
DR-2	_	$160^0 \pm 2.0^0$
DR-3	_	$161^0 \pm 1.5^0$

Before a droplet begins to move on an inclined surface, the droplet shape changes such that the forces acting at the triple contact line balance the gravitational force. The roll-off angle (α) decreases with an increase in droplet volume due to the increase in the gravitational force (*mg*) acting on the droplet [133]. Droplet roll-off experiments are carried out both on the double-roughness and single-roughness surfaces to determine the reduction in the contact angle hysteresis as well as enhancement in the roll-off characteristics due to the second layer of roughness. The capillary length of a water droplet defined as $\left(\gamma/\rho g\right)^{1/2}$ is equal to 2.7 mm. The characteristic length scale (diameter) of the 3 μL water droplet used in the experiments is approximately equal to 1.79 mm and is less than the capillary length. This implies that the effect of gravity can be considered negligible and the droplet assumed to be of spherical-cap shape [134]. Also, this results

in the surface forces being more dominant in comparison to the gravitational forces in determining the rolling tendency of the droplets.

The roll-off angle is observed to be very high on the single-roughness surfaces. For SR-2 (b/a = 0.92), the roll-off angle is 51° ± 3°, while for SR-1 (b/a = 0.56) and SR-3 (b/a = 0.42), the droplet did not roll off even at an inclination angle of 90°. For the very small droplets employed in the experiments, the gravitational force is unable to overcome the surface tension force acting at the triple contact line of the droplet. This is consistent with the observations of Deng *et al.* [63] who reported that for a b/a ratio less than 1, a 1 μL droplet did not roll off. The test was repeated for SR-1 and SR-3 using a larger droplet volume of 5 μL. In this case the droplet did roll off, but again, at a very high roll-off angle of 37°. For SR-2, the roll-off angle reduced to 32° when a droplet volume of 5 μL was used, which is consistent with the observation of Bhushan and Jung [133].

The droplet rolled off at a much lower tilt angle on the double-roughness surfaces. A 3 μL droplet rolled off at an inclination angle of 8.3° from DR-1, 9.5° from DR-2, and 3.7° from DR-3. Thus the presence of the secondary roughness layer reduces the roll-off angle drastically in all cases. Figure 4.4a shows a comparison between the roll-off angle of water droplets on the single roughness and double roughness surfaces. It is noted that 3 μL droplets were used in all experiments, with the exception that a 5 μL droplet was used for SR-1 and SR-3.

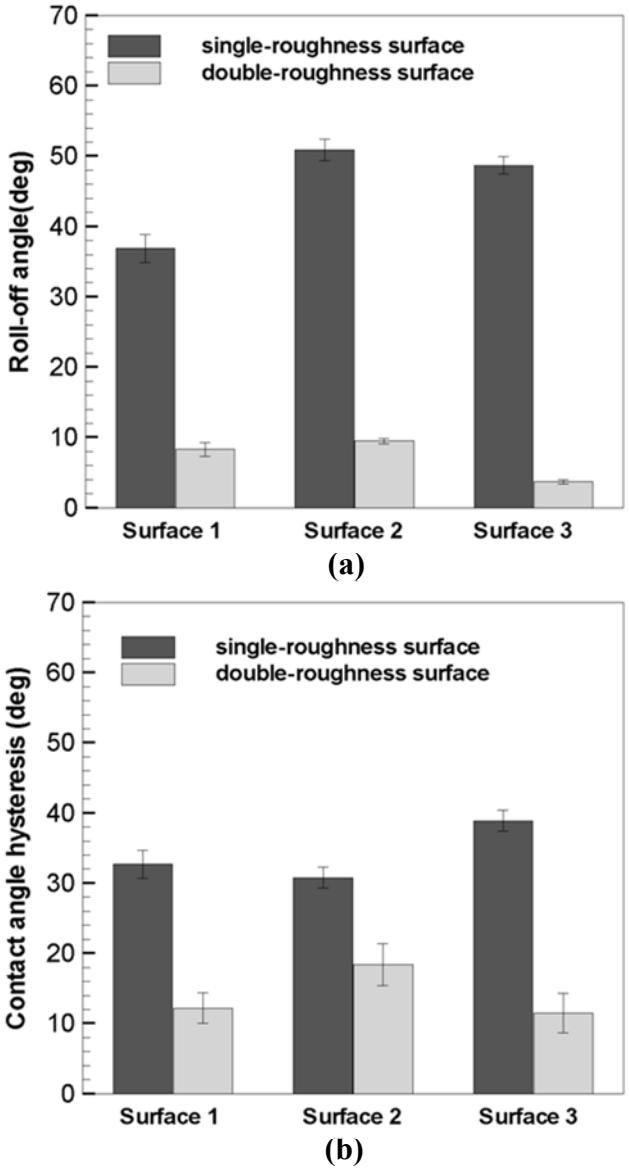

Figure 4.4. (a) The roll-off angle, and (b) contact angle hysteresis for the single-roughness surfaces (SR-1, SR-2, SR-3) and the double-roughness surfaces (DR-1, DR-2, DR-3).

Contact angle hysteresis refers to the difference between the advancing and the receding contact angles of a droplet and depends upon the surface roughness/irregularities. When the substrate is inclined, the advancing and receding angles of the droplet modulate so as to overcome the surface tension force acting at the

triple contact line and the contact line pinning due to surface structures. This explains the lower contact angle hysteresis shown in Figure 4.4b for SR-2 which has a *b/a* ratio higher than SR-1 and SR-3. The contact angle hysteresis (CAH) provides an estimate of the energy loss due to impact/interaction with the structured surface. The CAH is reduced significantly; for the DR-2 surface, this reduction is by 12.4° for a droplet of 3 μL volume (Figure 4.4b). The CAH is due to the pinning of the contact line on some of the sub-micron roughness features during initiation of rolling. The temporal evolution of the advancing and the receding contact angles on the double-roughness surfaces prior to roll-off illustrates that the advancing contact angle remains almost fixed at its static contact angle value while the receding contact angle decreases prior to the droplet roll-off (Figure 4.5). For the single-roughness surfaces, the advancing contact angle increases while the receding contact angle decreases before the droplet starts rolling.

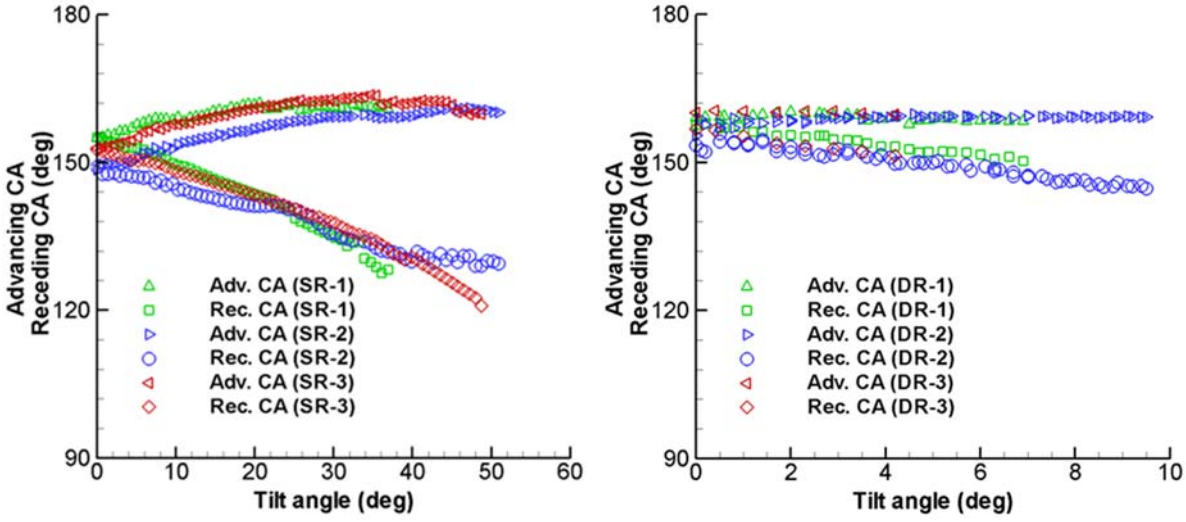

Figure 4.5. Temporal evolution of advancing and receding contact angles of the droplet during roll-off on single-roughness surfaces (SR-1, SR-2, SR-3) on the left and double-roughness surfaces (DR-1, DR-2, DR-3) on the right.

4.2.2 Droplet evaporation

The double-roughness surfaces were further characterized via droplet evaporation experiments under controlled environmental conditions without bottom heating as previously described. An initial droplet volume of 3 μL was used in all the experiments. The experimental observations are reported in terms of the non-dimensional contact diameter (normalized with respect to the initial contact diameter) and contact angle of the droplet as it evaporates. Figure 4.6a and Figure 4.6b show the time evolution of the evaporating droplet on SR-1 and DR-1, respectively. The experimental observation are reported in terms of the non-dimensional time τ; $\tau = t/T$, where t is the time instant and T is the total time taken for the complete evaporation of the droplet.

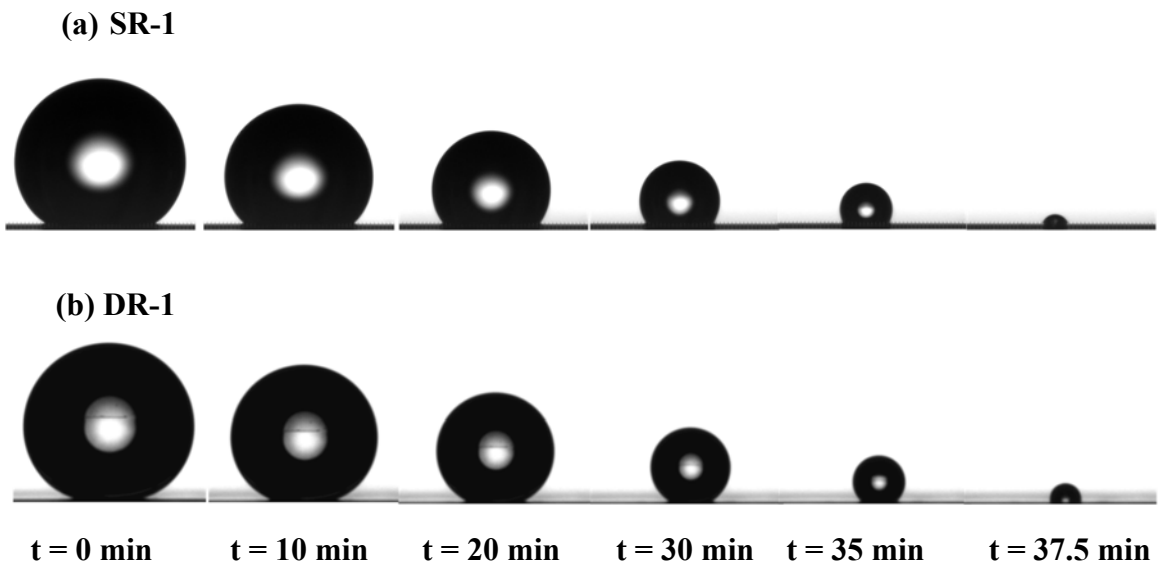

Figure 4.6. Instantaneous images of an evaporating sessile droplet placed on (a) SR-1, and (b) DR-1.

The droplet evaporation on the single-roughness surfaces (SR-1, SR-2, and SR-3) occurred in three distinct phases: constant contact area mode, constant contact angle mode and the mixed mode (Figure 4.7a, Figure 4.8a) as discussed in [92]. In the first phase the droplet contact angle reduces while the droplet contact line is pinned. Subsequently the contact line is de-pinned; the droplet interface starts sliding with a constant contact angle. The interesting observation here is that sliding of the contact line begins when the contact angle is equal to the receding contact angle. This observation is similar to that in the case of hydrophilic surfaces [9] and smooth hydrophobic surfaces. For all the three surfaces under consideration this angle is in close agreement with receding angles obtained from the roll-off experiments (Table 4.4). In case of the single-roughness surfaces the droplet remains in the Cassie state while evaporating except at the very end of the process when the droplet enters the air gaps and goes into the Wenzel state. Such an effect is delayed with two-tier roughness.

On the double-roughness surfaces, the droplet evaporates in the mixed mode, that is, the contact diameter as well as the contact angle change continually during the entire evaporation process. The change in contact angle is minimal; on DR-2, the CA varies from 165° to 157° till $\tau = 0.87$, after which the contact angle rapidly reduces. For DR-1, the contact angle reduces to 142° (corresponding to $\tau = 0.89$) in contrast to the behavior of SR-1 in which the contact angle decreases to 125° within a time of $\tau = 0.41$. Hence the reduction in contact angle is smaller compared to that of the single-roughness surfaces (Figure 4.8, Figure 4.9). The contact diameter has a continuous sliding motion as illustrated by the time evolution of the surface profiles in Figure 4.7. The contact angle behavior is qualitatively similar to that observed on lotus leaf surfaces [95].

Figure 4.7 shows the superposed images of droplet profiles to illustrate the behavior of the wetted diameter of the droplet as it evaporates on the two different types of surfaces (SR-2, DR-2). As can be seen from Figure 4.7, the droplet contact diameter continuously shrinks while evaporating on the double-roughness surface, whereas the contact line is pinned during the first phase on the single roughness surface. The asymmetry in the latter case (SR-2) is due to pinning of droplet contact line on one side. Among the three double roughness surfaces considered in the study, DR-2 exhibits the minimum resistance to sliding of the contact line while evaporating (Figure 4.9).

Table 4.4. Comparison of the contact angle corresponding to the initiation of sliding of droplet interface and the receding contact angle.

Single-roughness surface	**Contact angle corresponding to contact line sliding during evaporation (deg)**	**Receding contact angle from roll-off experiments (deg)**
SR-1	125	128
SR-2	133	129
SR-3	122	122

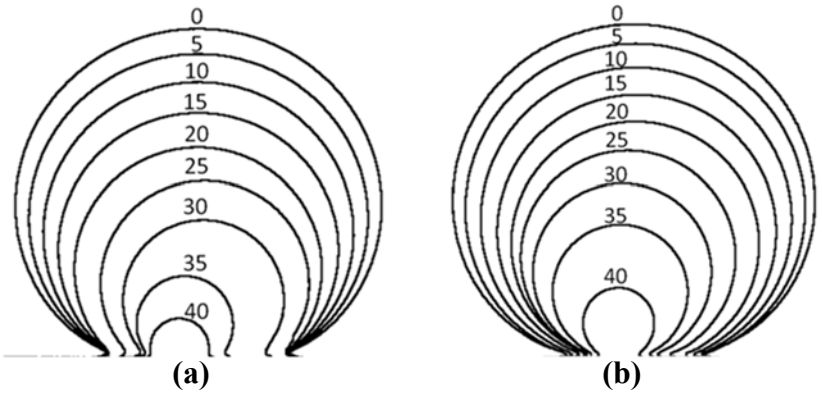

Figure 4.7. Evolution of the surface profile of a droplet evaporating on (a) SR-2 and (b) DR-2 (the numbers represent the time instant in min).

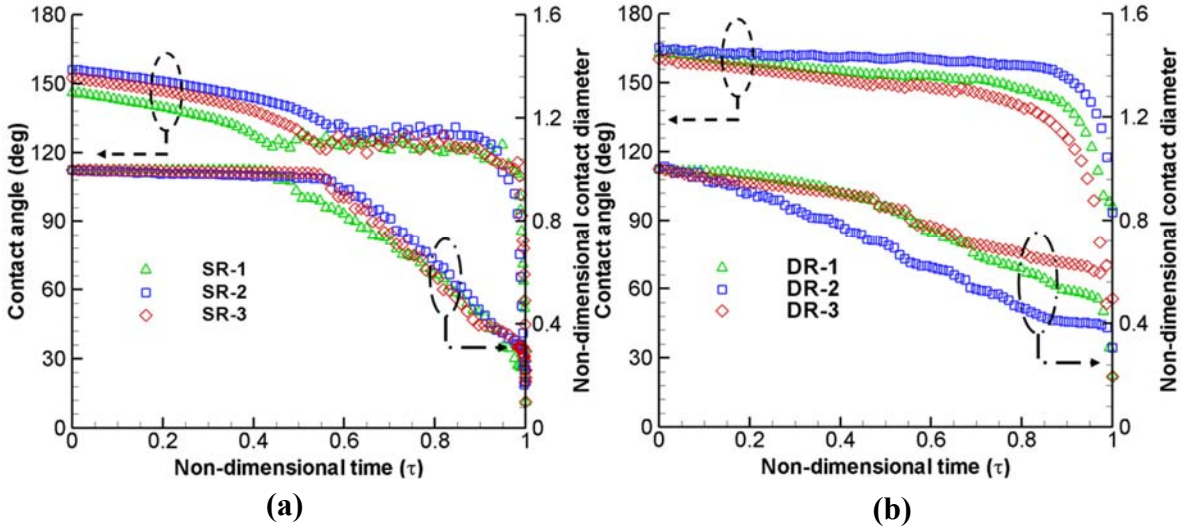

Figure 4.8. Variation of contact angle and contact diameter with respect to non-dimensional time (τ) during evaporation on (a) single-roughness and (b) double-roughness surfaces.

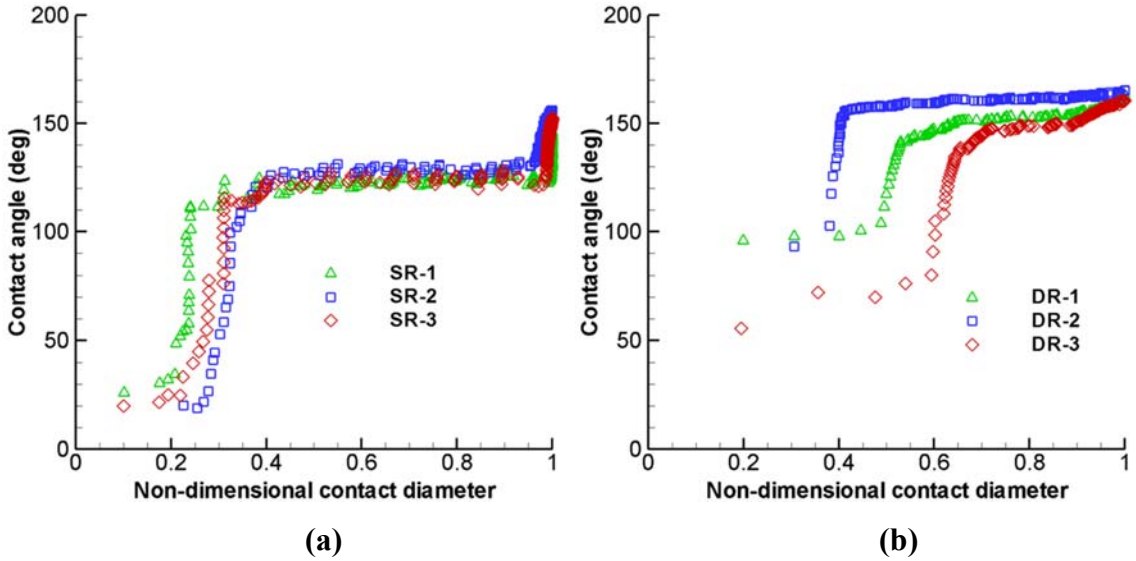

Figure 4.9. Variation of contact angle with non-dimensional contact diameter on (a) single-roughness and (b) double-roughness surfaces.

4.2.3 Droplet Impingement Dynamics

Droplet impingement is the most demanding test of the water repellency of a surface under dynamic conditions. During droplet impingement on a structured surface the

forces acting on the droplet that are responsible for wetting the air gaps are the Laplace pressure (P_L) and the Bernoulli or dynamic pressure (P_D), which can be written as

$$P_L = 2\gamma / R \tag{4.2}$$

$$P_D = \frac{1}{2}\rho V^2, \tag{4.3}$$

where γ is the surface tension of the liquid, R is the radius of the droplet, ρ the density of the liquid, and V is the velocity of the droplet just before impact. The capillary pressure (P_c) of the air gap in the surface offers the main resistance to droplet impalement of the surface and is inversely related to the space between the pillars,

$$P_C = -\gamma \cos\theta_0 \frac{4a}{p^2 - a^2}, \tag{4.4}$$

where θ_0 is the initial contact angle, a is the width of the pillars and p is the pitch. The transition criterion from the Cassie to Wenzel states upon droplet impingement is determined by the relative magnitude of P_C, P_L, and P_D. While surfaces with larger solid fraction (ϕ) have higher capillary pressure owing to the decreased air gap, the larger solid fraction also results in a lower contact angle and a lower roll-off tendency of the droplet on such surfaces as observed in the roll-off experiments. It is therefore essential to select an optimum value of ϕ while designing surfaces for higher contact angle and the required water repellency. The presence of a second layer of roughness elements helps enhance the static contact angle and water repellency of surfaces.

The study of droplet impact was carried out on the six superhydrophobic surfaces using droplets of volume 4.40 ± 0.25 μL in all the tests and impingement heights of 10 mm and 100 mm. The relative importance of the kinetic energy of the impinging droplet

and the surface tension force may be compared using the Weber number [78] defined as $We = \rho V^2 R / \gamma$. For the droplet impingement heights of 10 mm and 100 mm, *We* is equal to 2.8 and 27.6, respectively.

The behavior of the droplet upon impact can be understood based on two main stages. In the first stage, the droplet interface advances to attain the maximum wetted diameter. During this phase the kinetic energy of the droplet is stored as deformation energy in the droplet. In the second stage, the droplet retracts and the stored energy helps it rebound off the surface. The first stage (spreading of the droplet) is an inertia-driven phenomenon. Subsequent retraction and bouncing of the droplet off the surface is the basic test for the water repellency of the surface. Figure 4.10 shows images of the droplet at different instants when the droplet impingement height is 10 mm. For this impingement height with *We* = 2.8, the droplet bounced off both the single- and double-roughness surfaces, but there are differences between these sets of surfaces in terms of the contact angle of the droplet while it is retracting on the substrates, the contact time (total time the droplet is in contact with the substrate), and the droplet height attained after it bounces back.

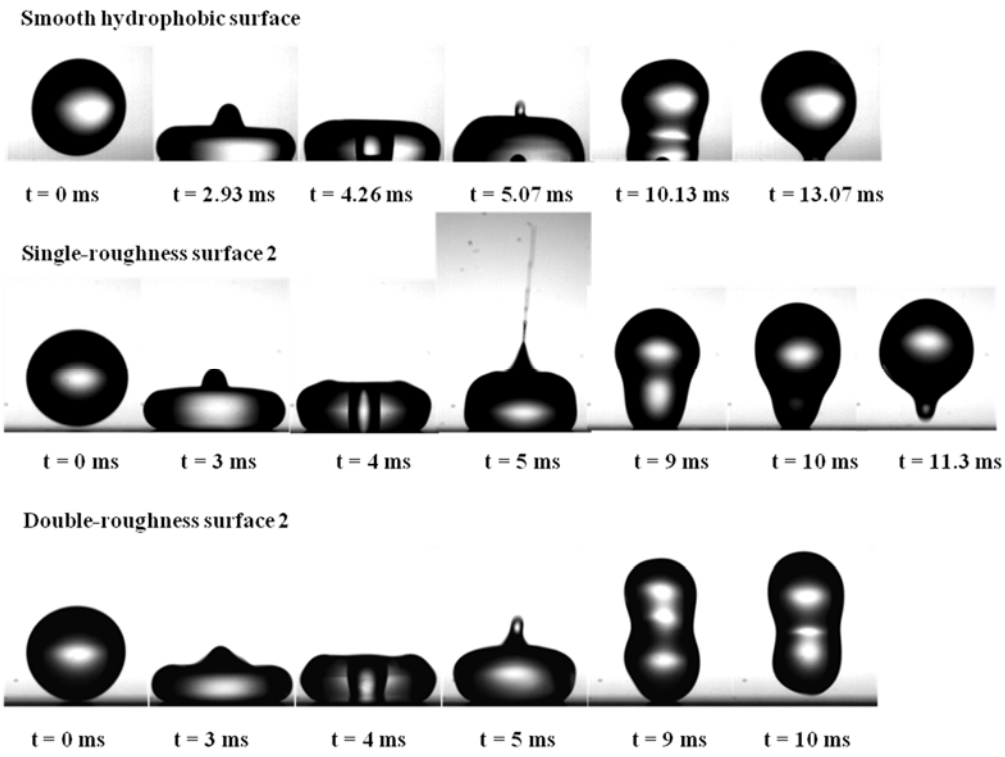

Figure 4.10. Images of the droplet profile at different time instants upon impingement from a height of 10 mm on the (a) hydrophobic surface, (b) SR-2, and (c) DR-2.

Figure 4.11 shows the temporal variation of the wetted diameter of the droplet when it is in contact with the surface corresponding to the impingement height of 10 mm. The time instant at which the droplet is just about to touch the substrate is taken as the initial time instant (t = 0). The droplet takes 2.67 ± 0.33 ms to reach its maximum wetted diameter irrespective of the surface parameters and the maximum wetted diameter is approximately equal to 1.2 times the droplet diameter as shown in Figure 4.11. However, the rate at which the interface of the droplet retracts before bouncing off the surface varies depending on the nature of the surface. This reflects the correlation between the contact angle hysteresis and the residence time of the droplet on the surface during impact. The droplet takes the least time to detach from surface DR-2 (t = 10 ms) and the

contact time is maximum for SR-3 (t = 12.3 ms). The higher the CAH, the longer is the time the droplet takes to detach from the substrate. For tests with the 10 mm drop height, the droplet takes 12.27 ± 0.76 ms to bounce off the single-roughness surface whereas the time is reduced to 10.33 ± 0.67 ms for the double-roughness surfaces (DR-1, DR-2, DR-3). This difference is mainly attributed to the higher energy loss upon impact on SR surfaces (resulting from greater CAH) as compared to DR surfaces. As stated earlier, the hysteresis is greater when only one tier of roughness elements is present, with a correspondingly higher loss of energy. The contact time varies between surfaces and is slightly different from the characteristic time scale (based on the balance between inertia and capillarity) given as $\tau = (2.6 \pm 0.1)\left(\rho R^3 / \gamma\right)^{1/2}$ by Okumura et al. [135]. The characteristic time scale for the droplet is 10.1 ms. The deviation from this time scale primarily in case of the single roughness surfaces is mainly because of the contact angle hysteresis on the surfaces. This is because the energy loss due to contact angle hysteresis is neglected in the derivation of the contact time. A more sparse distribution of pillars than those considered in the present work would yield contact times closer to the characteristic time scale due to the corresponding decrease in the contact angle hysteresis, as has also been observed by Li *et al.* [136].

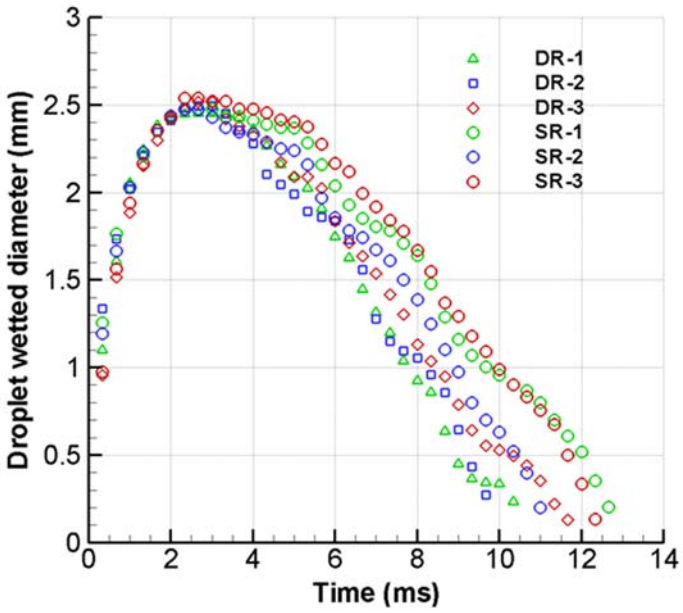

Figure 4.11. Variation of the wetted diameter of the droplet on the SR and DR surfaces corresponding to the droplet impingement height of 10 mm.

The other difference between the single and double-roughness surfaces is observed in the contact angle that the droplet interface makes with the substrate while retracting, and the wetted diameter of the droplet just prior to detachment from the surface. Table 4.5 summarizes the contact angle and the wetted diameter of the droplet before it detaches from the double-roughness and single-roughness surfaces. The droplet bounces off the hierarchical surfaces at a much higher contact angle than in case of single-roughness surface, thus indicating a Cassie jump. This further explains the lower energy loss of the droplet upon impact on the double roughness surfaces. The lower wetted diameter and the lower contact angle prior to detachment indicates the pinch-off phenomenon on the single roughness surface (Figure 4.10b) which is not seen in case of the double-roughness surfaces.

Table 4.5. Droplet contact angle and wetted diameter prior to detachment from the substrate.

Double-roughness surface	Contact angle prior to detachment (deg)	Wetted diameter (mm)
DR-1	146.5	0.23
DR-2	144.7	0.27
DR-3	135	0.13
SR-1	124.4	0.20
SR-2	125.3	0.20
SR-3	113.9	0.13

The coefficient of restitution is defined as $COR = \sqrt{\frac{h_2}{h_1}}$ where h_2 is the height to which the droplet bounces up and h_1 is the initial height from which the droplet is released. h_2 is given by the maximum distance between the center of mass of the droplet bouncing off the surface and the substrate. The coefficient of restitution of a surface is used as a quantitative measure of the reduction in energy loss of the droplet on the double-roughness surface. Figure 4.12 shows the maximum height attained by the droplet when it is dropped from a height of 10 mm on to the DR surfaces, SR surfaces, and a smooth surface (silicon wafer coated with Teflon). The droplet height follows a parabolic profile with respect to time after rebounding from the surface. The droplet oscillates in air (determined in terms of the position of its center of mass) after bouncing off the surface, suffering energy loss due to viscous dissipation as observed by Richard and Quéré [78]. A frequency analysis of the droplet oscillation in air can predict one primary oscillation frequency which varies according to the substrate; such analysis is, however, beyond the

scope of the present study. The height h_2 reached by the droplet after impingement and the corresponding COR are shown in Table 4.6. The COR for DR-2 is 0.67, as compared to a value of 0.54 for SR-2 and 0.52 of SR-1. The droplet did not bounce off the smooth surface at the droplet impingement height of 10 mm (resulting in a COR of 0 for this surface). The higher coefficient of restitution on the double-roughness surfaces as compared to the single-roughness and the smooth surfaces illustrates their superior hydrophobicity. This is a cumulative effect of the reduction in the viscous dissipation of the droplet, and lower contact angle hysteresis during droplet retraction.

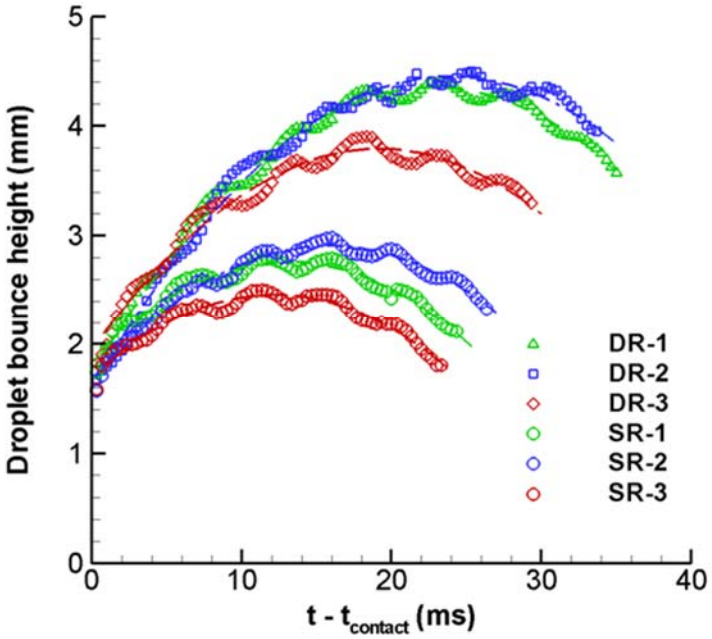

Figure 4.12. Maximum height attained by the droplet after recoil from the surface for a droplet impingement height of 10 mm (t – instantaneous time; $t_{contact}$ – time instant when the droplet just detaches from the substrate).

Table 4.6. Droplet impingement summary on the textured surfaces.

Surface	Coefficient of Restitution		
	1	**2**	**3**
DR	0.66	0.67	0.62
SR	0.52	0.54	0.49

The droplet impingement experiments are repeated with the droplet being released from a height h_1 of 100 mm, resulting in an impingement velocity of 1.4 m/s and a corresponding We = 27.6. Figure 4.13 shows the instantaneous images of droplet impact on DR-3 and SR-3 for this droplet release height; time t is defined as zero when the droplet is just about to touch the substrate. At this impingement velocity the droplet deforms significantly as it spreads on the surface. Figure 4.14 shows the temporal variation of the diameter of the droplet on surfaces 2 and 3, both for single- and double-roughness. As for the smaller release height of 10 mm, the droplet interface attains its maximum wetted diameter and then recedes. The droplet takes 2.27 ± 0.15 ms to reach its maximum wetted diameter in this case. This maximum wetted diameter on both single- and double-roughness surfaces is 2.3 times the initial droplet diameter, which is significantly larger than in the case of the shorter release height (h_1 = 10 mm), where the ratio was 1.2. The subsequent retraction profiles of the droplet interface on the single- and double-roughness surfaces are, however, different, and the secondary roughness on the DR surfaces serves to reduce the contact time.

Prior to bouncing off the surface, the droplet is highly elongated for h_1 = 100 mm, and the non-uniform energy distribution in the droplet results in smaller droplets being detached from the elongated droplet while bouncing off the substrate. While the droplet

bounces off completely from the double-roughness surfaces (at t = 10.4 ms for DR-3), a pinch-off is observed in the case of the single-roughness surfaces: a very small part of the droplet is stuck to the single-roughness surface (SR-3) as shown in Figure 4.13 at t = 12.8 ms. The higher retraction time (difference between the time instant of maximum spread and time instant when the droplet finally detaches from the substrate) on single-roughness surfaces, i.e., 8.13 ms on SR-2 and 10.53 ms on SR-3 compared to 6.73 ms on DR-2 and 8.13 ms on DR-3, indicates the reduction in total energy loss on the double-roughness surfaces fabricated.

Fragmentation occurs at the top of the droplet to form smaller droplets while bouncing off the substrate at this high Weber number (= 27.6). The smaller droplets formed (Figure 4.13) are released at a much higher velocity reaching a much larger height, and are not captured in the window size of the images. Hence the coefficient of restitution, which depends upon the final height of the center of mass of the droplet, is not calculated for this droplet release height.

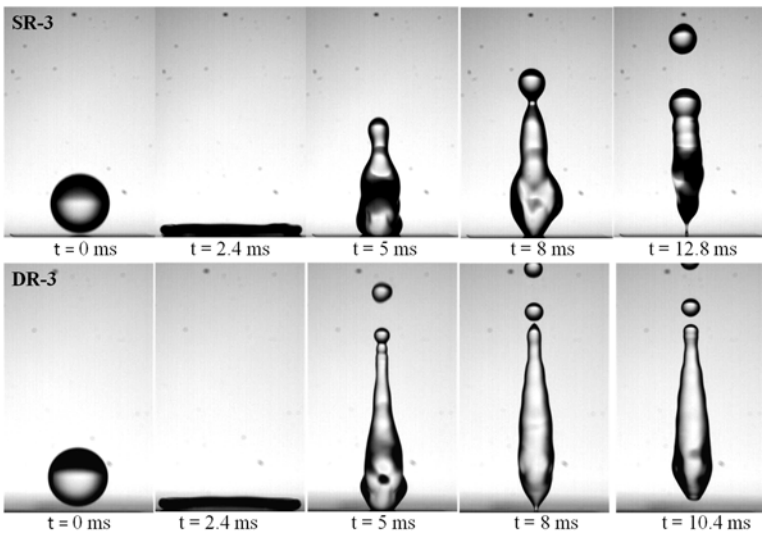

Figure 4.13 Instantaneous images of droplet impingement corresponding to a droplet release height of 100 mm on (a) SR-3, and (b) DR-3.

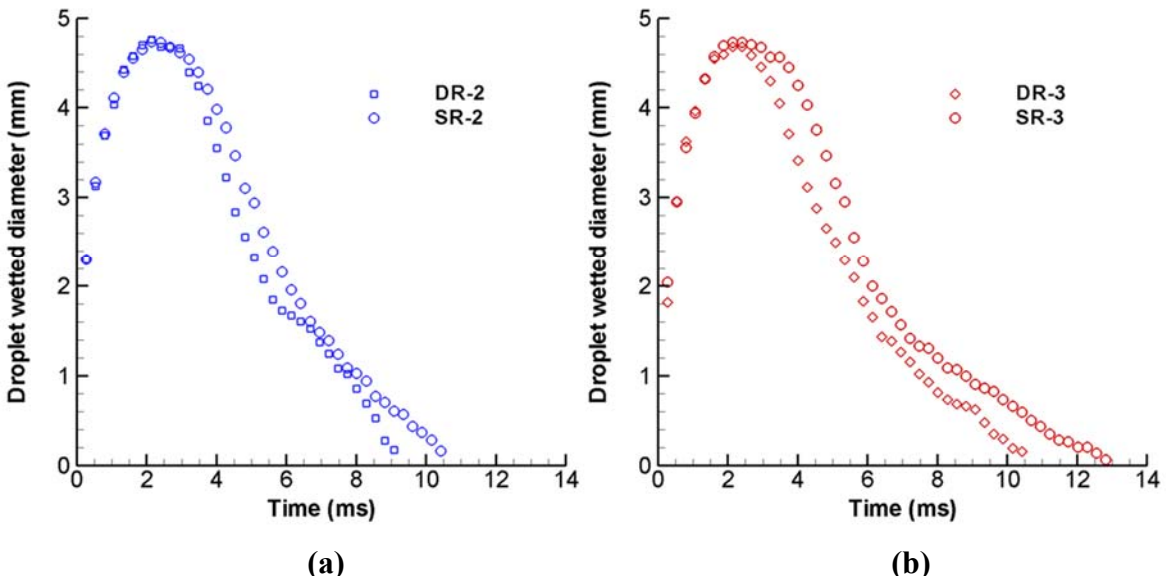

Figure 4.14. Wetted diameter corresponding to the droplet impingement height of 100 mm on (a) SR-2, and DR-2, and (b) SR-3, and DR-3.

4.3 Summary

A simple, one-step fabrication methodology for developing superhydrophobic double-roughness surfaces is presented. A single-step deep reactive ion etch method is employed to fabricate the hierarchical roughness structures; the second layer of roughness caused by the photoresist residue is stable and is an easy way to enhance the surface hydrophobicity. Significant improvement of the surface hydrophobicity is observed in terms of the non-wetting characteristics when the second layer of roughness elements is introduced as compared to surfaces with a single level of roughness in the form of micropillars. Larger static contact angles with a water droplet, smaller roll-off angles, and reduced contact angle hysteresis are demonstrated with the hierarchical surfaces relative to the single-roughness surfaces. The surfaces are also shown to better

withstand the impact pressure from an impinging water droplet. A coefficient of restitution of approximately 0.65 is achieved with the double-roughness surfaces when the droplet impingement height is 10 mm. The double-roughness nature of the fabricated surfaces preserves the robustness of the air gap between pillars even under impingement of a droplet released from a height of 100 mm.

CHAPTER 5. HYBRID SURFACE DESIGN FOR ROBUST SUPERHYDROPHOBICITY

The focus of research presented here is not only on the development of surfaces that exhibit superhydrophobic properties, but also on ensuring that they are robust and can maintain the superhydrophobic state against external forces that tend to induce wetting. The project was done in collaboration with Marie Theresa, an undergraduate intern from Karlsruhe Institute of Technology. Germany. In this chapter, we present and discuss two major findings. First, we show through analysis that *hollow* square pillars used as roughness elements demonstrate a higher anti-wetting pressure as compared to solid pillars of similar dimensions, both with communicating air gaps. Second, we characterize the hybrid surfaces fabricated in this work in terms of the static contact angle of a sessile droplet, and test their robustness with droplet impingement tests. We explain the droplet impingement behavior on the superhydrophobic surfaces using a dynamic pressure model. We then use the experimental results to determine the water hammer pressure during impact. We show the water hammer pressure acting on the superhydrophobic substrate during droplet impingement to be dependent on the surface morphology. The material presented in this chapter was published in *Langmuir* (**28**(25), pp. 9606–9615, 2012) [137].

5.1 Hybrid Superhydrophobic Surfaces: Design and Fabrication

The intrinsic contact angle, or Young's contact angle (θ_Y), of a droplet when placed on a smooth surface is given by the relative surface energies of the solid-liquid (γ_{SL}), solid-air (γ_{SA}), and liquid-air (γ_{LA}) interfaces as

$$\theta_Y = \cos^{-1}\left(\frac{\gamma_{SA}-\gamma_{SL}}{\gamma_{LA}}\right). \tag{5.1}$$

On a structured surface, on the other hand, the droplet contact angle depends on whether it is in a Cassie or a Wenzel state on the substrate; this droplet state can be predicted using an energy minimization approach [134]. A droplet gently deposited on a rough surface that favors the Cassie state energetically stays in the Cassie state with a high contact angle as given by [134] as

$$\theta_c = \cos^{-1}\left(-1+\phi\left(1+\cos\theta_Y\right)\right), \tag{5.2}$$

where θ_Y is Young's contact angle of the droplet on a smooth surface (= 120^0 for a water droplet on a Teflon coated smooth surface [71]), and ϕ is the solid area fraction defined as the ratio of the projected area to the base area of the surface $\left(\phi = \frac{a_o^{\,2}}{p^2}\right)$, with a_o being the feature size and p the pitch of the pillars (Figure 5.1a). The apparent contact angle of a droplet in the Cassie state thus depends on Young's contact angle and the solid fraction. An alternative situation is realized when the droplet homogeneously wets the micropillars and is in the Wenzel state; the contact angle in this case is given by

$$\theta_W = \cos^{-1}\left(r_m \cos\theta_Y\right), \tag{5.3}$$

in which r_m is the roughness given by $r_m = 1 + \frac{4a_o h}{p^2}$, and h is the height of the roughness elements.

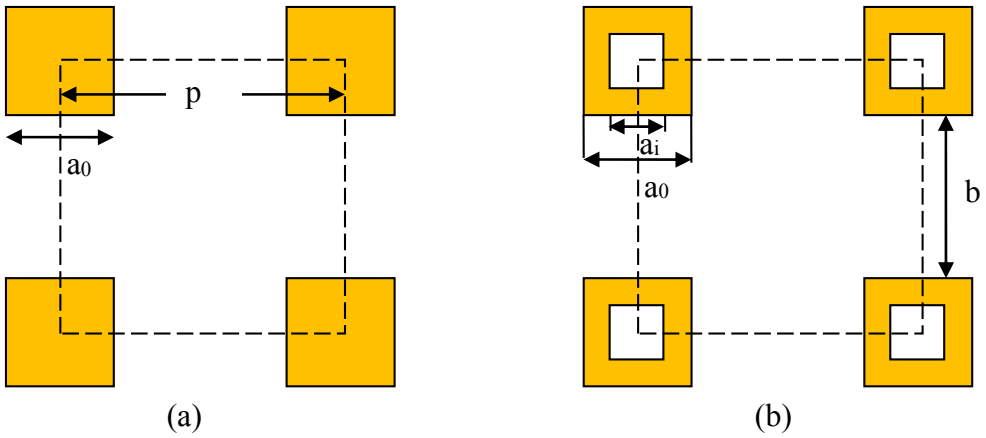

Figure 5.1. Schematic of (a) superhydrophobic surfaces with communicating air gaps, and (b) hollow-pillared hybrid surfaces.

It is possible to attain two different contact angles (corresponding to the Cassie and Wenzel states) on the same rough surface depending on how the droplet is formed [134]. The important condition for the Cassie state to be the more stable configuration on a superhydrophobic (SH) surface is for the Cassie state of the droplet to have a lower energy than the Wenzel state [35, 134]. That is, the contact angle obtained from the Cassie expression (Eq. (5.1)) must be smaller than that obtained using the Wenzel expression (Eq. (5.2)) [134].

The non-wetting Cassie state of a SH surface is attributed to the high capillary pressure (P_C) resulting from their small-pore structure. The capillary pressure depends on Young's contact angle (θ_Y) of the droplet on a smooth surface, the capillary perimeter (L_c) and area (A_c), and is given as [69]

$$P_C = -\gamma_{LA} \cos\theta_Y \frac{L_C}{A_C}. \tag{5.4}$$

in which γ_{LA} is the surface tension of the liquid (= 0.072 N/m for water). For a structured surface with a solid-pillared pattern as shown in Figure 5.1a, the capillary pressure takes the form

$$P_C = -4\gamma_{LA} \cos\theta_Y \frac{\phi}{a_o(1-\phi)}. \tag{5.5}$$

The transition between the Cassie and Wenzel states was explained in terms of the energy barrier between the two states by Patankar [134]. The energy barrier may be understood as the energy required to wet the sides of the surface elements on SH surfaces [138]. An alternative approach is to interpret the energy barrier in terms of the work done by capillary force, which is the product of capillary pressure and liquid-air interfacial area (= $p^2 - a_o^2$), to displace the air gaps through a height h within the roughness elements. For the SH surface geometry of Figure 5.1a, with feature size a_0 and height h, the energy barrier between the Cassie and Wenzel states of the droplet corresponding to one pillar (area p^2) is given by

$$E_C - E_W\big|_{per\ pitch} = P_C(A_C \times h) = -4\gamma_{LA}\cos\theta_0 \frac{\phi}{a_0(1-\phi)}\left[(1-\phi)p^2 h\right] = -4\gamma_{LA}\cos\theta_0 a_0 h. \tag{5.6}$$

The total energy barrier between the two states of a droplet of radius Rc (assuming the space beneath the droplet to be wetted homogeneously) may be determined by multiplying the energy with the total number of pillars (n) beneath the droplet ($n = \pi R_c^2/p^2$) as

$$E_C - E_W = -4\gamma_{LA}\cos\theta_0 a_0 h \frac{\pi R_C^{\,2}}{p^2} = -4\pi R_C^{\,2}\gamma_{LA}\cos\theta_0 \phi \frac{h}{a_0}. \tag{5.7}$$

This expression is analogous to the energy barrier inherent in the change in surface energy during Cassie-to-Wenzel transition as proposed by Patankar [134] (simplified form of equation 6 in reference [134]). The energy barrier between the Cassie and Wenzel state can be overcome by the kinetic energy of the droplet striking such a surface. Under dynamic conditions, additional pressures come into play at the interface: the Bernoulli pressure $\left(P_D = \frac{1}{2}\rho V^2 \right)$ due to the velocity of the droplet during impingement, and the shock pressure or the water hammer pressure $\left(P_{WH} = k\rho cV \right)$ produced by the sudden stoppage of the droplet by the substrate. The water hammer pressure is limited to a small area compared to the projected area of the droplet and this area depends on the size of the droplet and velocity of impingement [81]. The value of 0.2 for the coefficient *k* used in the literature gives an extreme over-estimate of the water hammer pressure acting on the surface. P_{WH} acting during the impingement of a droplet on a textured superhydrophobic surface is therefore determined experimentally using a pressure balance-based approach in the present work, as discussed in a subsequent section.

In order to prevent the droplet transition to homogeneous wetting of the surface, the anti-wetting pressure must exceed the wetting pressure, namely the sum of the dynamic pressure and the water hammer pressure, *i.e.*, $P_C > P_D + P_{WH}$. Otherwise, either partial or total infiltration of the air gap by the impinging droplet occurs [63]. Figure 5.2 illustrates these two possibilities following the impingement of a droplet on a superhydrophobic surface.

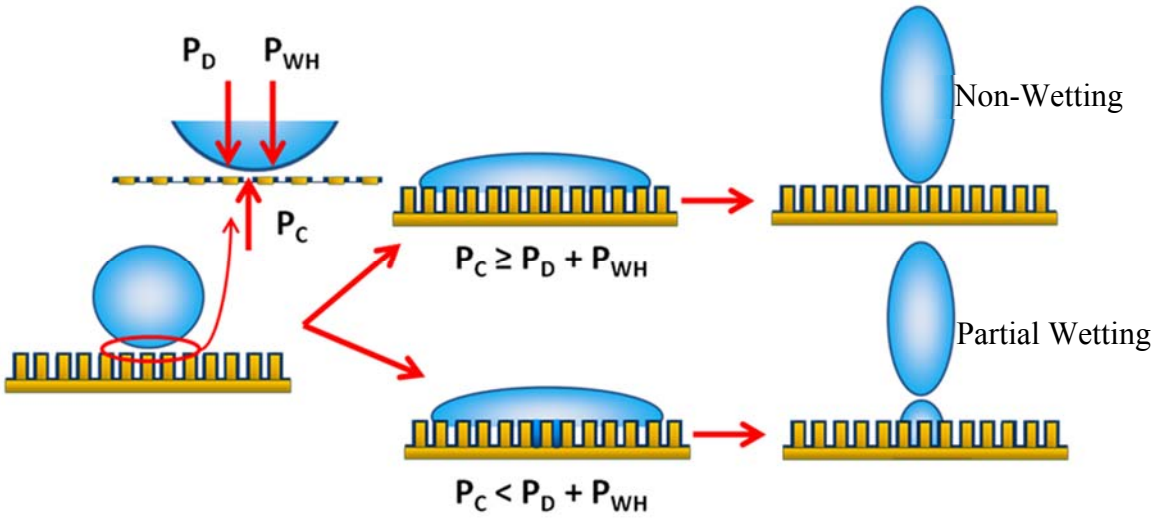

Figure 5.2. Schematic illustration of the alternative transition events during droplet impingement on a superhydrophobic surface.

The capillary pressure may be enhanced by decreasing the feature size (Eq. (5.5)) [139]. The feature height must exceed a minimum value to avoid a transition to droplet impalement caused by the curved surface of the droplet touching the substrate [58]. Tall, slender pillars would ensure superhydrophobicity, but may not be sufficiently robust. At the microscale, an alternate approach is to modify the surface design so as to increase the net anti-wetting pressure. In the remainder of this section, we describe the design of hollow-pillared hybrid surfaces based on this approach, and compare their characteristics in terms of static contact angle and anti-wetting pressure with those of surfaces with solid pillars with only communicating air gaps.

The hollow-pillared hybrid surface designed in this work consists of a square array of pillars with square holes at the centers of each of the pillars that serve to trap air in the holes. The rationale is to use both the communicating and non-communicating air gaps to enhance the anti-wetting property of the surfaces. Figure 5.1b shows the layout of

such a surface: a_0 and a_i represent the outer and inner dimensions of the square pillars, p is the pitch of the pillars, and b is the gap between the pillars. In the present study, a_i is maintained at two-thirds of a_0 for all the surfaces fabricated. For the experimental verification tests, six different substrates are fabricated with varying surface roughness and solid fraction as will be discussed in detail in a following section.

5.1.1 Static Contact Angle on Hybrid Surfaces

The static contact angle that may be achieved with the hollow-pillared hybrid surfaces (Figure 5.1b) is compared against that with a solid-pillared surface (Figure 5.1a) of equivalent pillar outer dimension, a_o. The solid fraction (ϕ) and the surface roughness (r_m) of the hybrid surface are given by

$$\phi = \frac{a_o^{\,2} - a_i^{\,2}}{p^2} \tag{5.8}$$

$$r_m = 1 + \frac{4(a_o + a_i)h}{p^2}. \tag{5.9}$$

The use of the non-communicating air gaps reduces the solid fraction, thus increasing the apparent contact angle. He *et al.* [4] formulated an expression for the equilibrium contact angle based on the energy balance between the Cassie and Wenzel states of the droplet. This angle represents the maximum contact angle of a droplet on a particular superhydrophobic surface, and for communicating square structures is given by He *et al*. [4] as

$$\cos\theta_E = -\left[1 + \frac{4\phi h}{a_0}(1-\phi)\right]^{-1}. \tag{5.10}$$

Thus, the equilibrium contact angle of the droplet on the hollow-pillared hybrid geometry is given by

$$\cos\theta_E = -\left[1 + \frac{4\phi h}{(a_0 - a_i)}(1-\phi)\right]^{-1}. \tag{5.11}$$

Comparing Eq. (5.10) and Eq. (5.11) it may be deduced that for a fixed outer feature size (a_o), the equilibrium contact angle (θ_E) is larger for the hybrid surface. Figure 5.3 compares the variation of the contact angle for the Cassie (Eq. (5.2)) and the Wenzel (Eq. (5.3)) states with respect to the solid fraction corresponding to both the hollow-pillared hybrid surfaces and the solid pillar structures. The chosen feature dimensions are a_o = 20 μm and pillar height h = 32 μm, and the solid fraction ϕ is varied by varying the pitch p. The equilibrium contact angle θ_E is the intersection of the Cassie and the Wenzel curves (Figure 5.3). The equilibrium contact angle for the hybrid structure is 167.2^0 and is achieved at ϕ = 0.049; this compares to the values for the solid pillars of 159^0 at ϕ = 0.137. Thus a higher stable contact angle can be obtained using a hollow-pillared hybrid geometry than with solid pillars. It is also noteworthy that hybrid pillars support the Cassie state of a droplet over a larger range of solid fractions (ϕ > 0.049) than do the solid pillars (ϕ > 0.137) for the same a_o.

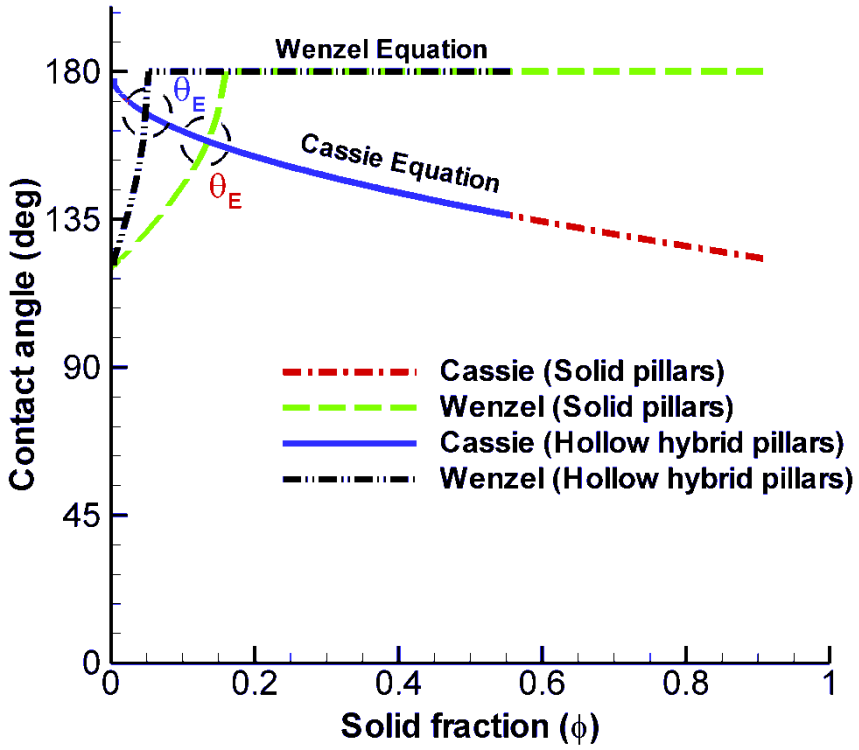

Figure 5.3. The dependence of contact angle on the solid fraction for hollow hybrid pillars and solid pillars. The intersection of the Cassie and Wenzel curves represent the equilibrium contact angle.

5.1.2 Anti-Wetting Pressure Offered by Hybrid Surfaces

The capillary pressure of the surface is also different for the hollow-pillared hybrid pillars proposed here, relative to a solid-pillar structure. From Eq. (5.4), the capillary pressure for the hybrid surface is

$$P_C = -4\gamma_{LA}\cos\theta_Y \frac{(a_o + a_i)}{p^2(1-\phi)} = -4\gamma_{LA}\cos\theta_Y \frac{\phi}{(a_o - a_i)(1-\phi)}. \quad (5.12)$$

The hybrid surface increases the capillary pressure significantly for a given value of solid fraction. Figure 5.4 shows the variation of capillary pressure for the hybrid surface as well as for solid pillars as a function of solid fraction (varying pitch) for a_o = 20 μm. As solid fraction ϕ is increased, the angle obtained using the Cassie equation (Eq. (5.2))

decreases. An increasing solid fraction implies a decrease in air gap size, which results in an increase in capillary pressure. Although this trend can be seen in case of both the surface geometries, the hybrid surface shows a much higher capillary pressure than the solid pillars for a given contact angle. At a solid fraction of 0.4 ($\theta_C \sim 143°$), the capillary pressure *Pc* is 14400 N/m^2 for the hybrid surface but only 4800 N/m^2 for the solid pillars. This is an important factor in the design of robust superhydrophobic surfaces for high anti-wetting pressure without compromising the high contact angle.

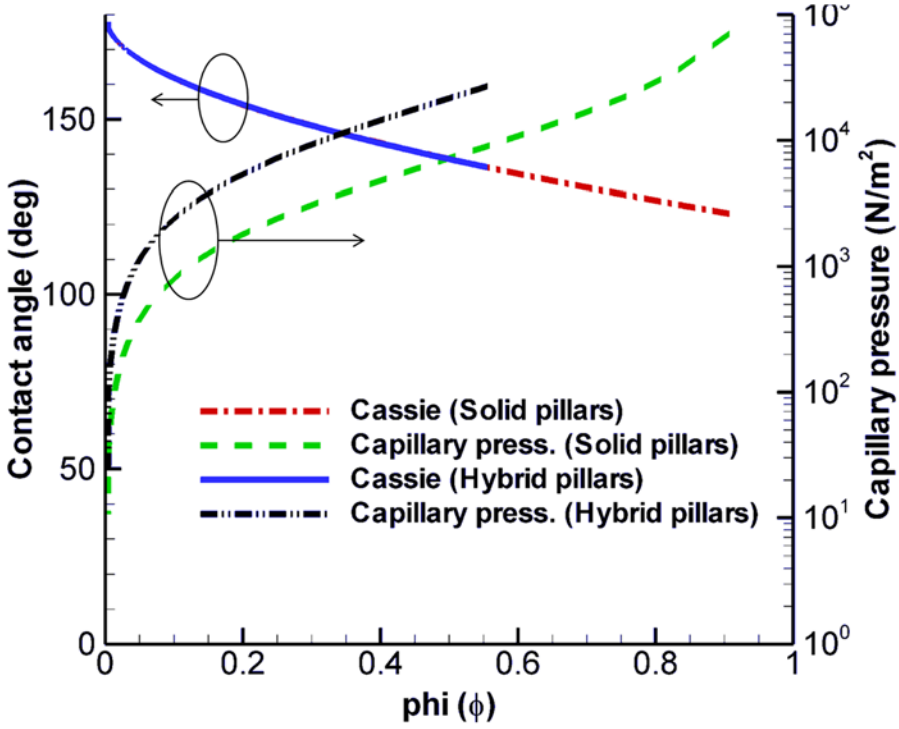

Figure 5.4. Variation of contact angle and capillary pressure with solid fraction for the hollow-pillared hybrid surface and the solid-pillared surface.

5.2 Fabrication of Hollow-Pillared Hybrid Surfaces

Six hybrid surface samples are fabricated in the present work, with the surface parameters selected such that the Cassie state is the stable configuration for a droplet.

The contact angle and the capillary pressure for the six hybrid surfaces are computed from Eq. (5.2) and Eq. (5.12) respectively to be significantly higher than the values on corresponding solid square pillars of the same pillar outer dimension (a_0) and pitch (p). Table 5.1 summarizes these surface parameters. All the surfaces were fabricated in the Birck Nanotechnology Center at Purdue University. Silicon wafers with 1 μm oxide layer are used as the substrates. The fabrication process includes spinning of HMDS at 3000 rpm for 10 secs followed by spinning photoresist, AZ 5214 (MicroChem) at 3000 rpm for 30 sec. The wafer is soft-baked at 110^0 C for 65 s and exposed for 7 sec at a power of 23 mW/cm^2 (Karl Suss MJB-3 mask aligner). The reversal bake is carried out at 110^0 C for 2 min and 40 sec, followed by a flood exposure for 60 sec. The photoresist is developed using AZ 400K:DI water at a dilution ratio of 1:4 for 30 sec. The photoresist is used to pattern SiO_2 using reactive ion etching (STS AOE). Subsequently, the photoresist is removed using acetone and methanol cleaning steps and the patterned oxide layer acts as the etch mask for silicon patterning using a deep reactive ion etch (DRIE) process. A low etch rate of 1.7 μm/min is chosen for anisotropic etching to achieve the design feature size. The DRIE parameters are listed in Table 1.

Table 5.1. DRIE process parameters.

Parameters	**Value**	
	etching	**passivation**
Switching time	6 sec	4 sec
Gas flow	160 sccm SF_6	85 sccm C_4F_8
RF coil power	900 W	700 W
RF Bias power	25 W	20 W

After DRIE etching, the oxide layer is removed using a buffered oxide etch. The structures are subsequently spin-coated with 0.2% Teflon AF1600 (DuPont, Wilmington, DE) in FC77 solution at 1500 rpm for 30 sec resulting in a conformal coating of ~ 50 nm. The substrates are then baked at 90° C for 45 min. SEM images of the hollow-pillared hybrid surfaces before spinning Teflon are shown in Figure 5.5.

Table 5.2. Surface parameters of the hollow-pillared hybrid substrates fabricated.

Surface	a_0 **(μm)**	a_i **(μm)**	**Pitch (μm)**	ϕ	r_m
1	15	10.0	39	0.08	2.64
2	20	13.3	45	0.11	2.65
3	13	8.7	25	0.15	4.47
4	20	13.3	34	0.19	3.88
5	27	18.0	42	0.23	3.55
6	33	22.0	47	0.27	3.48

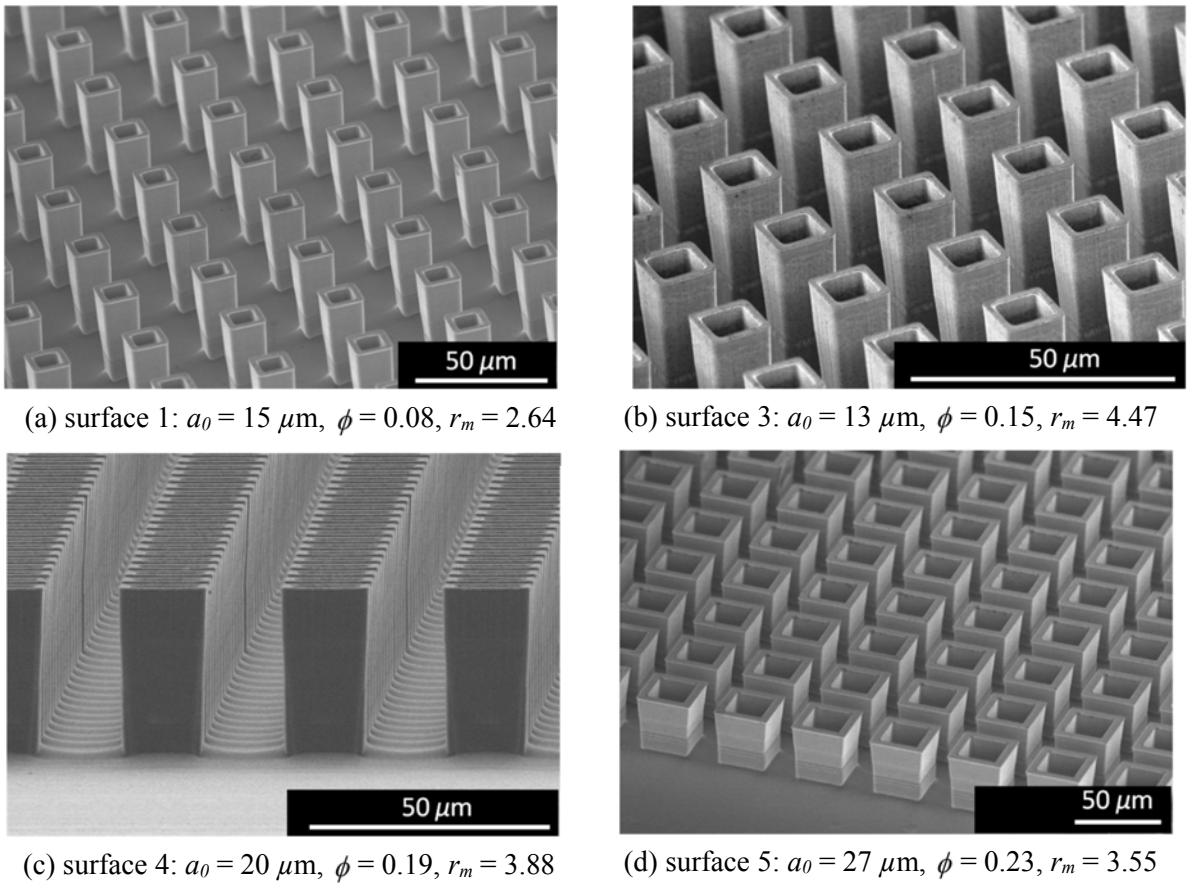

(a) surface 1: a_0 = 15 μm, ϕ = 0.08, r_m = 2.64

(b) surface 3: a_0 = 13 μm, ϕ = 0.15, r_m = 4.47

(c) surface 4: a_0 = 20 μm, ϕ = 0.19, r_m = 3.88

(d) surface 5: a_0 = 27 μm, ϕ = 0.23, r_m = 3.55

Figure 5.5. Scanning electron microscopy (SEM) images of four representative hollow hybrid superhydrophobic surfaces fabricated in the present work: (a) surface 1 (b) surface 3 (c) surface 4, and (d) surface 5.

5.3 Experimental Setup

The capillary length of a water droplet defined as $\left(\gamma/\rho g\right)^{1/2}$ is 2.7 mm. For droplet diameters smaller than this length, the flattening effect of gravity on the droplet may be neglected and a spherical geometry assumed. A 3 μL deionized water droplet is used for the static contact angle measurements such that the length scale (diameter) is approximately 1.79 mm and is less than the capillary length [71]. A goniometer (Model 290 Ramehart) is used for imaging the droplet and determining its contact angle using a

circular-fit algorithm. The spherical symmetry of the droplet allows for such a fit to determine the contact angle. The droplet impingement experiments are carried out with a droplet of 4.5 μl volume. Figure 4.3 shows a schematic diagram of the experimental setup used for the droplet impingement experiments. The images are recorded using a high-speed camera (Photron 1024 PCI) at 3,000 to 3,750 fps. Each experiment is carried out at least three times.

The reported droplet static contact angle is obtained as the average of the contact angles measured at different locations on the substrate. The droplet behavior upon impingement on the hybrid surfaces is seen to be extremely repeatable, mainly because of the precise control of the impingement settings and the uniformity of the substrates fabricated. For droplet impingement experiments, representative results are presented in terms of the contact angle and the droplet wetted diameter. Image processing is done using an in-house Matlab [119] code and Image J software (an image processing program available from the National Institutes of Health).

5.4 Results and Discussion

5.4.1 Static Contact Angle

The static contact angles for the six test surfaces, measured using a circular curvefit algorithm to the goniometer images, are summarized in Table 5.3. The experimental values of contact angle lie within 96 to 103 percent of the theoretically predicted values (from Eq. (5.2)) showing a reasonably good match. The reported static contact angles are averaged over four sets of experiments. All the hollow-pillared hybrid surfaces fabricated support high contact angles in the range of 153.4° - 157°.

Table 5.3. Predicted and measured values of the static contact angle for hollow-pillared hybrid surfaces.

Surface	Contact angle	
	Theoretical (deg)	**Measured (deg)**
1	163.5	156.3±0.2
2	160.9	156.1±0.9
3	157.7	153.9±0.5
4	154.7	156.3±1.1
5	152.3	155.5±0.2
6	149.7	153.9±0.5

5.4.2 Droplet Impingement

As discussed in an earlier section, the wetting transition upon impact is determined by the relative magnitudes of the Bernoulli pressure (P_D), water hammer pressure (P_{WH}), and capillary pressure (P_C). When a droplet of water impinges on a surface from a height of 50 mm with $a_o = 20$ μm and $\phi = 0.1$, these pressures take magnitudes of $P_C = 1{,}934$ N/m^2, $P_B = 491$ N/m^2, and $P_{WH} = 296{,}740$ N/m^2 (obtained using $k = 0.2$ in the expression for P_{WH} [63]). The water hammer pressure so predicted is orders of magnitude higher than the wetting pressures, and the wetting transition would be expected to occur at a droplet impingement height as small as ≈ 2 μm. In the experiments, however, it is observed that the wetting transition for superhydrophobic surfaces of this geometry occurs when the impingement height is in the range of tens of mm. It is clear that the expression for predicting P_{WH} must be modified.

The droplet impingement experiments not only assess the robustness of the air gaps of the hollow-pillared hybrid surfaces fabricated, but also aid in understanding the

mechanics of the impingement-induced droplet transition on the superhydrophobic surfaces. Experiments were carried out by carefully incrementing the height of impingement in steps of 5 mm until a height was reached at which a part of the droplet goes into the Wenzel state on the surface. The velocity corresponding to this occurrence is termed as the critical velocity. In the following sections we describe the dynamics of the droplet upon impingement on the hybrid surfaces, and propose a modified expression for predicting the water hammer pressure

5.4.3 Droplet Dynamics

This section describes the dynamics of droplets impinging on superhydrophobic surfaces during completely non-wetting (Figure 5.2a) and partial wetting (Figure 5.2b) impact. A droplet of volume ~4.5 μL was used in all the impingement experiments. The relative importance of the kinetic energy of the impinging droplet and the surface tension force may be compared using the Weber number [78] defined as $We = \rho V^2 R / \gamma_{LA}$, where R is the radius of the droplet. The Weber number in our experiments varies between 2.7 and 27.3.

The behavior of the droplet upon impact can be analyzed in terms of two main stages. In the first stage, the droplet interface advances to attain the maximum wetted diameter. During this phase the kinetic energy of the droplet is stored as deformation energy in the droplet. The first stage (advancing phase) is an inertia-driven phenomenon; in the second stage (receding phase), the droplet retracts and the stored energy helps it rebound off the surface. Complete retraction and detachment of the droplet from the superhydrophobic surface is possible only when the air gap within the structures retains its integrity during

impact; this is the basic test for water-repellence of a surface. In this non-wetting case the pressure of the air gap prevents the droplet from going into a Wenzel state and reduces the energy expended during the retraction of the droplet, causing it to bounce off based on the stored energy. Figure 5.6 shows the instantaneous images illustrating the droplet impact on surface 4 with a velocity of 0.99 m/s; *We* = 13.6. The capillary pressure is higher than the net wetting pressure in this case, and the droplet bounces back without wetting the surface.

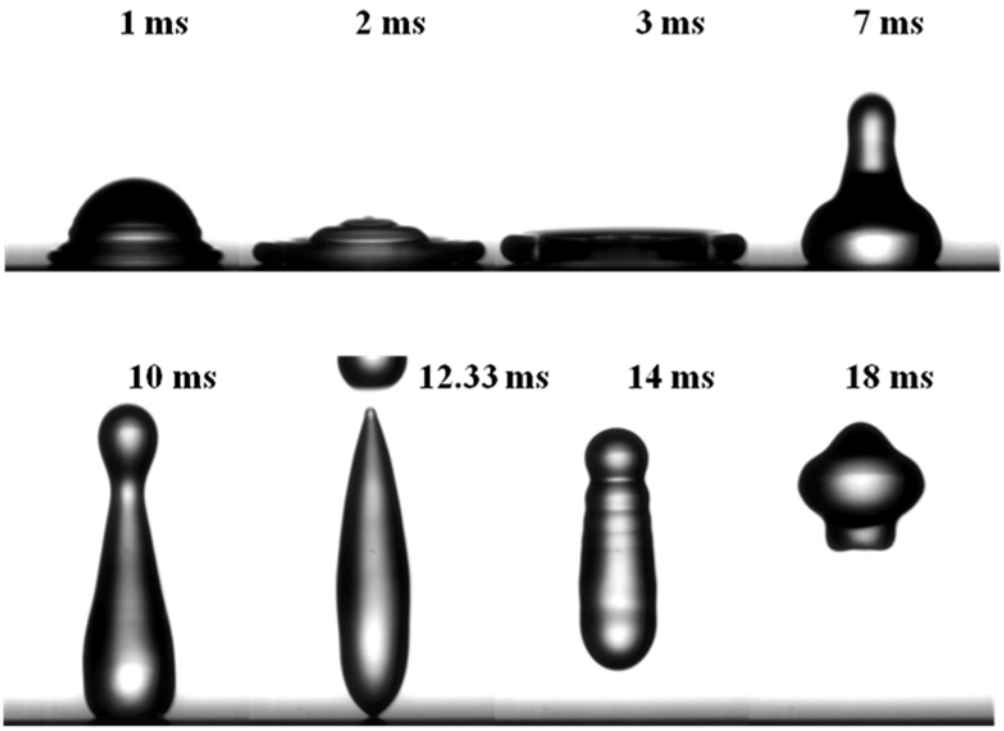

Figure 5.6. Instantaneous images of droplet impact on surface 4 at $V = 0.99$ m/s.

The non-dimensional contact diameter (normalized with respect to the initial diameter of the droplet) as well as the contact angle upon impact of a droplet from a height of 50 mm ($V = 0.99$ m/s, $We = 13.6$) are shown in Figure 5.7 for surface 1 and surface 3 to

illustrate the dynamics of transition of the droplet to the Wenzel state upon impact. Instantaneous images during the droplet impact process are included as insets in the figure; surfaces 1 and 3 are chosen for inclusion in the figure as they display the minimum and the maximum capillary pressures, respectively, out of the six test surfaces designed. For an impingement velocity of V = 0.99 m/s, the droplet undergoes a non-wetting impact on surface 3 and a Wenzel transition occurs on surface 1. The time period from t = 0 ms to t = 2.667 ms corresponds to the advancing phase of the droplet. The effect of the Cassie-to-Wenzel transition on the advancing phase of the droplet (i.e., till the droplet reaches its maximum wetted diameter) is negligible. The droplet reaches almost the same maximum wetted diameter (~ 1.85 times the initial diameter of the droplet) for both wetting (surface 1) and non-wetting impact (surface 3). This may be attributed to the extremely small fraction of the droplet penetrating the air gap compared to the volume of the droplet for impact on all six surfaces. In the case of surface 1, for an impingement height of 50 mm, the transition occurs over an area with radius ~ 0.72 mm (Figure 5.7) and assuming complete transition occurs over this area, the volume of displaced air is 0.048 mm^3, which is approximately 1 percent of the total volume of droplet.

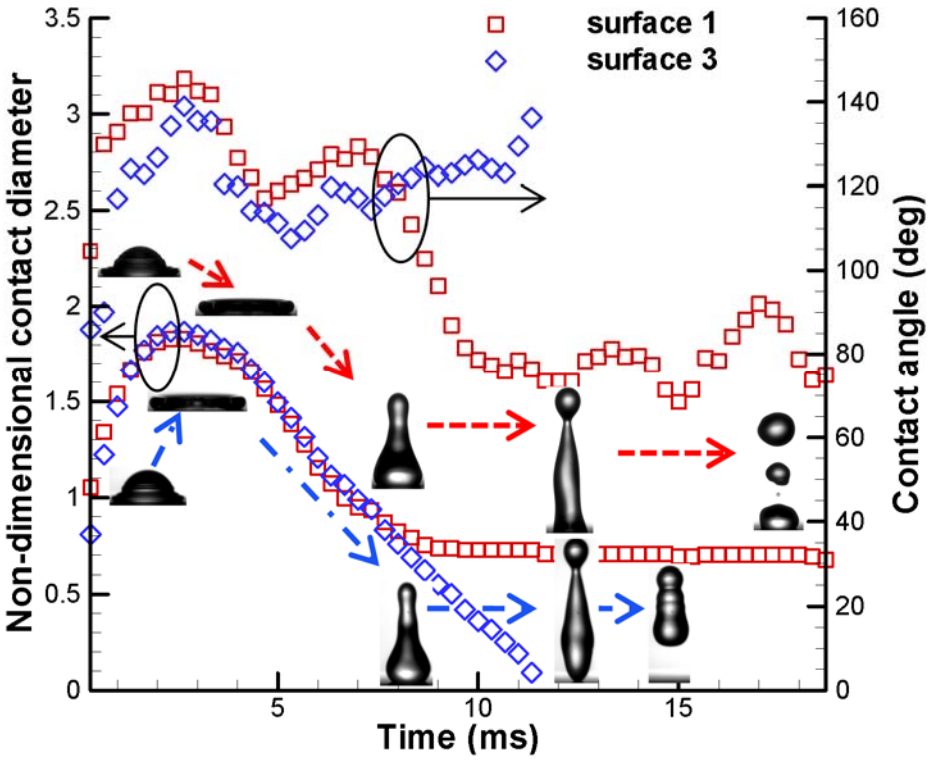

Figure 5.7. Instantaneous contact angle and non-dimensional contact diameter during non-wetting (surface 3) and wetting (surface 1) impact.

A strong influence of the surface type on droplet behavior upon impact is seen, however, during the retraction phase. On surface 3, the droplet retracts and detaches from the surface at t = 11.33 ms (Figure 5.7). Okumura *et al.* [135] proposed that the contact time (the total time of contact of the droplet with the surface) for a non-wetting impact is given by a characteristic time scale based on a balance between inertia and capillarity as $\tau = (2.6 \pm 0.1)\left(\rho R^3 / \gamma\right)^{1/2}$. This characteristic time scale for the droplet in the present work is 10.1 ms. The slightly larger contact time observed with surface 3 may be attributed to the hysteresis of the surface [71]. It can be seen from Figure 5.7 that the droplet behaves more or less alike on both surface 1 and surface 3 till t = 8 ms. The

wetted diameter of the droplet on surface 1 beyond t = 8 ms remains constant; thus the corresponding wetted diameter gives the length scale over which droplet transition occurred during impingement. Beyond this time, the droplet continues to retract with diminishing wetted diameter on surface 3, but is stuck indefinitely on surface 1. The inability of the droplet to recover from the Wenzel state induced due to impingement shows that there is extremely high resistance involved in detaching the droplet from the surface once it goes to its Wenzel state. This can be explained in terms of the energy expended in the transition process relative to the energy required for the subsequent reverse transition (from Wenzel to Cassie state). During droplet impingement, part of the energy of the droplet is expended in overcoming the energy barrier between the Cassie and the Wenzel states of the droplet, and the other part is utilized in spreading and subsequent retraction of the droplet interface.

The energy barrier for hollow-pillared hybrid surface may be determined from a modified form of Eq. (5.7),

$$E_C - E_W = -4\gamma_{LA}\cos\theta_0\left(a_0 + a_i\right)h\frac{\pi {R_C}^2}{p^2} = -4\pi {R_C}^2\gamma_{LA}\cos\theta_0\phi\frac{h}{\left(a_0 - a_i\right)}. \qquad (5.13)$$

Corresponding to a droplet impingement height of 50 mm, a portion of the droplet (of contact radius 0.72 mm) undergoes Wenzel transition on surface 1 as discussed earlier. The energy expended for this transition is 0.125 μJ, which is only a small fraction of the total energy of the droplet $(E_K = 2.21\,\mu J)$. The inability of the droplet to retract to the Cassie state once transition has occurred highlights the effect of non-conservative dissipation forces acting during reverse transition [35]. In contrast, the droplet has a non-wetting impact on surface 3, which means that the dissipative energy loss occurs only on

top of the pillars and hence, the entire droplet is able to bounce off the surface. The energy required for the Wenzel-to-Cassie reverse transition is much higher for the hollow-pillared hybrid surfaces than for the solid pillars, owing to the increased roughness (r_m) in the former.

Another characteristic distinguishing Cassie and Wenzel impact is the instantaneous contact angle of the droplet during the advancing and the receding phases (Figure 5.7). On surface 3, the droplet maintains a very high contact angle during its entire period of contact with the surface. On surface 1, however, the contact angle decreases beyond t = 8 ms, while the wetted diameter remains unchanged as the droplet remains partially in a Wenzel state. The oscillation observed in the contact angle beyond this time is a result of the attempt by the droplet to overcome the dissipative forces.

5.4.4 Pressure Balance

As discussed above, droplet impact on the hybrid surfaces fabricated for this work remains non-wetting for impingement velocities that are lower than the critical velocity. At the critical velocity, a part of the droplet goes into the Wenzel state and remains stuck to the surface. Once the impingement velocity exceeds the critical value and the effective wetting pressure exceeds the capillary pressure, the stability of the air gap in the superhydrophobic surface is compromised and drastic changes in the droplet characteristics are observed, primarily during the retraction phase of the droplet. Figure 5.8 illustrates the critical-velocity limit for surface 5. For the geometrical parameters of surface 5, the critical velocity is experimentally determined to be 1.37 m/s.

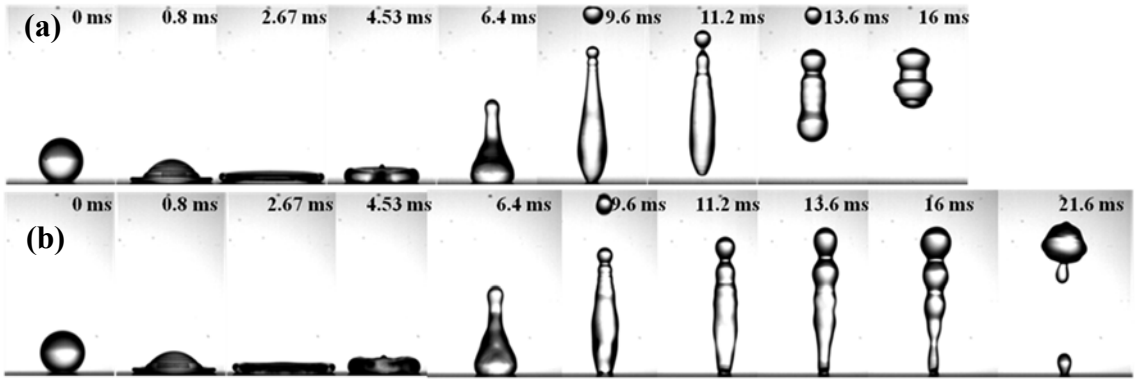

Figure 5.8. Instantaneous images during droplet impingement on surface 5 (P_C = 4768 N/m^2) corresponding to droplet velocities of (a) 1.34 m/s, and (b) 1.37 m/s. The second case represents the critical velocity for surface 5.

While expressions for P_C and P_D are available in the literature, the water hammer pressure P_{WH} for structured surfaces is less well quantified. The impact dynamics change in the presence of superhydrophobic surfaces. In the present work, careful experimental observation helps deduce the dependency of the water hammer pressure on different factors. The critical velocity corresponding to each surface is determined experimentally. The coefficient of water hammer pressure (in $P_{WH} = k\rho cV$) is then determined for each of the hollow hybrid surfaces based on the critical velocity for the Cassie-Wenzel transition,

$$k = \frac{P_C - P_D}{\rho c V}. \tag{5.14}$$

This approach to determining the coefficient k assumes that the theoretically calculated capillary pressure P_C applies. We assume that the effect of the step size of 5 mm used during impingement experiments is negligible in calculations of the coefficient. Table 5.4 lists the critical velocity and the value of the coefficient k in the definition of

P_{WH} corresponding to each of the surfaces. It is observed from these results that this coefficient is in fact not a constant, but is rather a function of the capillary pressure of the surface. The coefficient varies almost linearly with respect to capillary pressure as shown in Figure 5.9.

Table 5.4. Critical velocity and water hammer pressure coefficient for each hybrid surface.

Surface	**Critical height of impingement (mm)**	**Critical impingement velocity (m/s)**	**Coefficient of water hammer pressure**
1	50	0.99	0.1408×10^{-2}
2	50	0.99	0.1465×10^{-2}
3	100	1.40	0.2334×10^{-2}
4	100	1.40	0.1984×10^{-2}
5	95	1.37	0.1877×10^{-2}
6	90	1.33	0.1960×10^{-2}

Kwon *et al*. [140] showed that a Cassie-to-Wenzel transition can be induced due to water hammer pressure acting during pendant-drop deposition on a superhydrophobic surface. Wu *et al*. [141] carried out impingement experiments on superhydrophobic surfaces with different geometric parameters to demonstrate that the Cassie-Wenzel transition can lead to self-propelled movement of the droplet against the wettability gradient (due to the unbalanced interfacial forces). They reported the critical velocity of impingement for the different test surfaces (cylindrical pillars with fixed pillar diameter and height and varying pitch). We determine the capillary pressure based on the geometrical parameters of the surfaces used by Wu *et al.* [141] Substituting these values of critical impingement velocity and the capillary pressure in Eq. (5.14), we calculate the

coefficient of water hammer pressure (k). The data points evaluated are included in Figure 5.9 so as to place our experimental results in context with the literature. Even with a different surface geometry than that considered in the present work, these results from the literature follow a similar trend.

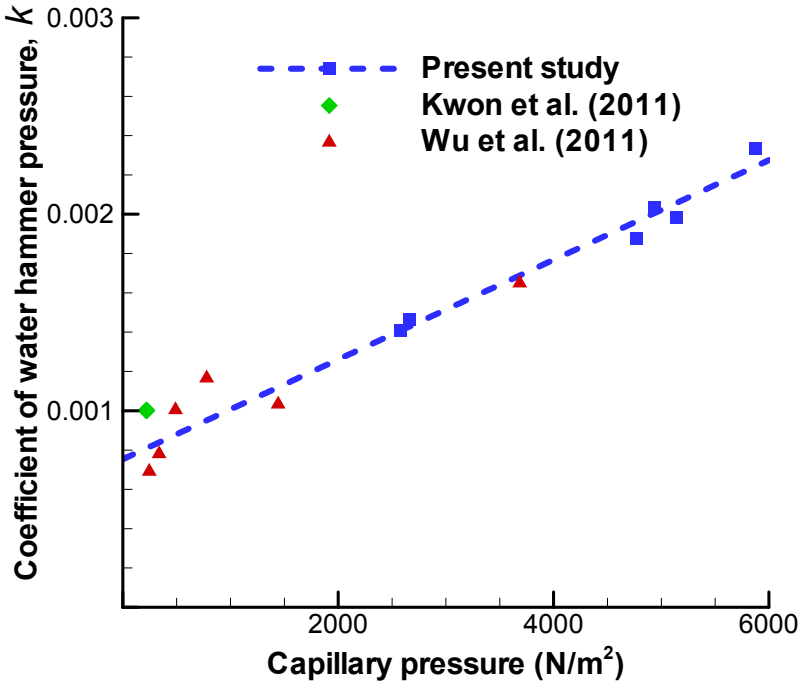

Figure 5.9. Plot showing the dependence between the coefficient of water hammer pressure and the capillary pressure.

This dependence of the water hammer pressure coefficient on the capillary pressure may be explained considering the morphology of the superhydrophobic surface, which is a combination of solid surfaces and air gaps. When a droplet impinges on a flat surface, its motion in the direction of fall is immediately arrested, resulting in a shock pressure. However, in the case of structured surfaces, the droplet experiences a heterogeneous impact. While the droplet comes to sudden stop on the solid parts of the surface, it is still

free to deform into the air gaps so that its overall deceleration is gradual. The shock developed is thus alleviated compared to a flat surface and this results in the much smaller observed coefficient of P_{WH} (ranging from k = 0.1408 x 10^{-2} to 0.2334 x 10^{-2} for the hybrid surfaces in this work compared to k = 0.2 on flat surface for moderate impingement velocities of approximately 8 m/s [80]).

In the limiting case ($V = V_{critical}$), the pressure balance may be written as

$$P_C - (k\rho cV) - \frac{1}{2}\rho V^2 = 0 . \tag{5.15}$$

Eq. (5.15) shows a quadratic dependence of the critical velocity on the capillary pressure which is also illustrated from the experimental results as well as those from Wu *et al.* [141] in Figure 5.10.

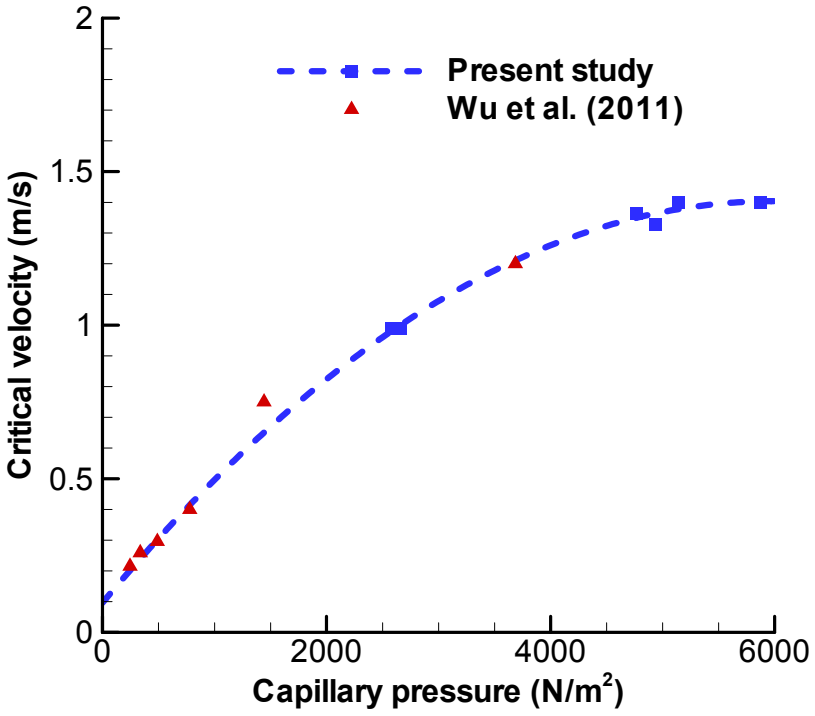

Figure 5.10. Plot showing the quadratic dependence of the critical velocity magnitude with respect to the capillary pressure.

This finding of the dependence of water hammer pressure on the surface morphology and capillary pressure could potentially contribute significantly to the design of superhydrophobic surfaces for practical applications. Experimental measurement of the impact forces during droplet impact on textured superhydrophobic surfaces would help in further understanding of the physics of impingement-induced wetting and droplet retraction.

5.5 Summary

Hollow-pillared hybrid surfaces consisting of both communicating and non-communicating air gaps are designed for enhancement of the anti-wetting pressure during droplet impact. The energy barrier of the superhydrophobic surfaces is represented in terms of the capillary pressure of the air gaps. The design could be further improved by decreasing the feature size, which would result in enhanced capillary pressure and air gaps of greater robustness. An additional pressure, namely the water hammer pressure, is demonstrated to play an important role during droplet impingement; however, the water hammer pressure coefficient is much smaller than for impingement on a rigid flat surface. Furthermore, the coefficient is predicted to be a function of the surface morphology, and hence of the capillary pressure; the critical velocity (which is the velocity of the droplet at which the droplet just goes to a Wenzel state upon impingement) is observed to exhibit a quadratic relationship with the capillary pressure.

Precise measurement of the impact forces is required to further validate the experimental observations and to obtain a precise value for the water hammer pressure coefficient. Results from this study offer a better understanding of impact dynamics that

can aid in the improved design of surfaces that can avoid the Wenzel transition under impinging droplets.

CHAPTER 6. DROPLET EVAPORATION DYNAMICS ON SURFACES WITH NEGLIGIBLE HYSTERESIS

In the current chapter, evaporation characteristics of sessile water droplets on smooth hydrophobic and structured superhydrophobic substrates is reported. On both surfaces, droplet evaporation is observed to occur in a predominant constant-contact-angle mode. The experimental results, with and without substrate heating, are compared with an isothermal vapor diffusion model for droplet evaporation from the literature. Good agreement is observed for the hydrophobic surface between the analytical expression and experimental results in terms of the total time for evaporation, transient volume, contact angle, and contact radius. The evaporation characteristics on superhydrophobic surface demonstrates significant deviation from the vapor diffusion-only model, with the difference being amplified as the substrate temperature is increased. This disparity is attributed primarily to the evaporative cooling at the droplet interface due to the high aspect ratio of the droplet and also the lower effective thermal conductivity of the substrate due to the presence of air gaps. A simple model considering thermal diffusion through the droplet is used to highlight the important role of evaporative cooling at the droplet interface in determining the droplet evaporation characteristics on superhydrophobic surfaces. The material presented in this chapter was published in *Langmuir* (**29**(34), pp. 10785-10795, 2013) [142] and *Phys. Rev. E* (84(4), p. 042402, 2014) [143].

6.1 Sample Preparation

Experiments are carried out on two test surfaces: a smooth hydrophobic surface and a textured superhydrophobic surface. The hydrophobic surface used in the experiments is a silicon wafer, spin coated with 0.02% solution of Teflon-AF 1600 (DuPont, Wilmington, DE) in FC-77 (3M, St. Paul, MN) to impart hydrophobicity. The fabrication procedure for the hierarchical surface used in the present work circumvents the conventional two-step process to create double-roughness structures. Silicon pillars constitute the larger roughness element and the second-tier roughness surface is obtained using a single deep reactive ion etching step (DRIE). The fabrication for this work was carried out in the Birck Nanotechnology Center at Purdue University.

Silicon prime wafers are spin-coated with positive photoresist AZ 9260 (Microchemicals) to form ~ 7 μm thickness of photoresist layer, and are lithographically patterned. The photoresist is cured at 90° C for 5 mins and acts as the etch mask for the deep reactive ion etch (Bosch) process. The Bosch process uses SF_6 for etching and C_4F_8 for passivation steps. During etching, the silicon is selectively etched to form the pillars. A higher passivation time and a lower O_2 gas flow during etching aids in retaining a fraction of the polymers formed during passivation. During the DRIE process, the partially cured photoresist is deformed and is retained at the top of the silicon pillars to form the desired second-tier roughness. Table 6.1 lists the process parameters used for fabrication of the hierarchical superhydrophobic surface. The periodicity (pitch) of the pillars is ~ 48 μm, while the width of the tops of the pillars is ~ 45 μm. The height of the pillars is 23 μm. The overall roughness (R_a) of the second-tier roughness element, measured using an optical profilometer (NewView 6300, Zygo), is 2.93 μm.

Table 6.1. DRIE process parameters.

Parameters	Value	
	Etching	**Passivation**
Switching time	8.5 sec	3 sec
Gas flow	450 sccm SF_6, 7 sccm O_2	200 sccm C_4F_8
RF coil power	2200 W	1500 W
RF bias power	30 W	20 W

The surface is then spin-coated with 0.02% solution of Teflon-AF 1600 in FC-77 to impart hydrophobicity. The thickness of the Teflon layer is approximately 50 nm; hence, the overall roughness of the primary roughness as well as the sub-micron roughness on top of the pillars is not affected by the Teflon coating. Figure 6.1 shows SEM images of the hierarchical superhydrophobic surface fabricated. The cratered second-tier roughness on the pillars renders the surface robustly superhydrophobic, enhances the CA of the droplet, and results in a CAH < 1 deg.

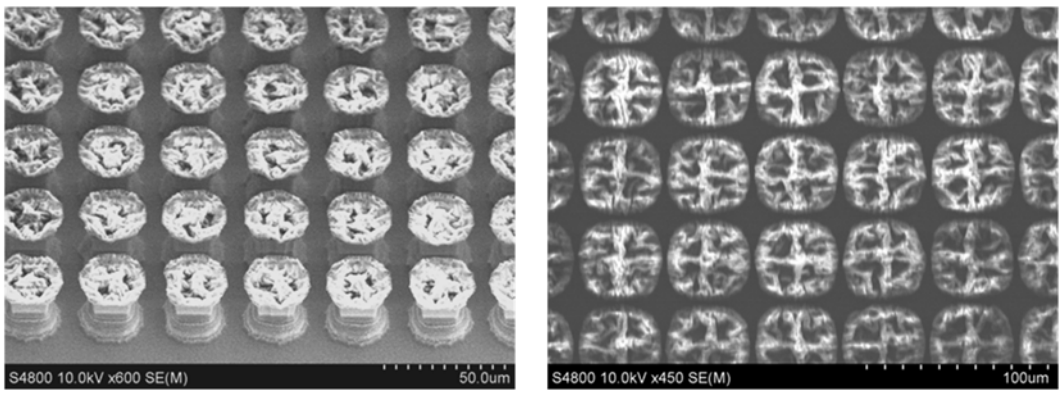

Figure 6.1. Scanning Electron Microscopy (SEM) images of the hierarchical superhydrophobic substrate used. The SEM image to the left shows the substrate tilted at 40 deg.

6.2 Experimental Setup

Deionized (DI) water droplets of volumes ranging from 1 to 8 $\mu L \pm 0.1\ \mu L$ are used in the experiments for droplet evaporation without substrate heating. In the case of droplet evaporation with substrate heating, deionized (DI) water droplets of initial volume $3\ \mu L \pm 0.1\ \mu L$ are used; this volume corresponds to initial radii of 0.95 mm on the hydrophobic surface and 0.90 mm on the superhydrophobic surface. For the range of droplet volume considered, the characteristic length of the droplet (its radius) lies below the capillary length scale $\left(\left(\gamma/\rho g\right)^{1/2}\right)$, which is equal to 2.7 mm for water. Thus gravity effects may be neglected and a spherical-cap assumption for the droplet holds [134].

The experimental setup is shown in Figure 6.2. The hot stage for the droplet evaporation experiments consists of a copper block that is electrically heated on its underside by a 10 W polyimide film heater (Minco); the sides of the block are insulated with fused ceramic foam. A PID controller (TOT-1200, Temp-o-Trol) is used to control the power input to the film heater based on the measured temperature close to the substrate. The test substrate is attached to the top of the copper block with a uniform layer of thermally conductive silicone paste (Omegatherm 201, Omega). The temperatures at four locations along the central axis of the copper block are continually measured during a test using a data acquisition system (34970A, Agilent Technologies). The temperature variation across the thickness of the copper block remained below the uncertainty of the thermocouple measurements. Therefore, the heater block can be treated as being isothermal, and the temperature nearest the sample substrate is quoted as the sample temperature for all the experiments. For the test cases with unheated

substrates, the ambient temperature and humidity are maintained at 20.5 ± 0.5°C and 29 ± 1%, respectively. Evaporation experiments are carried out at three different substrate temperatures: 40 ± 0.5°C, 50 ± 0.5°C and 60 ± 0.5°C. During the experiments of droplet evaporation on heated substrates, the ambient temperature and relative humidity are maintained at 21 ± 0.5°C and 36 ± 2%, respectively.

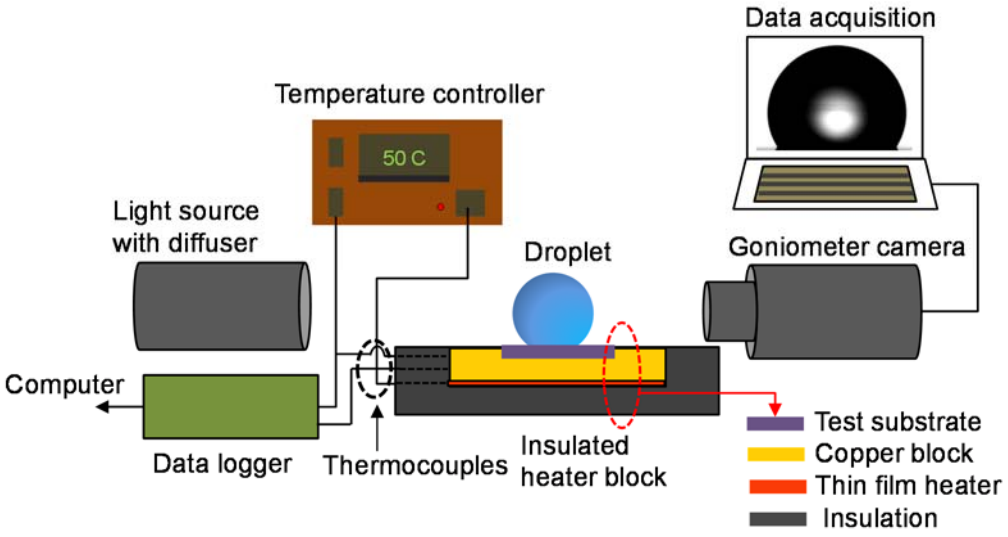

Figure 6.2. Schematic diagram of the experimental setup

For each test, a droplet is dispensed using a carefully calibrated microsyringe on to the test surface, and visualized using the goniometer imaging system till it evaporates completely. The diffusivity of water vapor in air, and saturated vapor concentration are sensitive to temperature. Therefore, precise control of experimental temperature and humidity conditions is essential for accurate determination of the droplet transient characteristics during evaporation. The actual temperature and humidity are recorded during each test and used in the analysis of the droplet evaporation characteristics so as to account for any minor fluctuations in values (the diffusion coefficient D is 25.41×10^{-6}

m^2/s, and the saturated vapor concentration c_s is 0.0175 kg/m^3 at a temperature of 20.5°C [144]). The static contact angle of the droplet on the surface is measured using a goniometer (Model 290, Ramehart). A cold light source used for backlighting ensures improved contrast without affecting the droplet evaporation rate. The images are recorded in intervals of 10 to 30 s and analyzed using the goniometer software. A circular curvefit to the droplet image gives the contact angle (θ), contact radius (R_c) and height (h) of the droplet (Figure 6.3a and Figure 6.3b). The droplet height and contact radius are also calculated and verified using an in-house MATLAB [119] code, and the contact angle using the relation $\theta = 2\tan^{-1}\left(\frac{h}{R_c}\right)$. Figure 6.3a and Figure 6.3b show the initial parameters of a droplet placed on the smooth and structured surfaces, respectively. The initial contact angle of the droplet on the smooth hydrophobic surface is ~ 120° and that on superhydrophobic surface is ~ 160°. The corresponding values of contact angle hysteresis are ~ 10 deg and ~ 1 deg, respectively.

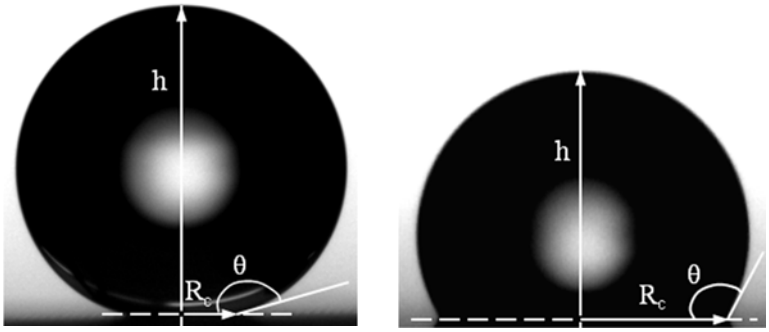

(a) (b)

Figure 6.3. Droplet placed on the (a) hierarchical superhydrophobic surface, and (b) smooth hydrophobic surface (Teflon-coated Si).

6.3 Theoretical Analysis

Without any external heat applied to the substrate, evaporation of the droplet is driven by the concentration gradient of water vapor between the droplet surface and the ambient. Diffusion of vapor into the atmosphere is the rate-limiting step, and the time scale for diffusion is on the order of $\frac{R_i^2}{D} \approx 0.04\,\mathrm{s}$, where D is the coefficient of vapor diffusion and R_i is the length scale of the droplet (initial radius of the droplet, which is on the order of mm) [13]. The diffusion time scale for a microliter-sized droplet is much smaller than the total evaporation time (typically a few hundred seconds). In the case of heated substrates the total time for complete evaporation of a droplet is significantly reduced when the surface is heated. However, even at a surface temperature of 60 °C, for a droplet of volume 3 μL, the ratio of diffusion time (t_D) to evaporation time (t_F) is $t_D/t_F \sim 0.0002$ (using experimental t_F). Therefore, the vapor concentration around the droplet may be assumed to be quasi-steady for unheated substrates as well as heated substrates for the range of temperatures considered in the study. A droplet suspended in air evaporates with its size constantly diminishing at a rate that is proportional to the droplet radius [82]. In case of a sessile droplet, the rate of evaporation is affected by the presence of the substrate and depends on the contact radius of the droplet as well its contact angle [82].

Several models have been proposed to describe the evaporation process of a droplet [99]. However the experiment-specific nature of the assumptions and simplifications inherent in the models prevent their application to other experimental studies [16, 83, 84]. Popov [13] proposed an analytical diffusion model for quasi-steady natural evaporation

of a droplet based on the solution to the Laplace equation describing the concentration field at the droplet surface in a toroidal coordinate system. The model accounts for the non-uniform vapor concentration field around the droplet. The evaporation flux $J(r)$ on the surface of a droplet in a toroidal coordinate system according to the diffusion-only model for evaporation is given as [13],

$$J(r) = \frac{D(c_s - c_\infty)}{R_c} j(\theta)$$

$$j(\theta) = \left[\frac{1}{2} \sin\theta + \sqrt{2} (\cosh\alpha + \cos\theta)^{3/2} \times \int_0^\infty \frac{\cosh\theta\tau}{\cosh\pi\tau} \tan\left[(\pi - \theta)\tau\right] P_{-1/2+i\tau}(\cosh\alpha)\tau d\tau \right], \quad (6.1)$$

where D is the coefficient of vapor diffusion, c_s the saturated vapor concentration on the droplet surface, c_∞ the concentration of water vapor at infinity, R_c the contact radius of the droplet, θ the contact angle of the droplet, and r the radial coordinate at the baseline of the droplet such that $r = R_c$ at the contact line. α and β are toroidal coordinates and are related to the height (h), contact radius R_c and contact angle θ of the droplet as

$$\cosh\alpha = \frac{\sin\theta}{\left(h/R_c\right)} - \cos\theta . \quad (6.2)$$

The expression for droplet evaporation rate, obtained by integration of evaporation flux over the droplet surface area, is based on the contact angle θ and contact radius R_c and is valid over the entire range of contact angles. It is noted that the contact-angle dependence of the evaporation rate as obtained by Picknett and Bexon [82] converges to Popov's solution [13], although the final expressions are in different forms: The dependence of the evaporation rate on CA given by Picknett and Bexon is in the form of

an approximate series solution, while Popov provided a closed-form expression. For any contact angle, the rate of mass loss as given by Popov is

$$\begin{aligned} &\frac{dM}{dt} = \rho_L \frac{dV}{dt} = -\pi R_C D(c_s - c_\infty) f(\theta); \\ &f(\theta) = \frac{\sin\theta}{1+\cos\theta} + 4\int_0^\infty \frac{1+\cosh 2\theta\tau}{\sinh 2\pi\tau} \tanh\left[(\pi-\theta)\tau\right] d\tau \end{aligned}, \tag{6.3}$$

where M is the droplet mass, ρ_L the liquid density, V the droplet volume, R_c the contact radius, D the coefficient of vapor diffusion, c_s the saturated vapor concentration on the droplet surface, c_∞ the concentration of water vapor at infinity, and $f(\theta)$ the functional variation of CA evaluated using a numerical integration scheme in MATLAB [119]. Using a spherical-cap assumption, the mass of the droplet may be written as

$$M = \frac{\pi\rho_L R_c^{\,3}}{3g(\theta)};\ g(\theta) = \frac{\sin^3\theta}{(1-\cos\theta)^2(2+\cos\theta)} \tag{6.4}$$

$$R_c = \left(\frac{3}{\pi} V\, g(\theta)\right)^{1/3}. \tag{6.5}$$

Eq. (6.3) may now be written as

$$\rho_L \frac{dV}{dt} = -\pi\left(\frac{3}{\pi} V\, g(\theta)\right)^{1/3} D(c_s - c_\infty) f(\theta). \tag{6.6}$$

On surfaces with significant CAH, the contact line remains pinned; the contact angle and the droplet height change to account for the mass loss of the droplet due to evaporation. When evaporation occurs in constant contact radius (CCR) mode (R_c = constant), the change in contact angle may be derived from Eqs. (6.1) and (6.2) as

$$\frac{d\theta}{dt} = -\frac{D(c_s - c_\infty)}{\rho_L R_c^{\,2}}(1+\cos\theta)^2 f(\theta). \tag{6.7}$$

The suitability of Eqs. (6.4) and (6.5) for determining the instantaneous droplet volume and contact angle in CCR mode on surface with high CA (~ 150 deg) has been demonstrated by Gelderblom *et al.* [98]. On most surfaces, a combination of both CCA and CCR mode is observed. The droplet evaporation on an ideal smooth surface with no irregularities is expected to occur at a constant contact angle. Under this condition, the droplet evaporation characteristics should be similar those of a drop suspended in air, except for the suppression of evaporation due to the contact with the solid surface. For droplet evaporation in constant contact angle mode (θ constant), the transient volume (V) is obtained by integration of Eq. (6.6) and is given by

$$V^{2/3} = V_i^{2/3} - \frac{2D(c_s - c_\infty)}{3\rho_L}\left(\frac{3}{\pi}\right)^{1/3}\left(g(\theta)\right)^{1/3} f(\theta)t\,. \tag{6.8}$$

in which V_i is the initial volume of the droplet. By rearranging the terms in Eq. (6.8) and using Eq. (6.5), the square of the wetted radius of the droplet can be represented as a linear function of time for a constant contact angle mode:

$$R_c^{\,2} = R_{ci}^{\,2} - \frac{2D(c_s - c_\infty)}{\rho_L} g(\theta) f(\theta) t\,. \tag{6.9}$$

Time taken for complete evaporation $\left(t_{tot}\right)$ may be obtained from the integration of Eq. (6.4), and for constant contact angle evaporation is given by

$$t_{tot} = \frac{\rho_L}{2D(c_s - c_\infty)}\left(\frac{3V_i}{\pi}\right)^{2/3} \frac{1}{\left(g(\theta)\right)^{1/3} f(\theta)} = k\,V_i^{2/3} \tag{6.10}$$

$$\text{in which } k = \frac{\rho_L}{2D(c_s - c_\infty)}\left(\frac{3}{\pi}\right)^{2/3} \frac{1}{\left(g(\theta)\right)^{1/3} f(\theta)}\,. \tag{6.11}$$

It is clear that k is constant for a fixed contact angle (θ). The total time for droplet evaporation in CCA mode is thus a linear function of the initial volume of the droplet.

Girard *et al*. [145] extended the vapor-diffusion model [13] to describe evaporation on a heated surface by allowing the droplet and substrate to be at an elevated temperature with respect to the ambient (but the droplet still was at the same temperature as the substrate), and determined the evaporation rate of droplets on a hydrophilic heated substrate as

$$J(r) = \frac{D\left(c_s\left(T_s\right) - Hc_s\left(T_a\right)\right)}{R_c} j\left(\theta\right). \tag{6.12}$$

in which T_s is the substrate temperature, T_a the ambient temperature. For droplet evaporation on a heated substrate, Equations 6.3 – 6.11 hold true with $c_s = c_s(T_s)$; $c_\infty = c_s(T_\infty)$ under the assumption that droplet evaporation is driven by vapor-diffusion.

6.4 Results and Discussion

6.4.1 Droplet Evaporation Characteristics on Unheated Substrates

6.4.1.1 Droplet Evaporation on a Smooth Hydrophobic Substrate

Droplet volumes of 1 to 6 μL are considered for study of evaporation characteristics on the smooth hydrophobic surface. The initial contact angle of the droplet is 118 ± 2 deg. Droplet evaporation characteristics are analyzed in terms of transient droplet volume, contact radius, and contact angle. Figure 6.4a shows the time evolution of the contact angle, and non-dimensional wetted radius of the droplet (with respect to non-dimensional time, $\tau = t/t_{tot}$). Droplet evaporation on the smooth hydrophobic surface occurred in two distinct phases. The initial phase of evaporation proceeds with contact

radius remaining nearly constant until the contact angle of the droplet reaches the receding contact angle (θ_{rec}) at $t = t_{rec}$. The receding contact angle of the droplet is 108 to 110 deg for all cases irrespective of the initial volume of the droplet considered (Figure 6.4a). In the second phase, the contact radius shrinks with the contact angle reducing at a much slower rate. Towards the end of the evaporation process, the contact angle and contact radius decrease simultaneously over a brief period of time. This mixed evaporation regime exists for a small fraction (~ 10%) of the total evaporation time and is neglected for the purpose of the current analysis. The droplet evaporation can thus be represented as a succession of the CCR and CCA modes.

The droplet evaporates in a constant contact radius mode from $t = 0$ to $t = t_{rec}$. The differential equation for CA given in Eq. (6.7) is integrated to determine the instantaneous droplet contact angle,

$$\int_0^{t_{rec}} dt = -\int_{\theta_i}^{\theta_{rec}} \frac{\rho R_c^{\,2}}{D\Delta c\left(1+\cos\theta\right)^2 f\left(\theta\right)} d\theta \tag{6.13}$$

$$\begin{aligned} \theta^n &= \theta^{n-1} + \frac{d\theta}{dt}\Delta t \\ &= \theta^{n-1} - \frac{D\left(c_s - c_\infty\right)}{\rho_L R_c^{\,2}}\left(1+\cos\theta\right)^2 f\left(\theta\right)\Delta t \end{aligned} . \tag{6.14}$$

Using the initial contact angle of the droplet (θ_i = 120 deg) and a fixed time step (Δt = 5 s), we use an explicit time-marching scheme to determine the transient contact angle (θ^n) of the droplet between $t = 0$ and $t = t_{rec}$. The value of CA at the previous time instant is denoted by θ^{n-1}. The total time for evaporation of a droplet solely in the CCR mode may be determined using Eq. (6.14) using $\theta^n = \theta_{rec} = 0\,\text{deg}$. The dashed lines in

Figure 6.4a and Figure 6.4b represent the instantaneous CA of the droplet until $t = t_{rec}$ predicted using Eq.(6.14). The predicted CA shows reasonable agreement with the experimental transient CA of the droplet. Table 6.2 shows that there is a reasonable match between the predicted value of the time at which the droplet contact line starts receding and the experimental results.

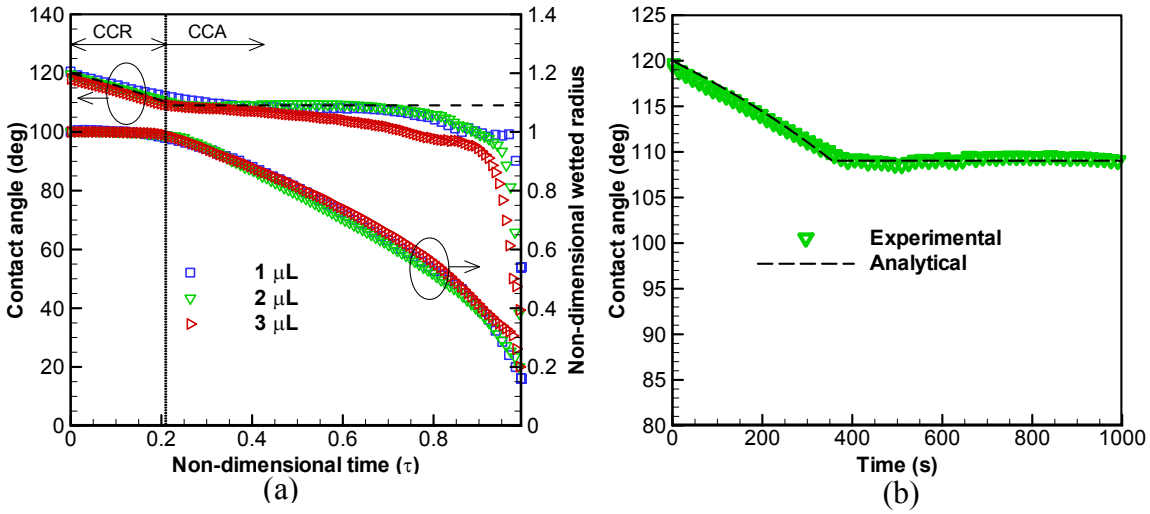

Figure 6.4. (a) Variation of contact angle and nondimensional wetted radius of evaporating droplets of different volumes as a function of the nondimensional time, and (b) comparison between experimental CA and transient CA predicted using Eq. (6.14) for droplet volume = 2 μL.

Table 6.2. Time when the contact line starts receding.

Volume (μL)	**t_{rec} Analytical (sec)**	**t_{rec} Experimental (sec)**	**Deviation (%)**
1	175	195	11.43
2	355	390	9.86
3	380	405	6.58
4	430	480	11.63

The second phase of droplet evaporation on the smooth hydrophobic surface occurs in a CCA mode. The contact angle remains almost constant at θ_{rec} (~ 110 deg), and the droplet radius and height change in response to the mass loss by evaporation. The instantaneous droplet contact radius can be predicted using Eq.(6.9). To account for the droplet contact line pinning till $t = t_{rec}$ in the first phase of the evaporation process, Eq. (6.9) may be written as

$$R_c^{\,2} = R_{ci}^{\,2} - \frac{2D(c_s - c_\infty)}{\rho_L} g(\theta_{rec}) f(\theta_{rec})(t - t_{rec}). \tag{6.15}$$

Figure 6.5 shows the variation of the square of the contact radius for different droplet volumes on the smooth hydrophobic surface. The square of the contact radius varies linearly with time beyond $t = t_{rec}$. The dashed lines represent the predictions from Eq.(6.15), which show good quantitative and qualitative agreement with the experimental values.

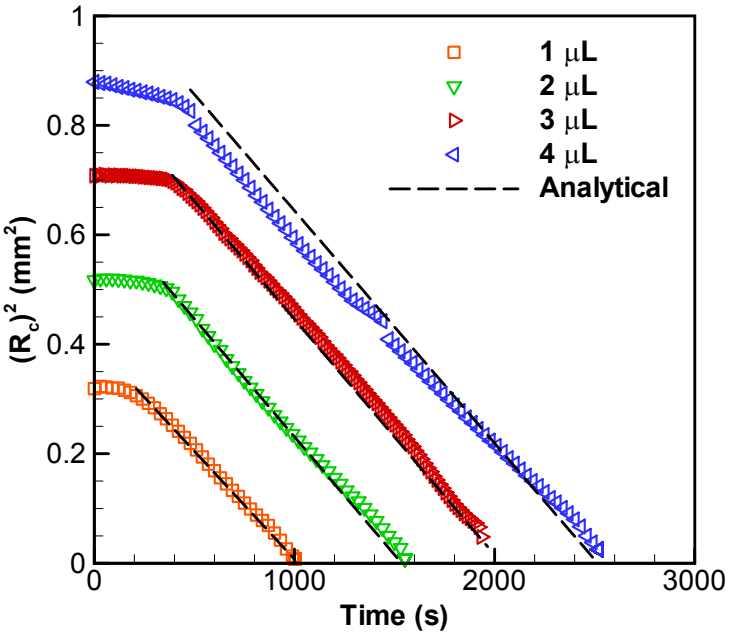

Figure 6.5. Transient variation of droplet volume on the smooth hydrophobic surface.

Next, the total time that the droplet takes to evaporate on the smooth hydrophobic surface is compared to the analytical solution of Popov [13]. Two cases are considered: first, we determine the total time for evaporation assuming droplet evaporation only in the CCA mode $\left(\theta=\theta_{rec}\right)$, and in the second case, the total time is evaluated with the CCR mode assumption ($R = R_i$). The time required for CA to change from $\theta = \theta_i$ to $\theta = 0$ (Eq. (6.14)) gives the total time of evaporation in the CCR mode. Table 6.3 lists the time taken for the total evaporation of the droplet corresponding to both cases. It is evident that the evaporation time is well-predicted using the relation for the CCA mode of evaporation (Eq. (6.10)).

A comparison of the experimentally determined time for complete evaporation with the analytical prediction assuming the CCA mode (Eq(6.10)) and CCR mode (Eq.(6.13)) is shown in Figure 6.6. A linear dependence is observed between the total evaporation time and the droplet volume raised to a two-third power. With the experimental parameters, D = 25.41 x 10^{-6} m^2/s, saturated vapor concentration c_s = 0.0175 kg/m^3, humidity (H) = 0.29, and θ = 110 deg, the proportionality constant k in Eq. (6.11) is determined to be 947.

Table 6.3. Total time for evaporation on the smooth hydrophobic surface.

Volume (μL)	**Time taken in CCA mode (s) Case 1**	**Time taken in CCR mode (s) Case 2**	**Time taken for complete evaporation (s) Experimental**	**Deviation (%)**
1	954	870	1009	5.45
2	1521	1350	1562	2.62
3	1993	1820	1971	-1.12
4	2450	2240	2543	3.80

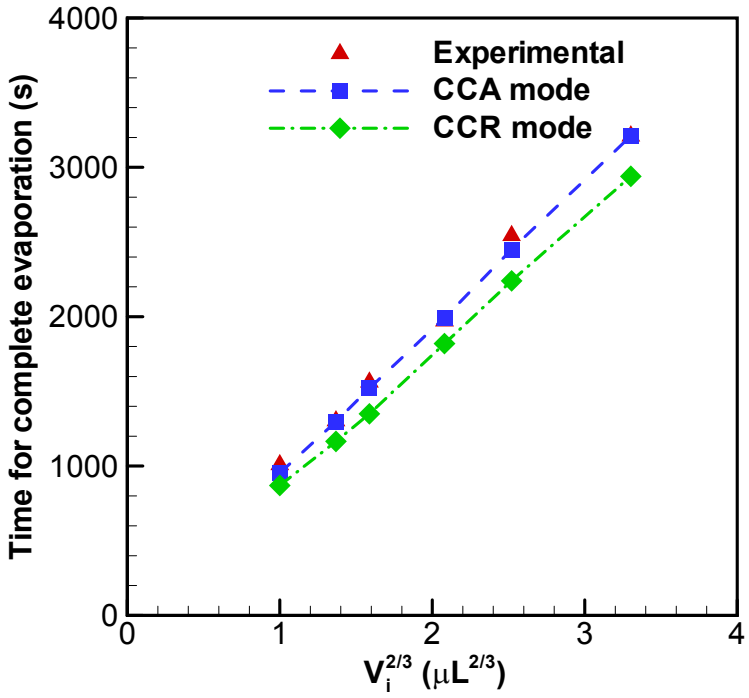

Figure 6.6. Total time for evaporation of droplets of different volume on the smooth hydrophobic surface. The dashed lines represent the time required for complete evaporation of droplets in the CCA mode (Eq. (6.8)) and in the CCR mode (Eq. (6.10)).

Figure 6.7 shows the time evolution of the volume of the evaporating droplet corresponding to the four different initial droplet volumes considered. The symbols

represent the experimental data and the dashed lines in the figure represent the transient droplet volume predicted using the expression for fixed contact angle (θ_{rec} = 110 ± 1 deg), *i.e.*, Eq. (6.6). Although evaporation on a smooth hydrophobic surface proceeds in the CCR mode followed by the CCA mode, a constant contact angle model is observed to predict the total time of evaporation as well as the droplet volume evolution with good accuracy. The change of volume with respect to time is non-linear, consistent with the evaporation characteristics reported by Nguyen [96]. This non-linear trend is seen throughout the evaporation time span, irrespective of whether evaporation is occurring in CCR or CCA mode.

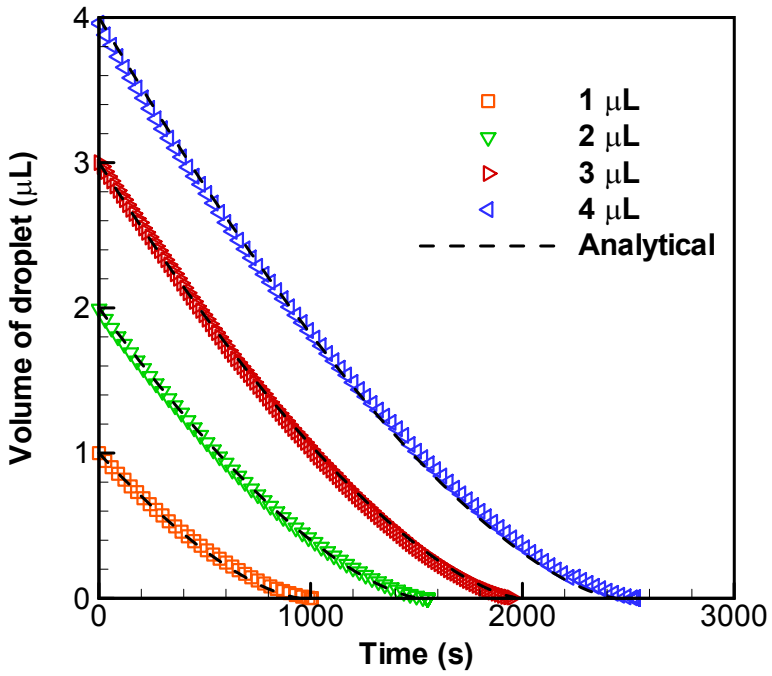

Figure 6.7. Temporal evolution of droplet volume during evaporation on the smooth hydrophobic surface for different initial droplet volumes (1 μL – 4 μL).

6.4.1.2 Droplet Evaporation on a Hierarchical Superhydrophobic Substrate

As discussed earlier, the hierarchical surface considered features two-tier roughness. The contact angle hysteresis (CAH) of the surface is measured using roll-off experiments [71] to be extremely low (< 1 deg). Negligible CAH implies that the receding CA is almost equal to the initial CA, $\theta_{rec} \sim \theta_i$. Hence, the droplet contact line starts receding immediately as the droplet placed on the substrate begins to evaporate. The droplet evaporation, therefore, occurs predominantly in the CCA mode. The instantaneous droplet images of a 3 μL droplet evaporating on the smooth hydrophobic surface and the superhydrophobic surface are illustrated in Figure 6.8a and Figure 6.8b. Figure 6.9 shows the contact angle and non-dimensional contact radius with respect to non-dimensional time (normalized with respect to the total observed time for evaporation). The inset shows the time-varying outline for a droplet of initial volume 2 μL as it evaporates. The droplet wetted radius shrinks with time, and a CCR phase is almost absent in case of this superhydrophobic surface. Towards the tail end of evaporation, the contact angle and contact radius shrink simultaneously for a very brief period. As with evaporation on the smooth hydrophobic surface, this mixed mode where both CA and CR decrease exists for a very short duration (~ 3% of the total evaporation time) and may be ignored for analysis.

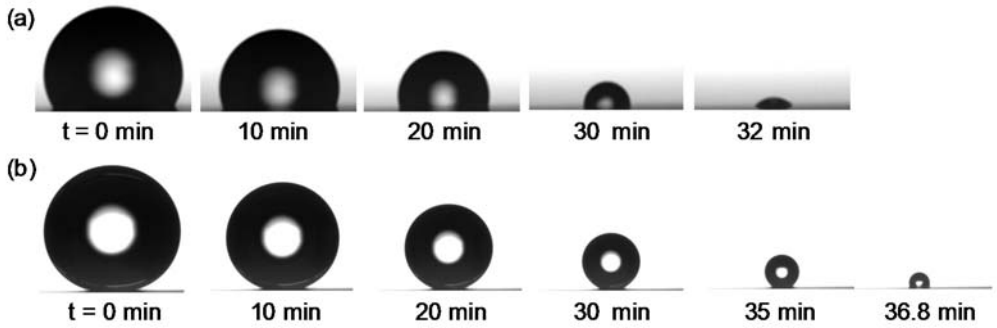

Figure 6.8. Instantaneous images of a sessile droplet (V_i = 3 μL) evaporating on (*a*) the smooth hydrophobic surface, and (*b*) the hierarchical superhydrophobic surface.

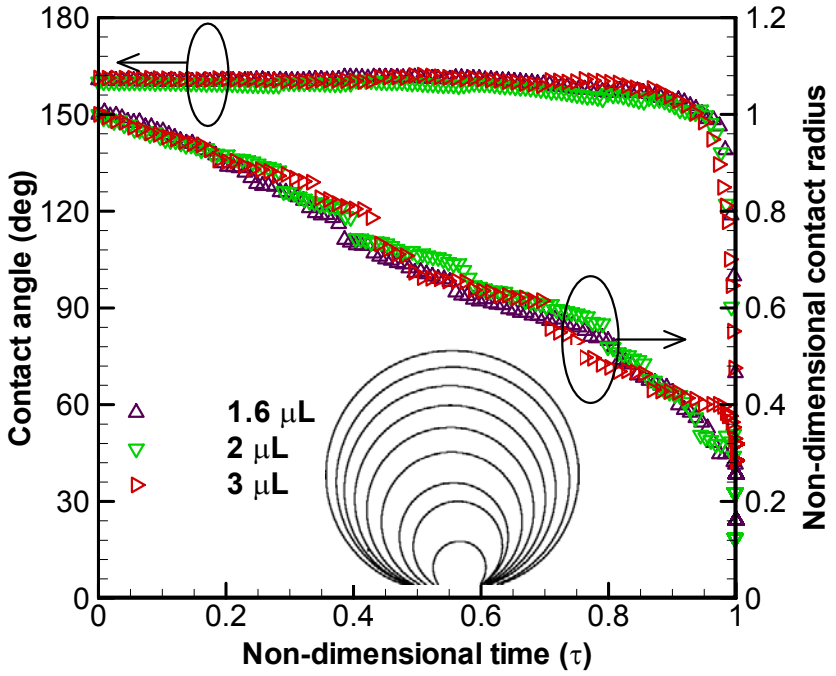

Figure 6.9. Contact angle and non-dimensional contact radius of droplets on the hierarchical superhydrophobic substrate. The inset shows the time-varying outlines for a droplet of initial volume 2 μL as it evaporates.

The total time taken for complete evaporation of droplets of different initial volumes on the hierarchical surface is determined experimentally and shown in Figure 6.10. The total time period varies linearly as $V_i^{2/3}$. With the experimental parameters D = 25.41 x

10^{-6} m^2/s, c_s = 0.0175 kg/m^3, humidity (H) = 0.29, and θ = 160 deg, the proportionality constant k in Eq. (6.8) is determined to be 890. For a constant contact angle mode, the total time of evaporation is given by Eq. (6.8). Figure 6.10.shows a comparison between the duration for complete evaporation of the droplet on the hierarchical surface with the predicted time from Eq. (6.8). The error bars represent the standard deviation of the measurements averaged over four experimental runs. Unlike in the case of the smooth hydrophobic surface where the experimental results agreed well with predictions for all initial droplet volumes (Figure 6.6), a consistent difference is seen between the two for the superhydrophobic surface (Figure 6.10). The actual times for evaporation are 1.25 to 1.33 times the predicted times. The analytical model overestimates the rate of evaporation by ~ 20 %. The increase in actual time for evaporation may be attributed to the reduced ease of vapor diffusion due to geometric vapor confinement under the footprint of the droplet due to the presence of air gaps, which is not taken into account in the model. Although the analytical expression using the isothermal diffusion model indicates that the difference between the time taken by a droplet to evaporate in the CCA and CCR modes becomes negligible beyond a CA ~ 150 deg [146], the experimental results from the present study indicate otherwise. Similar evidence of suppression of evaporation near the contact line in the CCA mode was offered by Kulinich and Farzaneh [17], with experimental measurements for evaporation on two surfaces with the same initial CA and varying CAH. The droplet in the CCA mode was reported to take significantly longer to evaporate than that in the CCR mode. The reduction in the rate of evaporation on the superhydrophobic surface with the CCA mode may also be attributed

to the reduced effective thermal conductivity of the substrate as will be discussed later in this section.

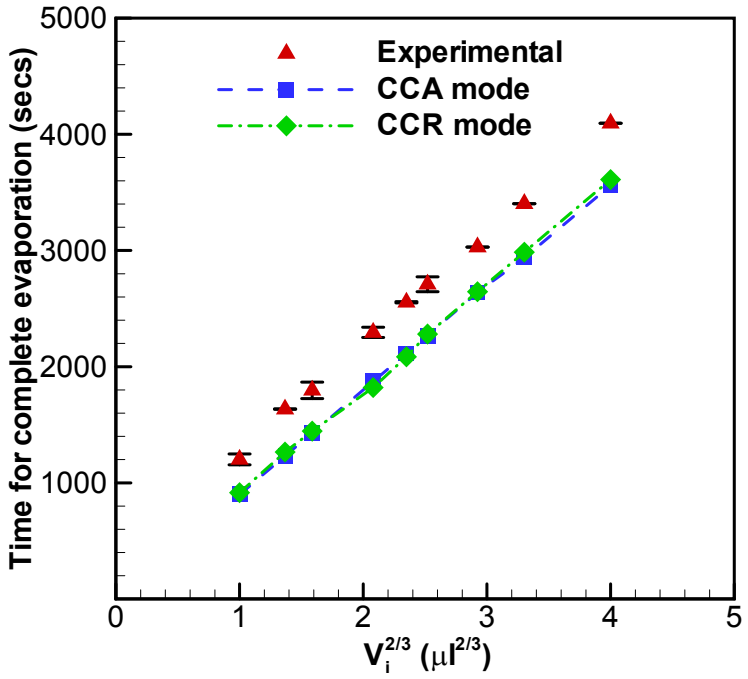

Figure 6.10. Total time for complete evaporation of droplets of different initial volumes (V_i) on the hierarchical superhydrophobic surface.

The isothermal diffusion model overpredicts the rate of evaporation of a droplet placed on a superhydrophobic surface with negligible CAH. In order to account for the suppression of evaporation, a correction factor of 0.8 is introduced to Eq. (6.8) to predict the instantaneous volume of the droplet. The instantaneous volume of the droplet may therefore be estimated as

$$V^{2/3} = V_i^{2/3} - 0.8\frac{2D(c_s - c_\infty)}{3\rho_L}\left(\frac{3}{\pi}\right)^{1/3}\left(g(\theta)\right)^{1/3} f(\theta)t\,. \tag{6.16}$$

Figure 6.11 shows the temporal variation of droplet volume on the hierarchical superhydrophobic surface for different initial droplet volumes. The droplet volume varies non-linearly with time. Interestingly this behavior of non-linear reduction in volume also matches the droplet evaporation on surface with very high initial contact angle *and* high contact angle hysteresis leading to a pinned mode of evaporation [98]. The dashed lines show the predicted transient droplet volume of the droplets with different initial volumes using Eq. (6.16), which includes the correction proposed in this work for suppression of evaporation for high contact angle droplet evaporation.

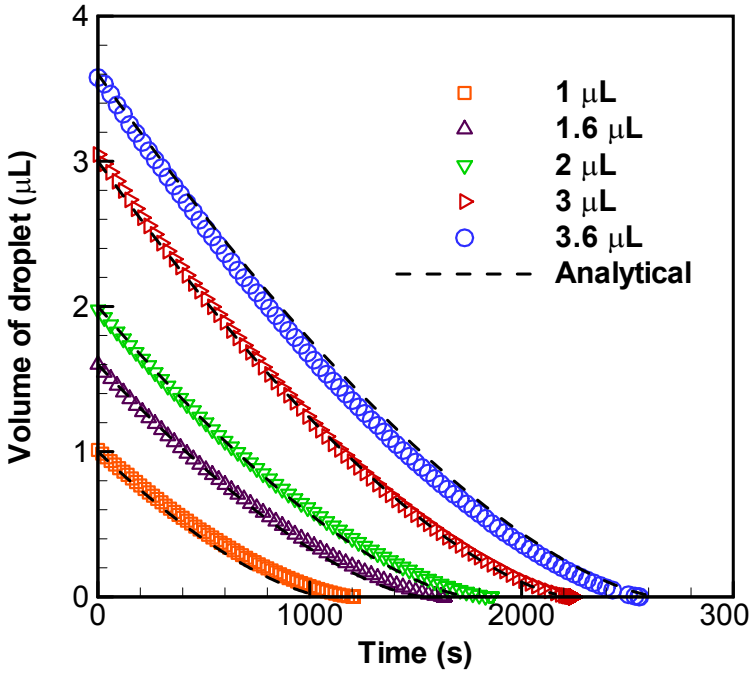

Figure 6.11. Transient evolution of droplet volume during evaporation of droplets of different initial volumes on the hierarchical superhydrophobic surface.

6.4.2 Generalized Relation for Droplet Volume Variation during Evaporation on Unheated Hydrophobic and Superhydrophobic Surface

As seen from the previous sections, experiments on hydrophobic and hierarchical superhydrophobic surfaces with respective CA of approximately 120 deg and 160 deg indicate a non-linear variation of volume with time when the CA > 90 deg. The linear relationship between the transient volume raised to $2/3^{rd}$ power and time holds good for superhydrophobic surface where the contact angle remains fixed throughout the process of evaporation, as well as for hydrophobic surface where a combination of CCR and CCA modes exists (Figure 6.5 and Figure 6.10). Also the experimental data of Gelderblom *et al*. [98] suggest a non-linear dependency of the droplet volume on time, even when the droplet evaporates predominantly in a constant contact radius mode. These experiments confirm the current observation that the volume of the droplet changes non-linearly with time when CA > 90 deg. One reason for such non-linear behavior may be the extreme sensitivity of $f(\theta)$ in Eq. (6.3) on θ when CA > 90 deg (the dependence between $f(\theta)$ and θ for the entire range of CA is shown in Figure 6.12.

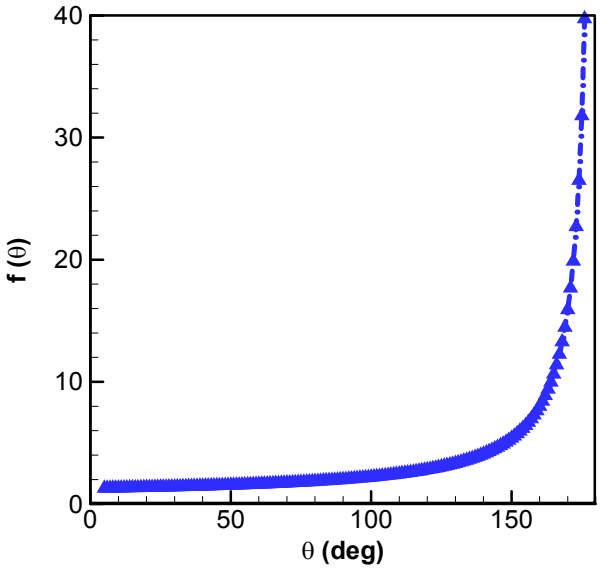

Figure 6.12. Variation of f(θ) with respect to contact angle of the droplet.

We non-dimensionalize the droplet transient volume (V) during evaporation with respect to the initial volume (V_i) and time (t) using the total time for evaporation of the droplet (t_{tot}) as

$$V^* = \left(\frac{V}{V_i}\right), \qquad t^* = \left(\frac{t}{t_{tot}}\right). \tag{6.17}$$

Using Eq. (6.8) and Eq. (6.10), the non-dimensional volume of the droplet may be written simply as

$$\left(\frac{V}{V_i}\right)^{2/3} = 1 - t^*. \tag{6.18}$$

Figure 6.13a and Figure 6.13b show the variation of the normalized $V^{2/3}$ versus non-dimensional time on smooth hydrophobic and hierarchical superhydrophobic surfaces, respectively. It is noted that even for the hydrophobic surface on which the droplet evaporation follows a typical three-stage process (CCR mode followed by CCA and

mixed modes), the above expression shows good agreement with experimental results. Further, we extract experimental data for droplet evaporation on a superhydrophobic surface with a pinned contact line from Gelderblom *et al.* [98] and plot along the same coordinates in c. There is reasonable agreement between the analytical and experimental values till $t^* \sim 0.5$, beyond which some deviation is observed. The deviation as t^* approaches 1 may be explained in terms of the contact angle of the droplet being less than 90 deg towards the end of the evaporation [98]. Eq. (6.18) therefore provides a generalized relationship between the instantaneous droplet volume and the time scale, irrespective of the mode of droplet evaporation when the contact angle of the droplet $\theta >$ 90 deg.

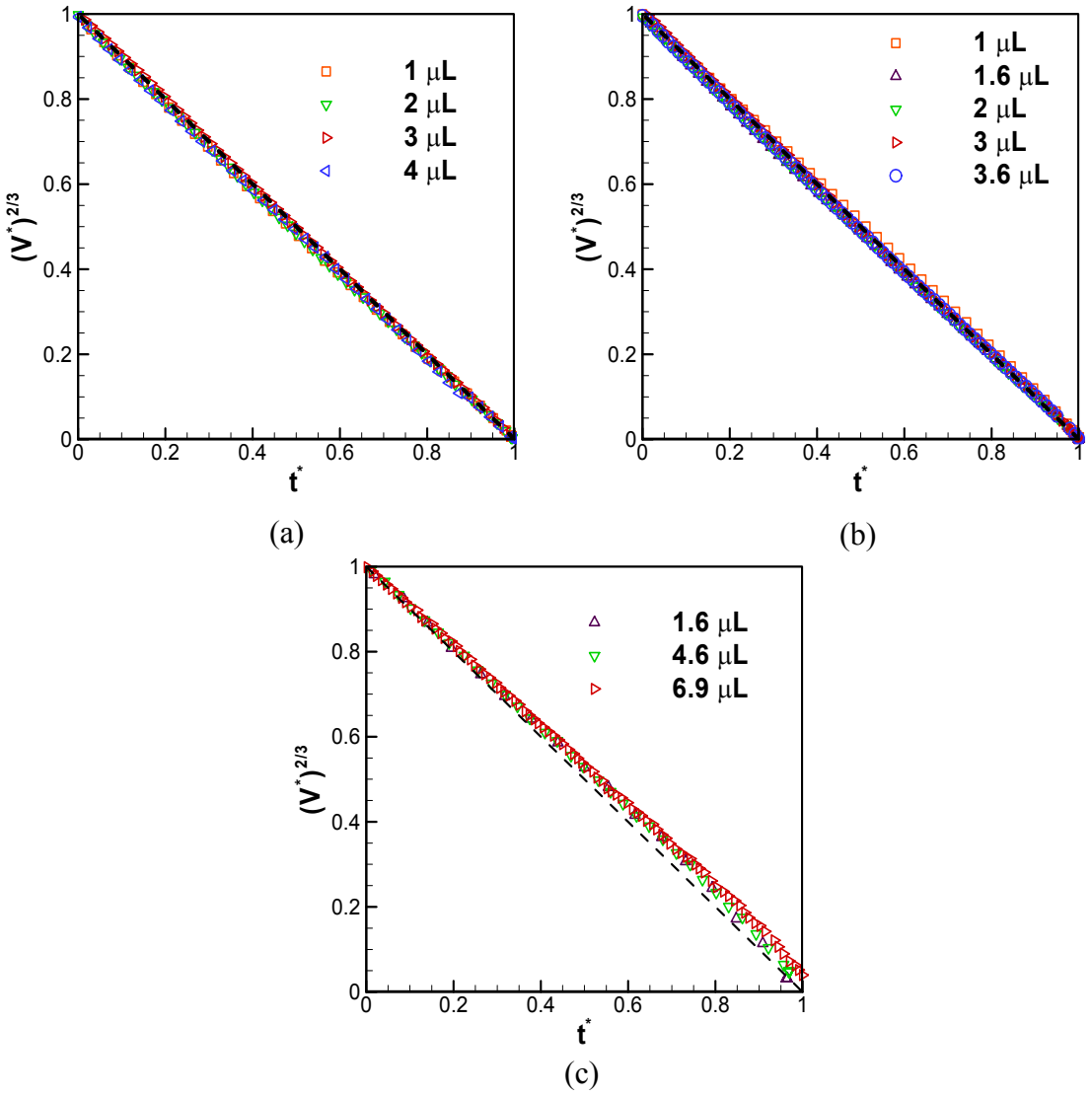

Figure 6.13. Variation of normalized droplet volume of the droplet raised to two-thirds power with non-dimensional time corresponding to evaporation on a (a) smooth hydrophobic surface, (b) superhydrophobic surface with negligible CAH, and (c) superhydrophobic surface with fixed CL [98]. The dashed lines represent the non-dimensional droplet transient volume predicted from Eq. (6.18).

6.4.3 Droplet Evaporation Characteristics on Heated Substrates

The experimental results for droplet evaporation on the heated hydrophobic and hierarchical superhydrophobic surfaces are discussed here in terms of the total time for evaporation, and the temporal variations of contact radius, contact angle, droplet volume,

and the average instantaneous evaporation flux. Evaporation occurs primarily in a CCA mode on both substrates. The experimental results for the two surfaces are compared against each other and with predictions from the vapor-diffusion-only model. A simple model is presented that takes into account the temperature drop across the height of the droplet due to conduction through the droplet and the interface temperature dependence of the local saturated vapor concentration.

6.4.3.1 Temporal Variation of Contact Radius and Contact Angle

Figure 6.14 shows the variation of droplet contact angle and nondimensional contact radius (nondimensionalized by the initial contact radius of the droplet) with respect to the time normalized by the total time of evaporation τ at three different substrate temperatures. The insets in Figure 6.14(a) and Figure 6.14(b) show the respective temporal evolution of droplet shape on the hydrophobic and superhydrophobic surfaces corresponding to the substrate temperature T_{sub} = 50 °C. The variation with normalized time of the transient contact angles and nondimensional contact radii for different substrate temperatures is more or less similar. On the hydrophobic substrate, the contact radius of the droplet is observed to decrease continuously as the droplet evaporates as shown in Figure 6.14(a). The droplet contact angle decreases from an initial contact angle to the receding contact angle value within the first 40% of the total time for evaporation. From then on, droplet evaporation occurs purely in a CCA mode till $\tau \sim 0.9$, followed by a mixed mode. This behavior is in contrast to droplet evaporation on unheated smooth hydrophobic surfaces where a distinct CCR mode was observed and the contact radius remained fixed for the first 20% of the evaporation time; with substrate

heating, the CCR mode is replaced by a mixed mode in which both the contact radius and contact angle decrease simultaneously. With the superhydrophobic surface, owing to the minimal contact angle hysteresis, the droplet evaporation occurs in a CCA mode for most of the evaporation period as seen in Figure 6.14b. The average droplet contact angle during evaporation on the superhydrophobic surface remains at ~ 160 deg. A stick-slip behavior is observed intermittently due to the surface roughness.

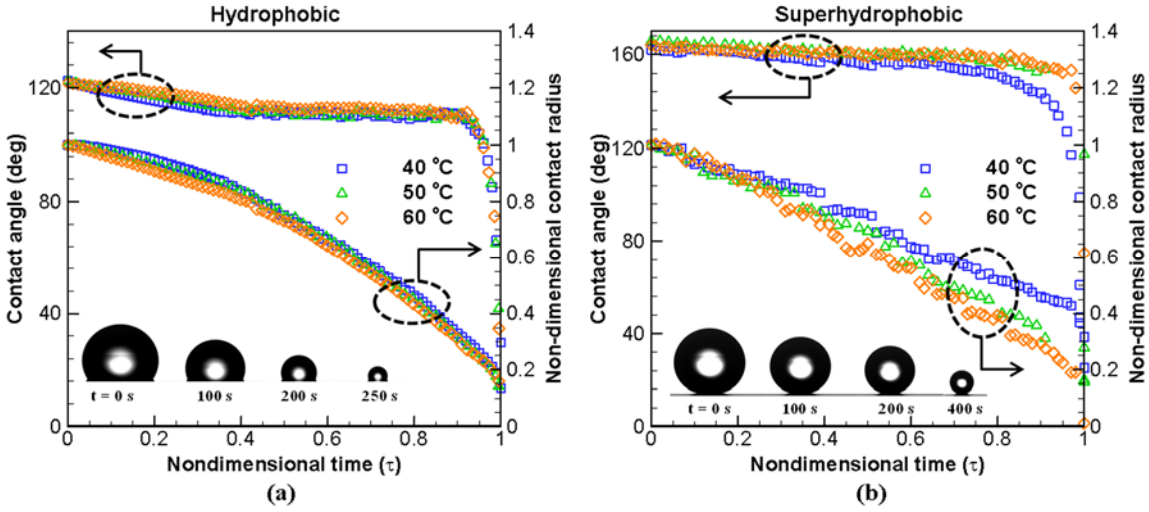

Figure 6.14. Variation of the droplet contact angle and nondimensional contact radius with respect to nondimensional time on the heated (a) hydrophobic surface and (b) superhydrophobic surface. The insets show the temporal variation of droplet shape corresponding to T_{sub} = 50 °C.

6.4.3.2 Total Time for Evaporation

It is important to assess the total time taken for the droplet to evaporate completely. In the presence of substrate heating, it is possible to reduce this time considerably as compared to an unheated case. Figure 6.15 shows the time taken for complete evaporation of a 3 μL water droplet on the hydrophobic and superhydrophobic surfaces. Total time for evaporation corresponding to unheated substrates is also included in the

graph (substrate temperature of 21°C). The times calculated from the vapor-diffusion model, Eq.(6.10), using the approximate value of the receding contact angles, *i.e.,* θ = 110 deg, for the hydrophobic substrate and θ = 160 deg for the superhydrophobic substrate are also shown in the plot. The theoretical values of the total time of evaporation on the hydrophobic and superhydrophobic substrates overlap closely as shown in the plot. The experimental behavior supports the exponential relation between the total time and substrate temperature proposed by Girard *et al*. [145]. The dependence of total time for evaporation t_F can be fitted with a power law, $t_F = aT_{sub}^{\ b}$ where a = 2510300, b = -2.34 for the hydrophobic surface and a = 767100, b = -1.91, for the superhydrophobic surface. There is an excellent match between the measured total time for evaporation and that predicted by the vapor-diffusion model in the case of the smooth hydrophobic surface. Conversely, a considerable mismatch is observed when the surface is superhydrophobic. The vapor diffusion model overpredicts the rate of evaporation on the superhydrophobic surface. This behavior is as opposed to droplet evaporation on a hydrophilic surface, where the isothermal diffusion-driven model was reported to underpredict the evaporation rate under heated conditions [97]. The time taken for complete evaporation of a droplet on the heated superhydrophobic surface is shown in Table 6.4. The uncertainties shown represent the standard deviation of the different test runs. Table 6.4 shows the deviation between the measured and predicted times for total evaporation on the superhydrophobic substrate. The deviation is amplified with increase in substrate temperature: from 31.2% at 40 °C to 50.8% at 60 °C. At room temperature, without substrate heating, a 20 – 25% deviation was reported for evaporation on a superhydrophobic surface without substrate heating.

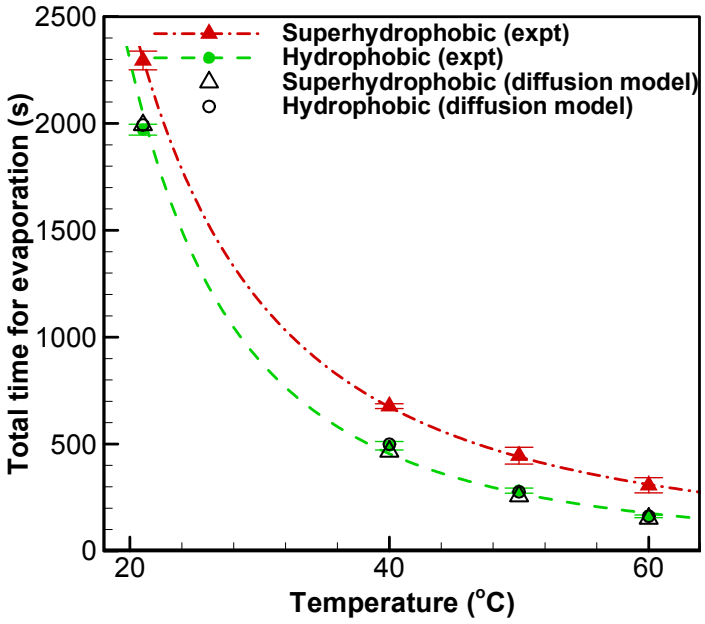

Figure 6.15. Total time for evaporation of droplets on the hydrophobic and superhydrophobic surfaces as a function of substrate temperature. The dashed lines represent a power fit to the experimental results. The hollow symbols represent the time for evaporation calculated from the vapor-diffusion model, Eq. (6.10).

Table 6.4. Total time for evaporation on the superhydrophobic substrate.

Substrate temperature (°C)	**Time taken for evaporation (s): Experimental**	**Time taken for evaporation (s): Vapor-Diffusion Model**	**Deviation (%)**
40	677 ± 11.4	465	31.2
50	445 ± 39.3	257	42.4
60	307 ± 35.5	151	50.8

6.4.3.3 Variation of Droplet Volume

The reduction in droplet volume over time during evaporation of the droplet is non-linear for both hydrophobic and superhydrophobic surfaces (Figure 6.16). This is similar to the behavior of droplet evaporation on hydrophobic and superhydrophobic surfaces

without substrate heating. Although the total time for droplet evaporation on the hydrophobic surface was found to be predicted very well by the vapor-diffusion model, the temporal variation of volume is not as well predicted (Figure 6.16a). This is in contrast with the droplet volume variation on an unheated hydrophobic surface, which was found to be predicted with remarkable accuracy by this model (as reported earlier)

In the case of the superhydrophobic surface, the vapor-diffusion model significantly overpredicts the experimental evaporation rate, and the percentage difference increases with an increase in substrate temperature (Figure 6.16b). The reason for the mismatch between the experimental results and the vapor diffusion model can be explained in terms of the competing effects of the buoyancy-induced convection in the vapor phase and the evaporative cooling along the interface, which will be described in detail in a following section.

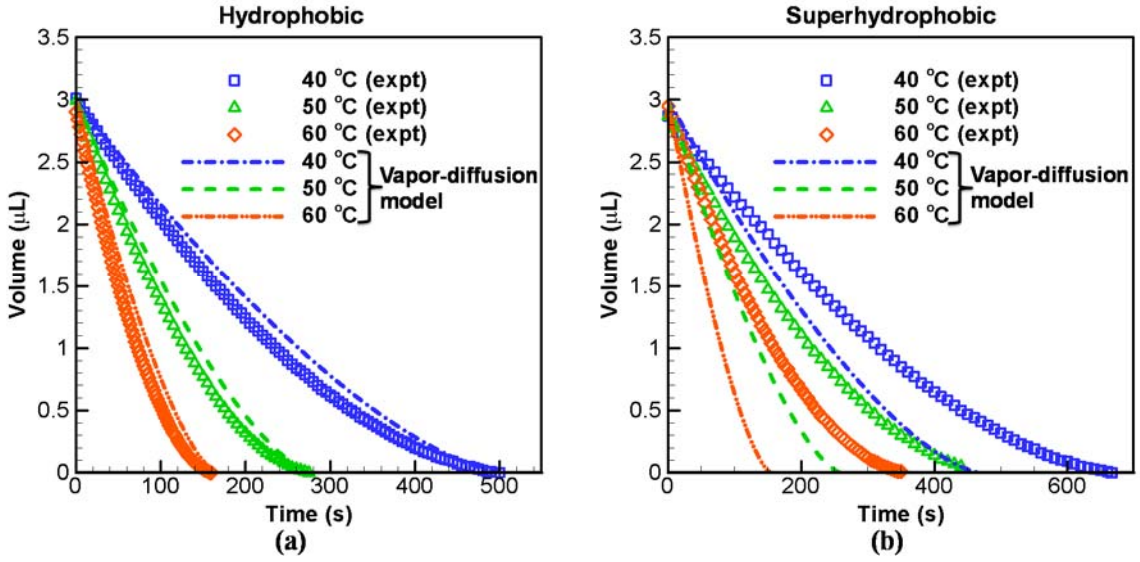

Figure 6.16. Temporal variation of droplet volume on the (a) hydrophobic and (b) superhydrophobic surfaces. The dashed lines represent the variation of droplet volume with respect to time as obtained from the vapor-diffusion model.

6.4.3.4 Variation of Average Evaporation Flux

The evaporation flux along the surface of an evaporating droplet is non-uniform except when the contact angle of the droplet is 90 deg [13]. Based on the vapor-diffusion model, while the flux is diverging near the contact line of a droplet with contact angle < 90 deg, the flux is actually finite near the contact line when the contact angle > 90 deg as described in an earlier section. Experimental determination of the local evaporation flux is challenging due to the difficulty in determination of the local vapor concentration as well as the temperature at the droplet interface. The area-averaged flux over the droplet surface is calculated using $J_{avg} = \frac{\rho \, dV/dt}{A}$ where ρ, A, and V are the density, surface area, and volume of the droplet, respectively. Figure 6.17(a) and Figure 6.17 (b) show the variation of average evaporation flux with respect to the transient volume of the droplet for both surfaces. The average evaporation flux increases as the droplet evaporates on the hydrophobic and the superhydrophobic substrates; that is, the flux increases with reduction of instantaneous droplet volume during evaporation. Towards the end of evaporation, corresponding to the period where droplet evaporation occurs in the mixed mode, there is a steep increase in the evaporation flux. For the same substrate temperature, the droplet evaporating on the hydrophobic surface has a higher evaporation flux as compared to the superhydrophobic surface, which can also be concluded from the lower time of evaporation in the case of evaporation on a hydrophobic surface.

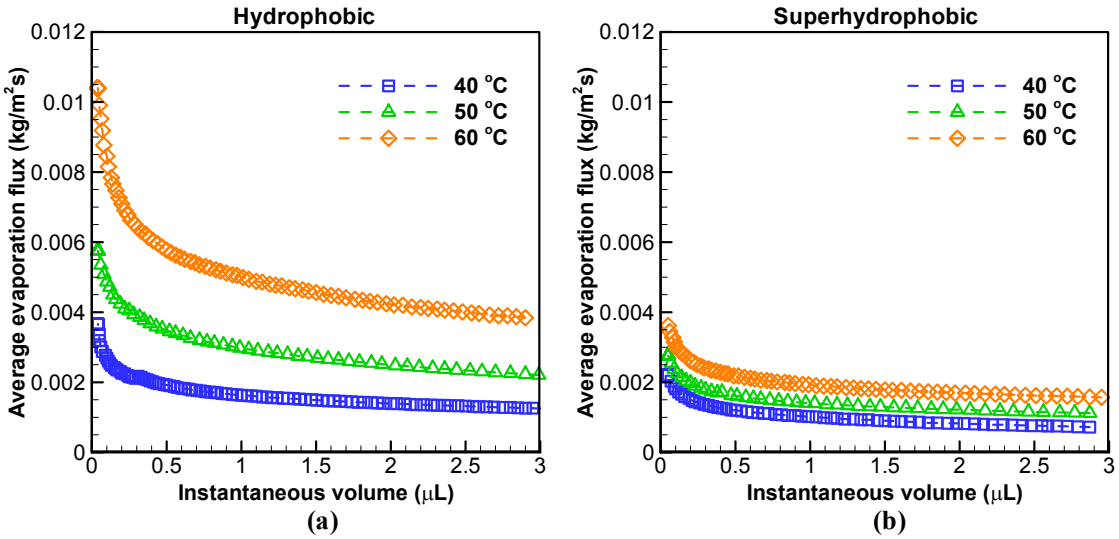

Figure 6.17. Average evaporation flux with respect to instantaneous droplet volume for different substrate temperatures on the (a) smooth hydrophobic and (b) superhydrophobic substrates.

6.4.4 Evaporation Suppression on the Superhydrophobic Surface

The different factors that result in evaporation suppression in the case of a superhydrophobic surface are analyzed. A simplified thermal diffusion model is developed to illustrate the mechanisms leading to the inability of the diffusion-based model to explain evaporation on such surfaces.

6.4.4.1 Geometric Constriction

The diffusion model [13] takes into account the non-uniform evaporation flux at the surface of the droplet. The evaporation flux computed using the Eq. (6.1) for a droplet of volume 3 μL with different contact angle values evaporating without substrate heating is shown in Figure 6.18. Contact angles (θ) of 30, 60, 90, 120, 150, and 160 deg are selected corresponding to a constant volume of 3 μL to illustrate the difference in the variation of the evaporation flux on the droplet surface (Figure 6.18) at the different contact angle. The evaporation flux was shown to be diverging at the contact line

analytically and experimentally by Hu *et al*. [87] for droplets with low CA ($\theta < 90$ deg), as also shown in Figure 6.18. For a hemispherical droplet ($\theta = 90$ deg), the evaporation flux is constant all along the surface of the droplet. However, when the contact angle exceeds 90 deg, the evaporation flux is maximum at the highest point of the droplet (corresponding to $r/R_c = 0$). The flux remains almost uniform along the upper half of the droplet surface and reduces to zero near the contact line. This shows that Popov's diffusion model takes into account the saturation of vapor, and the resulting reduction of local evaporation flux near the contact line. In spite of this, the presence of disparities between the analytically predicted and experimental rates of droplet evaporation on a superhydrophobic surface signifies that the difference is not due to the local geometric constriction near the contact line as has been suggested in earlier studies [17].

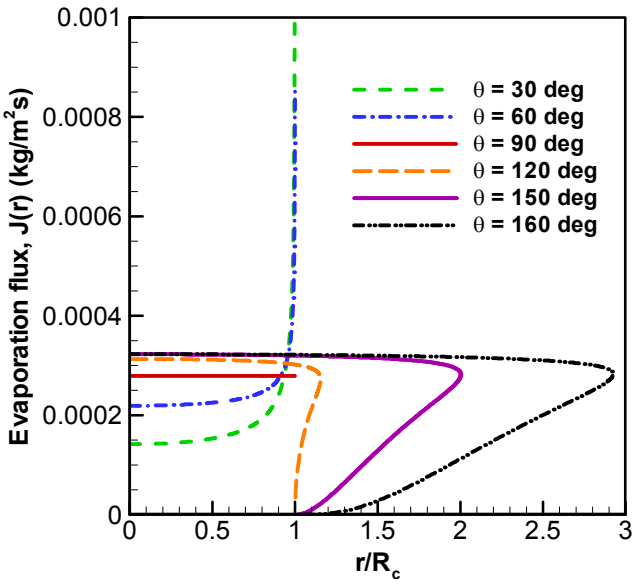

Figure 6.18. Variation of evaporation flux along the droplet surface corresponding to different contact angles at $t = 0$ s.

6.4.4.2 Evaporative Cooling Effect at the Droplet Interface

A possible reason for the observed increase in the total time of droplet evaporation on a superhydrophobic surface may relate to the evaporative cooling effect at the droplet interface. Two factors could contribute to the interface cooling. The first is the effective thermal conductivity of the substrate. David *et al.* [85] reported that pinned droplets on insulating substrates take longer to evaporate than on highly conducting substrates due to evaporative cooling. Structured surfaces are rendered superhydrophobic by their ability to retain air gaps [71]. The stability of the air gaps and the reduced solid-liquid contact area with the superhydrophobic surface results in the high droplet contact angles, and the reduced CAH, observed. The very low conductivity of air (0.024 *W/mK*) reduces the effective conductivity of the substrate, which can in turn reduce the rate of evaporation due to evaporative cooling of the droplet. The effective thermal conductivity of the structured layer in this work, consisting of silicon pillars and photoresist of ~ 23 μm height and assuming a conductivity of 0.25 *W/mK* for the AZ 9260 photoresist, is determined to be 0.54 *W/mK* (details are included in the Supporting Information). On the other hand, a higher CAH [17] is an indication of the air gaps in the structured surfaces being replaced by liquid, resulting in a higher effective conductivity than in the case where the air gaps are retained.

The second and most important factor contributing to interface cooling is the thermal resistance of the droplet. A droplet placed on a superhydrophobic surface maintains a high contact angle throughout evaporation which implies that for a fixed droplet volume, the ratio of droplet height to its corresponding contact radius remains consistently high (for CA = 160 deg, $h/R_c \sim 5.7$). This leads to a longer thermal resistance path within the

droplet (conductivity of water = 0.6 *W/mK*) resulting in significant evaporative cooling compared to droplets with lower contact angles. The isothermal diffusion model indicates that the total time for evaporation of a droplet is almost the same for both CCA and CCR modes when the initial CA ≥ 150 deg [146], which is not the case in reality. Kulinich and Farzaneh [17] reported that the time taken for complete evaporation of the droplet on a superhydrophobic surface with a pinned contact line was higher than for a sliding contact line, although the initial contact angle of the droplet was ≥ 150 deg in both cases. In the present experiments, evaporation occurs in the CCA mode. This is in contrast to droplet evaporation in a CCR mode where the contact angle decreases to account for evaporation, thereby reducing the thermal resistance path within the droplet. Thermal conduction through the droplet plays a significant role in determining the rate of evaporation especially on a superhydrophobic surface.

A model is developed here to demonstrate the influence of evaporative cooling on the rate of droplet evaporation on a heated substrate. The relative importance of the convective and the diffusive transport inside the droplet can be determined using the nondimensional Peclet number ($Pe = UL/\alpha$) where U, L, α represent the characteristic velocity, length scale, and thermal diffusivity of the droplet. Using a characteristic velocity of tens of micron per sec [9, 147], and the droplet height as the characteristic length scale, the Peclet number for a 3 μL droplet is calculated to be less than 1, signifying the dominance of the diffusive transport inside the liquid droplet. Similar conclusions regarding the minimal contribution of the convection inside the droplet on the net evaporation rate were made by Pan *et al*. [148] using a full-scale numerical model. The model developed in the present work accounts for thermal diffusion through the

liquid droplet and vapor diffusion through the surrounding gas, while convection in the gas and liquid domains is neglected. The influence of the convection in the vapor domain can be analyzed based on the comparison between this model and the experimental results. Heat is conducted from the heated substrate through the droplet and utilized for phase change at the liquid-vapor interface. The substrate is held at a uniform constant temperature. The ambient temperature and humidity are taken as 21 °C and 36% to match the experimental conditions. One-dimensional conduction is assumed along the vertical axis. The droplet volume is discretized into disks parallel to the droplet contact area, as shown in Figure 6.19. The one-dimensional heat conduction model implies that the temperature laterally over each control volume remains uniform and the surface temperature variation occurs only along the vertical axis of the droplet. The energy balance over each control volume can be written as

$$-kA_b \left.\frac{dT}{dx}\right|_b = -kA_t \left.\frac{dT}{dx}\right|_t + J(r)\, h_{fg}\, dS\,, \tag{6.19}$$

where k is the thermal conductivity of the liquid droplet (k = 0.6 *W/mK* for water), A_b and A_t are respectively the bottom and top face-areas of the control volume, h_{fg} is the latent heat of vaporization, and dS corresponds to the surface area of the control volume representing the liquid-air interface. The evaporation flux $J(r)$ in Eq (6.19) is initialized as the theoretical flux obtained from the vapor-diffusion model using Eq. (6.1) and evaluated at the substrate temperature. The thermophysical properties are evaluated at the interface temperature (initialized as the substrate temperature). The saturated vapor concentration at the droplet interface is coupled with the saturation pressure and hence

the local interface temperature at the droplet. The saturation pressure $p_{sat}(T_{lv})$ is calculated using the Clausius-Clapeyron equation,

$$p_{sat}(T_{lv}) = p_{sat\_ref} \exp\left(\frac{Mh_{fg}}{R}\left(\frac{1}{T_{sat\_ref}} - \frac{1}{T_{lv}}\right)\right) \tag{6.20}$$

$$C_v\big|_{lv} = \frac{p_{sat}(T_{lv})}{RT_{lv}} \tag{6.21}$$

$$h_{fg} = 2.7554\times10^{6} - 3.46\,T^{2}. \tag{6.22}$$

The energy equation Eq (6.19) is solved to obtain temperatures using the finite volume method in MATLAB using a forward-difference scheme. The updated local temperatures are used to determine the evaporation flux and the thermophysical parameters (P_{sat}, C_v, h_{fg}) in subsequent iterations. The energy equation is solved and iterated upon until convergence and the resultant surface temperature profile is obtained along the vertical axis of the droplet.

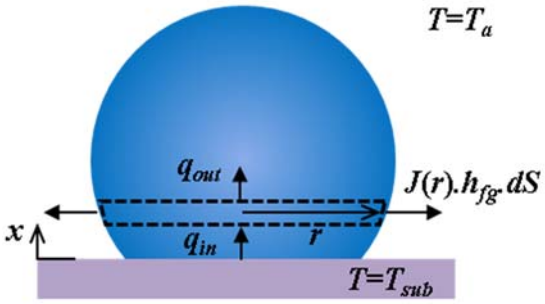

Figure 6.19. Control volume approach to determining the axial droplet interface temperature subject to evaporative cooling.

The interfacial temperatures of a 3 μL droplet obtained by solution of Eq. (6.19), with contact angles of 110 deg and 160 deg, are plotted in Figure 6.20a and Figure 6.20b, respectively. The magnitude of the evaporative cooling is assessed based on ΔT, the

difference between the substrate temperature and the minimum temperature which occurs at the top of the droplet interface, as shown in Table 6.5. The magnitude of interfacial cooling increases with an increase in substrate temperature for both the contact angles considered (Table 6.5). For droplet evaporation in the CCA mode, the total time of evaporation is related to the inverse of the rate of evaporation, as seen from Eq. (6.3) and Eq. (6.10). The ratio of the measured evaporation rate $dm/dt\big|_{\exp t}$ and that given by the vapor-diffusion-only model $dm/dt\big|_{diff}$ is hence obtained as the ratio of the total time for evaporation from Eq. (6.10), and from the measured values in the form of $\left(dm/dt\big|_{\exp t}\right)\Big/\left(dm/dt\big|_{diff}\right) \sim (t_F)_{diff}/(t_F)_{\exp t}$. The evaporation rate increases with substrate heating, resulting in an increased rate of cooling, and sustains a larger temperature differential across the droplet.

The effect of evaporative cooling on the interface temperature is much larger in the case of the superhydrophobic surface compared to the smooth hydrophobic surface for the substrate temperatures considered (Table 6.5). This can be explained in terms of the higher height-to-contact-radius aspect ratio of a droplet on the superhydrophobic surface than on the hydrophobic surface, h/R_c = 5.67 (CA = 160 deg) versus h/R_c = 1.43 (CA = 110 deg). The longer conduction path (h) and a significantly lower conduction base area ($A_c = \pi R_c^2$) in the case of the superhydrophobic surface as compared to the hydrophobic surface result in a larger temperature differential in the former. In contrast, for a hydrophilic surface, the low contact angle of the droplet implies a significantly lower h/R_c aspect ratio. The temperature drop across a droplet on hydrophilic surfaces is thus minimal, as reported by Girard *et al*. [145].

Despite the considerable temperature drop predicted for the hydrophobic substrate, the total time for evaporation recorded experimentally shows excellent agreement with the vapor-diffusion-only model (Table 6.5). A similar observation was made by Pan *et al*. [148], who reported that under unheated substrate conditions with a droplet contact angle of 110 deg, the suppression of evaporation caused by the evaporative cooling effect is compensated by the convective flow in the air which tends to enhance the rate of evaporation. The agreement between the current experimental results and the vapor-diffusion-only model even at elevated temperature indicates that the buoyancy-driven convection balances the evaporative cooling effect even as the interface cooling increases with an increase in the substrate temperature. This implies that the evaporation enhancement effect of buoyancy-induced convection would be amplified as the substrate temperature is increased. Conversely, for the superhydrophobic surface, there is a considerable difference between the measured and predicted time of evaporation. This indicates that the enhancement of evaporation rate due to convection in the air and liquid domains is not sufficient to compensate for evaporation suppression due to the lowered interface temperature. For hydrophilic surfaces, on the other hand, the vapor diffusion model has been shown to underpredict the rate of evaporation when subject to substrate heating [96, 97]. This is because the suppression of the evaporation rate by lowering the interface temperature is negligible in case of the hydrophilic surface, and the effect of buoyant convection-induced enhancement of the evaporation rate is dominant.

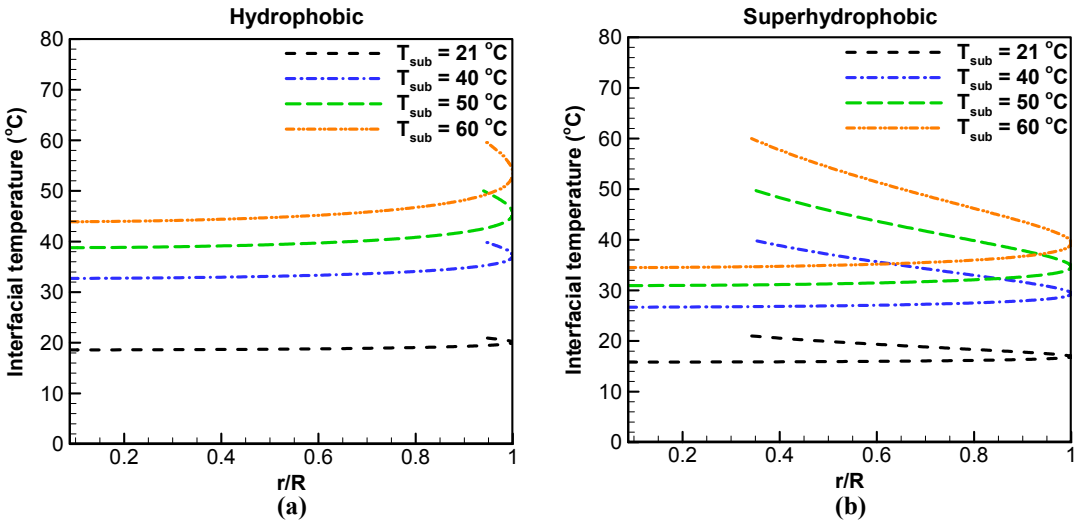

Figure 6.20. Interfacial temperature of a droplet of 3 μL volume at different substrate temperatures corresponding to the (a) hydrophobic (θ = 110 deg) and (b) superhydrophobic substrates (θ = 160 deg). The radial location r along the droplet interface is normalized by the droplet radius (R).

Table 6.5. Interfacial temperature of droplet subject to evaporative cooling.

T_{sub} (°C)	**Hydrophobic Substrate (θ = 110 deg)**		**Superhydrophobic Substrate (θ = 160 deg)**	
	ΔT (°C)	**Evaporation time ratio $(t_F)_{diff}/(t_F)_{expt}$**	**ΔT (°C)**	**Evaporation time ratio $(t_F)_{diff}/(t_F)_{expt}$**
21	2.41	1.011	5.17	0.770
40	7.28	1.003	13.3	0.687
50	11.22	0.984	19.05	0.576
60	16.09	0.970	25.49	0.492

6.5 Summary

Evaporation of droplets on a hierarchical superhydrophobic surface with negligible contact angle hysteresis is shown to occur only in a constant contact angle mode. The influence of substrate temperature on the evaporation characteristics of droplets on

hydrophobic and superhydrophobic surfaces is also experimentally investigated. The experimental results are compared with a vapor-diffusion model which assumes the droplet temperature to be equal to the temperature of the substrate. Although the vapor-diffusion-only model predicts the evaporation characteristics on a smooth hydrophobic surface with reasonable accuracy, it overpredicts the rate of evaporation for the case of superhydrophobic surfaces having low contact angle hysteresis. This disagreement is amplified with an increase in the substrate temperature (deviation ~20 percent for unheated case and ~ 50 percent when the substrate temperature is equal to 60 °C). Quantitative results for the total time of evaporation, temporal variation of droplet volume, contact radius and contact angle are presented. The reduction in the rate of evaporation is attributed to the suppression of evaporation primarily by evaporative cooling at the droplet interface due to the high aspect ratio of the droplet leading to a longer thermal resistance path, and the low effective conductivity of the substrate owing to the presence of the air gaps. An adjustment factor is proposed to account for the suppression of evaporation, and is found to accurately predict the transient droplet volume on the unheated superhydrophobic surface. Based on our experimental observations and results from the literature, a generalized relationship for predicting the instantaneous volume of droplets under ambient conditions with initial CA > 90 deg, irrespective of the mode of evaporation, is presented. A simple model is solved to determine the non-uniform interface temperature which is lower than the substrate temperature. This model highlights the importance of evaporative cooling on reducing the resultant rate of evaporation of the droplet, especially in the case of superhydrophobic surfaces.

CHAPTER 7. EVAPORATIVE CONVECTION FLOW IN DROPLETS EVAPORATING ON HEATED HYDROPHOBIC AND SUPERHYDROPHOBIC SURFACES

In the current chapter, we experimentally demonstrate that the recirculating flow field inside a sessile droplet evaporating on heated smooth hydrophobic, and superhydrophobic substrates is driven by thermal buoyancy forces. We employ Particle Image Velocimetry, and a subsequent velocity-correction algorithm that takes into account the refractive index mismatch when viewing through the spherical interface of the droplet, to quantitatively determine the flow velocity magnitude. In the case of a hydrophobic substrate, a cross-section of an axisymmetric toroidal vortex, with flow directed upwards along the droplet vertical axis, is observed at the central plane of the droplet. The inward motion of the seeding particles at the sliding contact line explains the localized particulate deposition observed on smooth hydrophobic surfaces at the center of an evaporated droplet footprint. We evaluate the dependence of the flow field on the instantaneous droplet volume and substrate temperature. A scaling analysis is used to relate the observed velocities inside the droplet to the Rayleigh number.

On the superhydrophobic substrate, an asymmetric vortex, with a solid-body rotation flow pattern is observed; this is in stark contrast with the axisymmetric flow pattern that develops on hydrophilic and hydrophobic substrates. This asymmetric flow pattern develops due to the large height-to-diameter aspect ratio of the droplet, which dictates a

stable buoyancy-induced convection mode with one rolling vortex. The flow velocity is shown to increase with substrate temperature and is an order of magnitude higher compared to droplets evaporating on hydrophobic substrates. We propose a unique method to use such evaporation-induced flow on superhydrophobic substrates as a means to promote efficient 'on-the-spot' mixing in microliter droplets. In addition, the high recirculation velocity combined with the sliding contact line of the droplet minimizes a distributed deposition of particles on the substrate during the evaporation process, enabling a single concentrated deposition after complete drying on superhydrophobic substrates. The project was done in collaboration with Aditya Chandramohan. A part of the material presented in this chapter is submitted for publication.

7.1 Experimental Setup

In the experiment, a deionized water droplet of 3 ± 0.5 μL initial volume is allowed to evaporate on a hydrophobic substrate (Teflon-coated silicon wafer) placed inside a transparent enclosure to avoid disturbance due to external air flow. The experimental setup is shown in Figure 7.1. The initial contact angle of the droplet is 118 ± 2 deg and the contact angle hysteresis is ~10 deg. The superhydrophobic substrate is fabricated with silicon prime wafers using standard lithography and dry etching (deep reactive-ion etch) techniques. The fabrication was carried out in the Birck Nanotechnology Center at Purdue University. The surface has a square array of pillars, as shown as the inset in Figure 7.2. The pitch of the pillars is ~30 μm, the width of the tops of the pillars ~10 μm, and the height of the pillars ~20 μm. The textured surfaces were coated with Teflon (~50 nm thickness) to render them superhydrophobic. The initial contact angle (CA) of the droplet is 157 ± 2 deg and the contact angle hysteresis is ~ 10 deg. Experiments are

conducted at three different substrate temperatures: 40 °C, 50 °C, and 60 °C. The ambient temperature and humidity are maintained at 24 ± 1 °C and 36 ± 3%, respectively.

The water droplet is seeded with 1 μm-diameter fluorescent polystyrene microspheres with peak excitation and emission at 532 nm and 602 nm, respectively. A continuous diode-pumped solid-state Nd:YAG laser (Coherent Verdi V5; 532 nm) along with a Galilean lens arrangement is used to produce a light sheet with thickness ~ 30 μm and height ~ 6 mm that illuminates the vertical central plane of the droplet. A laser power of 1 W is used in the experiments. Water has a very low absorption coefficient at the laser wavelength [149]; hence, laser-induced heating of water during the experiment is negligible. A high-speed camera (Photron FASTCAM 1024PCI) fitted with a microscopic lens (Keyence VH-Z50L) and a high-pass filter (center wavelength = 620 nm, bandwidth = 52 nm) captures the light emitted from the seeding particles at 60 frames per second at a spatial resolution of ~ 3.8 μm/pixel. Figure 7.1 shows a schematic diagram of the experimental setup. A modified lens arrangement is used for visualization of the horizontal cross-sectional plane of the droplet. Figure 7.2a and Figure 7.2b show the streaklines in the vertical and horizontal plane of the droplet obtained by overlapping multiple sequential images in the case of the hydrophobic and superhydrophobic substrate respectively. All experimental results presented are acquired during the constant contact angle mode of evaporation, during which the mass loss due to evaporation results in a corresponding reduction in the height and contact radius of the droplet.

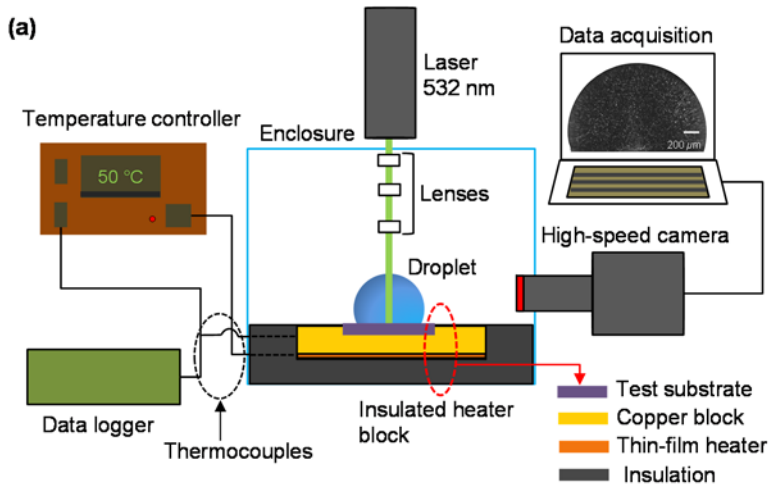

Figure 7.1. (a) Experimental setup for flow visualization using Particle Image Velocimetry.

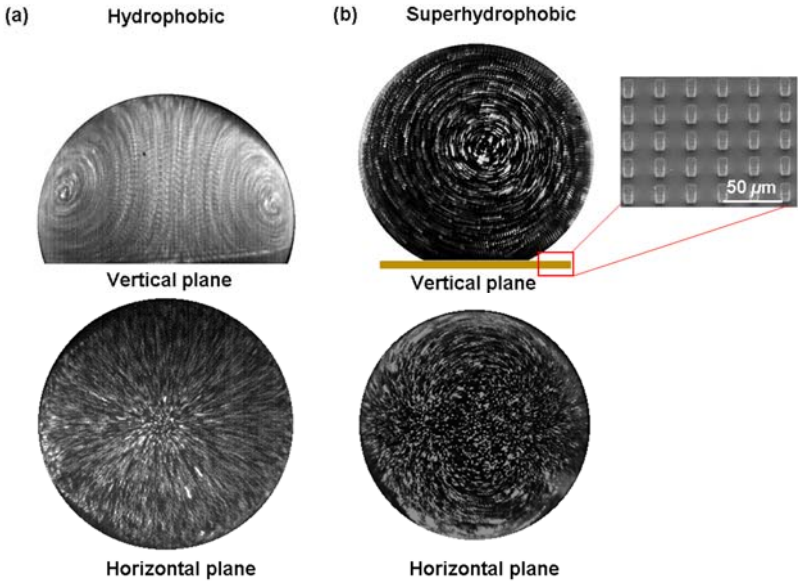

Figure 7.2. Streaklines visualized by superimposing multiple sequential side-view and top-view images on a (a) hydrophobic (b) superhydrophobic substrate. The inset shows the SEM image of the superhydrophobic substrate used in the experiment.

The PIV vector field is computed using the software LaVision 8.1.4. A multi-pass, cross-correlation algorithm with first- and second-pass window sizes of 32 × 32 and 16 ×

16 pixels, and 50% overlap between consecutive frames, is used to obtain a converged velocity vector field. The instantaneous vector fields at each grid location are time-averaged over a droplet volume change of ± 0.1 μL due to evaporation to obtain a vector field inside the droplet corresponding to a given volume; for instance, velocity vectors obtained during a droplet volume change from 2.1 μL to 1.9 μL are used to obtain the time-averaged vector field attributed to the droplet volume of 2 μL.

7.2 Results and Discussion

7.2.1 Flow Behavior on a Hydrophobic Substrate

The velocity vectors are distorted (through a distortion in the cross-correlated particle positions) due to the spherical shape of the droplet interface which acts as a liquid lens. As a result, the vectors are severely compressed at the periphery (resulting in loss of vector data) and magnified at the center of the droplet [110]. A velocity-correction algorithm [110,150] is employed to correct for this distortion and to obtain an accurate quantitative estimate of the flow field. The velocity mapping algorithm proposed by Kang *et al*. [110] is used with the correction reported by Minor *et al*. [150] incorporated. The ray-tracing method calculates the actual position of the particles based on the surface curvature and index of refraction of the liquid droplet. The ray-tracing is realized by projecting the particle position, obtained from the captured image on the camera, onto the surface of the droplet by assuming that the droplet has a spherical profile. Based on the refractive indices of air and water, the surface projection is traced to the center plane of the droplet to determine the actual (*i.e.*, corrected) particle position using Snell's law. The velocity vector correction is obtained by taking the derivative of the position correction [110]. The velocity field correction algorithm requires geometric

characterization of the droplet contact radius, height, and the coordinates of the center of the base contact area, which are determined from the experimental images. Using an in-house image processing code developed in MATLAB (The Mathworks Inc., Natick, MA), the droplet image noise is reduced and the reflections removed. Subsequently the image is binarized and a boundary detection algorithm is used to determine the droplet profile, from which the geometric parameters of the droplet are estimated.

Figure 7.3 shows the vector plot in the central plane of the droplet before and after vector position and magnitude correction. At the center of the droplet, the lens effect artificially magnifies the actual velocities by approximately 34% at 50 °C (Figure 7.3). The optical distortion at the droplet interface significantly expands the positions and increases the magnitudes of the vectors at the center of the visualization plane. Vector positions near the interface are heavily compressed toward the interface, ultimately resulting in a loss of information in this region even after correction [110]. It should be noted that the shifted vectors produced by the correction algorithm allow identification of the actual position of the vortex center in the plane of visualization (Figure 7.3). The uncertainty in determination of the corrected vectors is dependent on the errors in the measurement of the droplet contact radius, height, and center of the base contact area, which are each estimated to be within 1 pixel. The root-sum-squared approach was taken to assess this uncertainty, which was found to be within 2 μm/s.

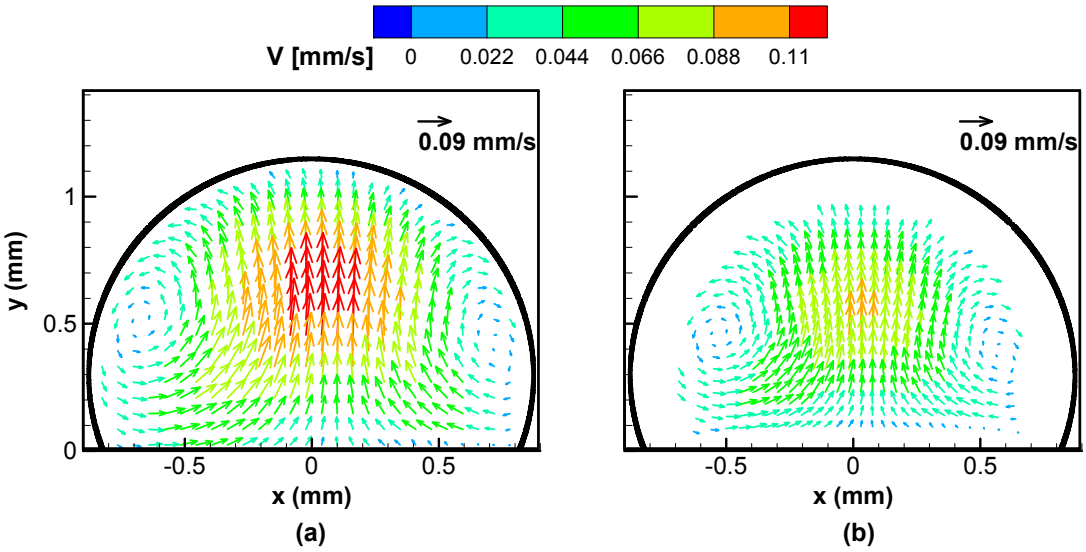

Figure 7.3. Velocity vectors corresponding to substrate temperature of 50 °C (a) before and (b) after velocity correction, at a droplet instantaneous volume of 2 μL.

Figure 7.5a and Figure 7.5b respectively show the velocity fields on the central vertical plane when the droplet has evaporated down to a volume of 2 μL and 1.2 μL on a substrate maintained at 50 °C. A cross-section of the toroidal vortex, appearing as a counter-rotating vortex pair in the 2D plane, is observed with flow directed inward towards the center of the droplet along the substrate and upward along the vertical axis. This flow behavior is in stark contrast to that on a hydrophilic surface where the flow along the substrate is directed outwards towards the contact line [13,101]. Earlier studies have attributed the recirculating flow inside an evaporating droplet to the Marangoni convection caused by surface tension gradient along the interface [101,104]. The Marangoni number is defined as $Ma = \frac{-d\sigma}{dT}\frac{1}{\mu\alpha}L\Delta T$ where dσ/dT is the change in surface tension due to temperature, and μ, α, L, and ΔT represent the dynamic viscosity, thermal diffusivity, length scale of the droplet, and temperature difference across the droplet,

respectively. The temperature gradient on the surface of the droplet, which determines the direction of the Marangoni flow, is dependent on the geometry and the thermophysical properties of the droplet and substrate. Typically, a radially outward flow along the substrate is reported. Recent studies have reported a flow directed inwards along the substrate under unique conditions, such as when the droplet contact angle is less than 14 deg [110,151,152], and when the substrate-to-droplet thermal conductivity ratio k_R is low ($k_R < 2$) [103]. If Marangoni convection were important in our experiments (CA ≈ 110 deg and $k_R > 250$), the flow would be directed outward along the solid-liquid interface towards the contact line and downward along the vertical axis. Instead, the observed upward direction of flow along the vertical axis indicates that the driving parameter here is the density gradient caused by the temperature stratification in the droplet; *i.e.*, buoyancy-induced Rayleigh convection is dominant.

A significant temperature drop may be sustained across an evaporating droplet due to evaporative cooling at the interface on a hydrophobic surface which supports a large contact angle [148]. Thus, the liquid nearer the heated surface is at a higher temperature and lower density compared to the liquid at the top of the droplet. This results in an unstable equilibrium: the denser liquid at the top descends while the lighter liquid at the bottom ascends, and this global motion within the droplet leads to a three-dimensional toroidal vortex pattern. The absence of the outward capillary flow seen with hydrophilic surfaces is attributed to the unpinned contact line and reduced evaporative flux near the contact line compared to droplets with an acute contact angle as described in the previous chapter. The axisymmetric nature of the toroidal vortex pattern is further confirmed by PIV visualization in the horizontal plane of the droplet with the maximum diameter (at

$y/h \approx 0.23$, where y and h represent the distance from the base of the droplet, and the droplet height, respectively); velocity vectors in this plane confirm the inward flow of particles towards the vertical axis along the substrate (as included in the Supplementary Material). The Galilean lens arrangement is modified (compared to the one described in Figure 7.1a) so as to illuminate a horizontal cross-section of the droplet. The horizontal plane of the droplet (corresponding to the maximum diameter) is chosen as the plane for visualization so as to minimize the distortion of the light sheet path due to refraction at the curved interface. The placement of the camera is also altered to visualize this horizontal plane.

Figure 7.4a and Figure 7.4b show the uncorrected and corrected velocity vectors, respectively, in the central horizontal plane of a droplet evaporating on a hydrophobic surface maintained at 40 °C, corresponding to an instantaneous droplet volume of 2.1 ± 0.1 μL. The flow is observed to be directed inwards towards the center. This is also supported by the results obtained in the vertical cross-section of the droplet, as discussed previously, and affirms the axisymmetric, toroidal vortex flow structure in the droplet.

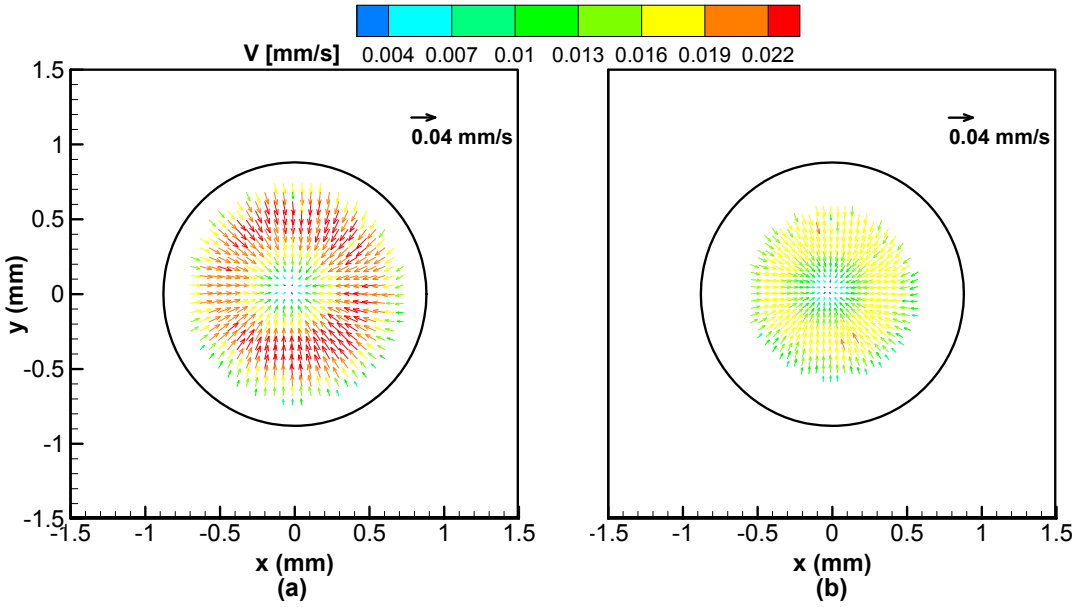

Figure 7.4. Flow visualization at the horizontal plane of the droplet at $y/h \approx 0.23$ corresponding to hydrophobic substrate temperature of 40 °C (a) before correction and (b) after correction.

This buoyancy-induced flow recirculation, in conjunction with the sliding contact line, explains the localized deposition pattern observed in the case of hydrophobic surfaces [24]. The flow pattern observed here is analogous to the solute-buoyancy-induced flow reported by Kang *et al*. [153].

A comparison of the velocity fields inside the droplet corresponding to instantaneous droplet volumes of 2 μL and 1.2 μL may be drawn from Figure 7.5. The flow velocities decrease as the droplet volume (and correspondingly, the rate of evaporation as reported in the previous chapter) decrease. This reduction in velocity magnitude can be explained in terms of the driving buoyancy forces, assessed using the Rayleigh number given by $Ra = \frac{\rho g \beta}{\mu \alpha} \Delta T L^3$ where ρ and β are the density and thermal expansion coefficient of the liquid, respectively. The Rayleigh number decreases with a reduction in the length scale

(height of the droplet), resulting in a lowered buoyancy-induced convection velocity at lowered volumes (Figure 7.5b).

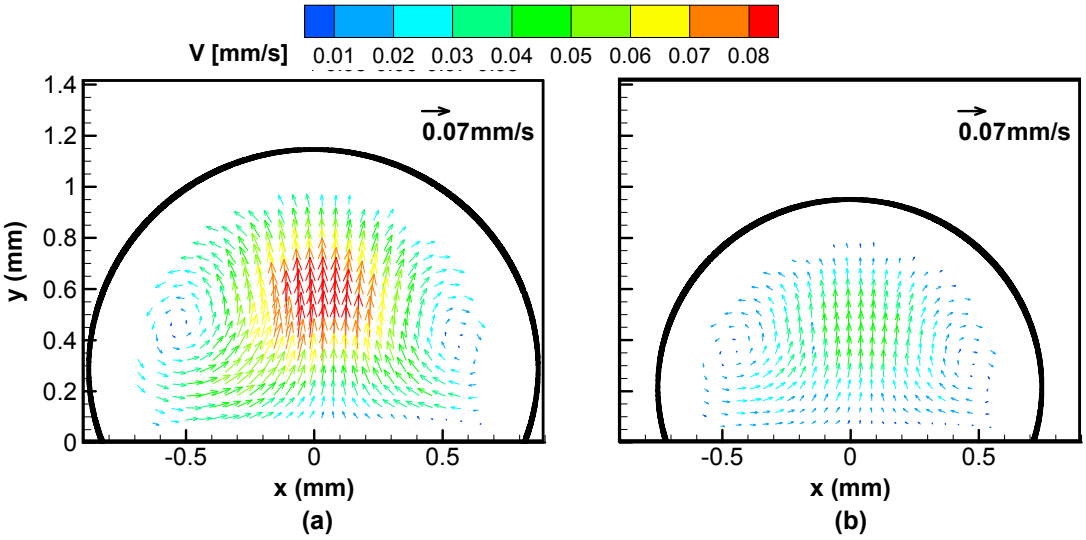

Figure 7.5. Comparison of velocity fields at the central vertical plane inside a droplet evaporating on the hydrophobic substrate maintained at 50 °C at instantaneous volumes of (a) 2 μL and (b) 1.2 μL.

The flow velocities (and rate of evaporation) increase with an increase in substrate temperature. To illustrate this increase, the velocities extracted along the central vertical axis of the droplet at the instantaneous volume of 2 μL corresponding to different substrate temperatures are shown in Figure 7.6. The increase in buoyancy-induced flow velocity can be attributed to the higher temperature drop across the droplet at elevated temperatures (as determined in the previous chapter). An interesting observation is that, irrespective of the substrate temperature, the velocity is highest at $y/h \approx 0.4$. The high velocity at this location may be explained by proximity to the center of the toroidal vortex. Figure 7.7 shows the velocity magnitude along the vertical axis of symmetry of the droplet as it evaporates on substrates maintained at different substrate temperatures.

The velocity field behavior with decreasing volume is very consistent across all the substrate temperatures considered.

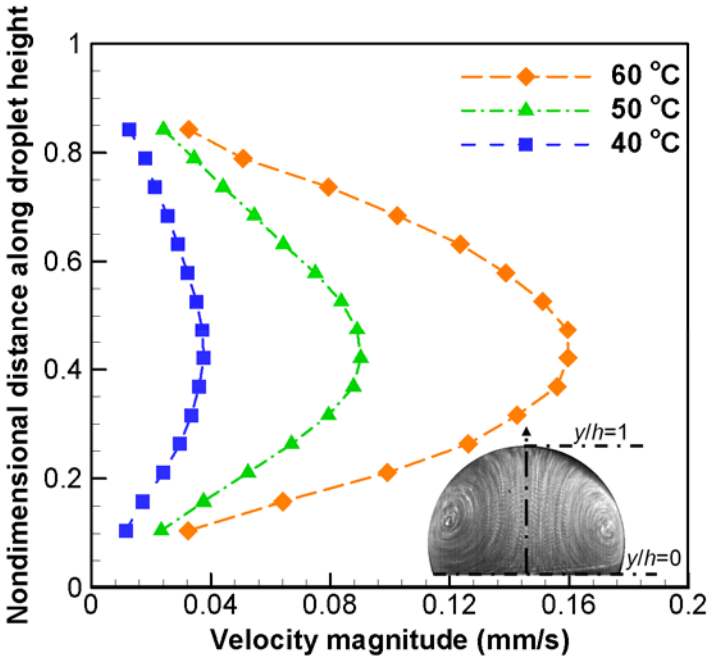

Figure 7.6. Velocity magnitude along the vertical axis of symmetry of the droplet at a volume of 2 μL on the hydrophobic substrate.

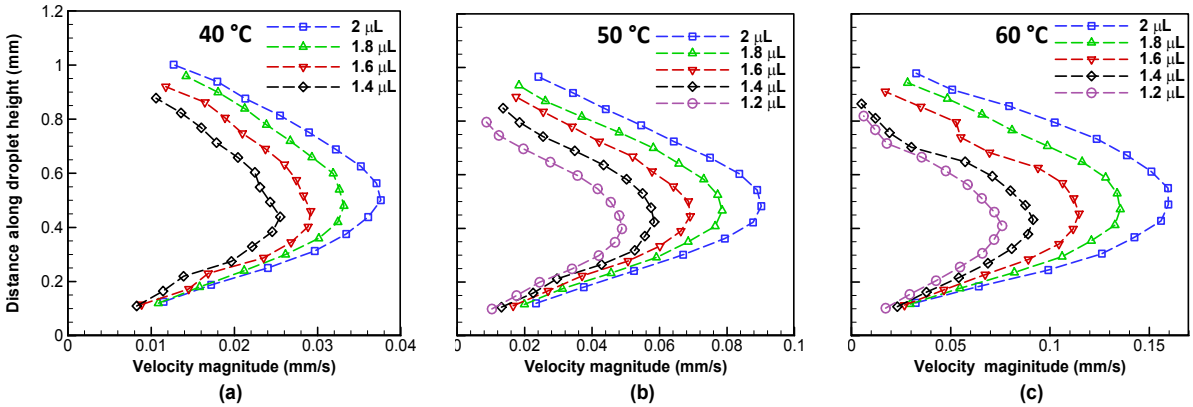

Figure 7.7. Variation of flow velocity on the hydrophobic substrate with changing volume of the evaporating droplet along its vertical axis of symmetry, at substrate temperatures of: (a) 40 °C, (b) 50 °C, and (c) 60 °C.

The contribution of buoyancy to the flow behavior inside the droplet, compared to other potential mechanisms, is assessed in terms of the Rayleigh number. A quantitative determination of Rayleigh number requires an estimation of the temperature drop, ΔT, along the droplet height. To aid in prediction of the temperature field inside an evaporating droplet on a heated substrate, the relative importance of the convective and the diffusive transport inside the droplet may be determined using the Peclet number ($Pe = UL/\alpha$, where U, L, and α represent the characteristic velocity, length scale, and thermal diffusivity of the droplet, respectively). Using the average velocity in the vertical plane of the droplet as the representative flow velocity (U), and the height of the droplet as the length scale, a representative value for Pe corresponding to each different instantaneous droplet volume is determined. Figure 7.8 shows the Peclet number corresponding to different instantaneous droplet volumes and substrate temperatures. The Peclet numbers thus obtained are typically less than 1 for the substrate temperatures considered in the present study. It is therefore appropriate to assume thermal diffusion to be the primary mode of heat transfer in a reduced-order model for the temperature field.

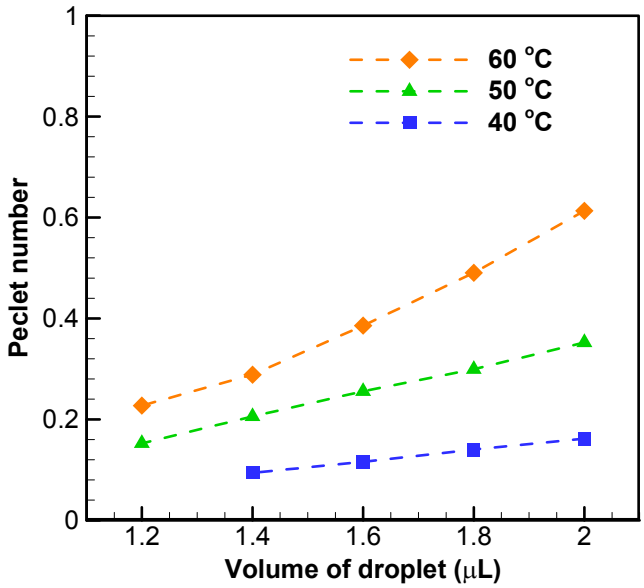

Figure 7.8. Peclet number at different instantaneous droplet volumes corresponding to different surface temperatures for a hydrophobic substrate.

Using the diffusion model, the temperature drops along the droplet height are determined to be 7.1 °C, 11.0 °C, and 15.9 °C, corresponding to respective substrate temperatures of 40 °C, 50 °C, and 60 °C. The thermophysical properties are evaluated at the average temperature of the droplet obtained from the solution of the diffusion-only model. For the experimental conditions, the calculated theoretical value of the Marangoni number suggests that significant thermocapillary convection should take place; however, the experimental observation indicates the dominance of buoyancy-induced convection. The magnitude of velocity inside the droplet is on the order of tens to hundreds of μm/s, as opposed to predicted Marangoni-induced flow velocities on the order of thousands of μm/s [147]. This suppression of Marangoni convection in water droplets is attributed to the large dipole moment of water molecules that attracts contamination on the free surface, and is supported by numerous experimental studies.

Hu and Larson [101] reported that the Marangoni number in water may be suppressed by up to 100 times due to the high sensitivity of water to contamination, as opposed to organic fluids, where theoretical predictions are more readily realized [110,105].

The present study establishes a direct correlation between flow velocity inside droplets evaporating on heated hydrophobic surfaces and the Rayleigh number. Figure 7.9 shows that the maximum velocity inside the droplet, across all experiments, is linearly related to the Rayleigh number. The flow velocity inside the droplet increases with an increase in Rayleigh number and signifies the dominance of buoyancy forces in the recirculating convection pattern observed.

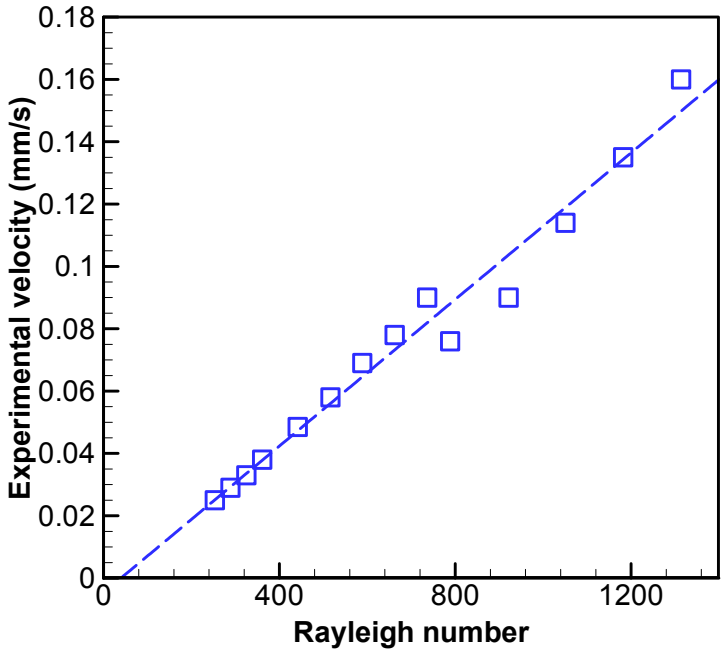

Figure 7.9. Variation of the maximum velocity inside the droplet at different substrate temperatures and volume, with respect to Rayleigh number.

7.2.2 Flow Behavior on a Superhydrophobic Substrate

In the case of a superhydrophobic substrate, an asymmetric vortex, with a solid-body rotation flow pattern is observed (Figure 7.10). This is in stark contrast with the axisymmetric flow pattern observed during droplet evaporation on hydrophobic substrates. Figure 7.10a, and Figure 7.10b show the uncorrected and corrected velocity vectors, respectively, corresponding to a substrate temperature of 50 °C. This flow pattern is consistent across all experiments conducted at the different substrate temperatures. Since the flow is not axisymmetric, the relative orientation of the visualization plane with respect to the axis of the convection roll determines the velocity profile obtained during experiments; all two-dimensional visualizations of central vertical planes presented herein are near-perpendicular to the rolling axis. The horizontal cross-section is visualized at the maximum diameter of the droplet (at y = 0.46 h); the streaklines are shown in Figure 7.2b. The velocity vector plots in Figure 7.11 show that the flow pattern is symmetric along one central vertical plane of symmetry aligned with the direction of flow rotation; the horizontal in-plane velocities are significantly lower compared to the velocity magnitudes in the central vertical plane (Figure 7.10b).

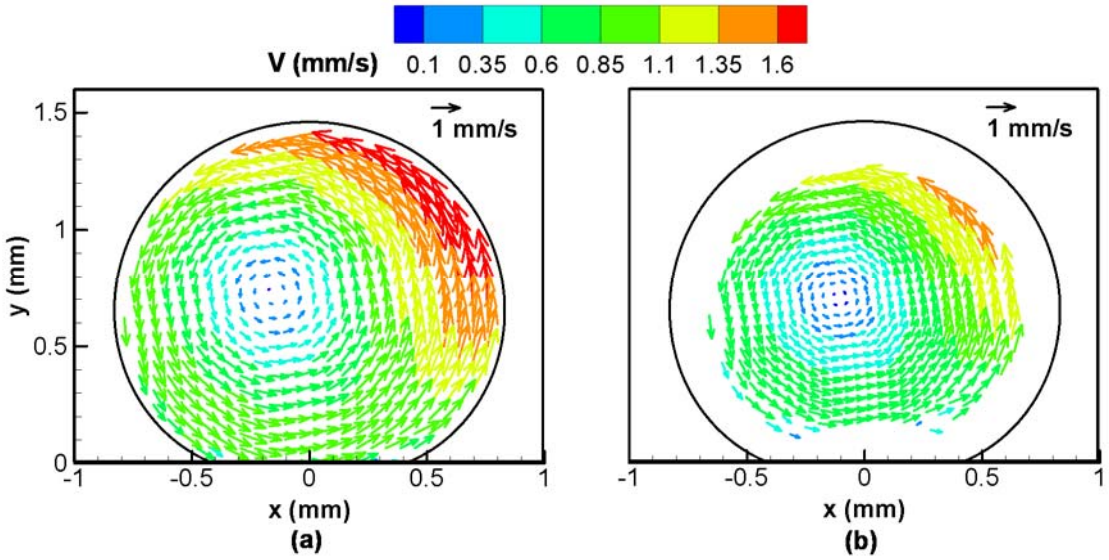

Figure 7.10. Velocity vectors corresponding to a heated superhydrophobic substrate at 50 °C (a) without velocity correction, and (b) with velocity correction, at a droplet instantaneous volume of 2 μL.

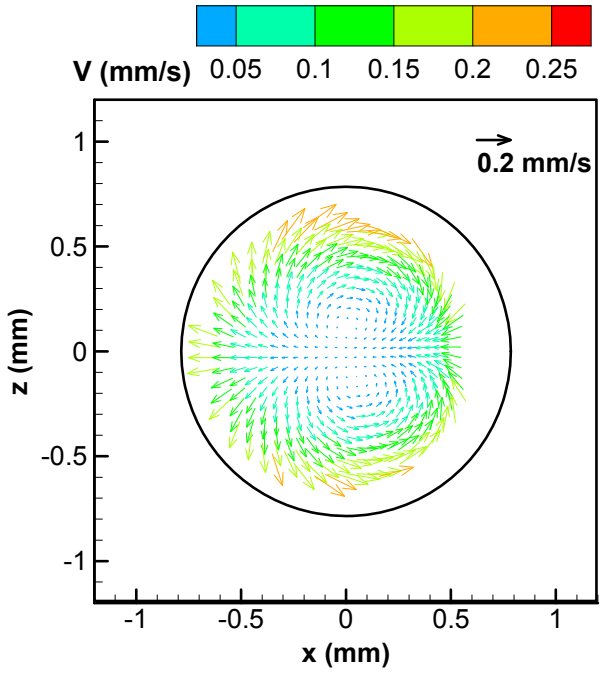

Figure 7.11. Velocity vectors at the horizontal plane of the droplet (at $y = 0.46\ h$) with instantaneous volume ~ 2 µL corresponding to a substrate temperature of 50 °C.

The flow pattern in a water droplet evaporating on a heated hydrophobic surface has been definitively attributed to buoyancy forces caused by the temperature stratification in the droplet based on the observed direct scaling between the measured flow velocity and nondimensional Rayleigh number; as described in the previous section. Surface-tension-induced Marangoni convection is suppressed in water droplets, as is supported by numerous experimental studies [102,105]. The Rayleigh number, which is used to assess the driving buoyancy forces, scales as $\mathrm{Ra} \sim \Delta T\, L^3$, where L and ΔT represent the length scale (height) of the droplet and temperature difference along the droplet height, respectively. The driving buoyancy force increases with an increase in temperature difference, ΔT across the droplet. The temperature differential across the droplet height is expected to be even greater for a superhydrophobic surface due to the longer conduction path between the (smaller) substrate contact area and the interface at the top of the droplet. Therefore, the flow pattern established in a water droplet evaporating on a superhydrophobic surface can also be attributed to buoyant forces. The convection pattern resulting from the Rayleigh-Benard instability in the presence of thermal buoyancy forces is dependent on the geometry of the system and the boundary conditions [154,155].

The single, asymmetric vortex observed in droplets on the superhydrophobic surface is in stark contrast to the axisymmetric fluid motion observed on hydrophilic [102] and hydrophobic substrates. On heated hydrophobic surfaces with a sliding contact line, an axisymmetric toroidal vortex is formed with flow directed upward along the vertical axis of the droplet. The differences in the three-dimensional steady flow pattern in the droplets between the hydrophobic and superhydrophobic cases can be attributed to the

dependence of the primary instability mode of Rayleigh-Benard convection on the geometry of the spherical cap droplet. The threshold for attaining an asymmetric flow state in cylindrical prisms by Rayleigh-Benard convection was previously established experimentally and numerically [154,155,156]. These studies showed that the form of the stable flow structure which emerges due to Rayleigh-Benard convection is dependent on the cylinder aspect ratio (AR = h/D; where h is the height of the cylinder and D is the base diameter) and the Rayleigh number [154,155,156]. For a cylinder heated on end, a nonlinear numerical analysis of convection by Neumann [156] showed that stable axisymmetric solutions are restricted to small Rayleigh numbers. Within this constraint, an axisymmetric toroidal vortex was reported for cylinder aspect ratios less than 0.55 or 0.72 depending on the wall boundary condition [155,156]. For a cylindrical geometry with aspect ratio $\gtrsim 1$, a one-roll mode was reported [154,155,156]. While these specific thresholds apply to flow in cylinders, the convection instability for low Rayleigh number flows inside spherical cap droplets follows a similar behavior; this is supported by experimental results for hydrophobic and superhydrophobic substrates. On the hydrophobic substrate (CA = 110 deg), the lower aspect ratio droplet (h/D = 0.67, where h is the height of the droplet and D is the droplet contact diameter) exhibits a stable axisymmetric flow. Conversely, on the superhydrophobic surface (CA = 150 deg), the higher aspect ratio (h/D = 0.93) leads to a stable single rotating vortex. Furthermore, the flow structure in the horizontal central plane (Figure 7.11) is analogous to the Rayleigh-Benard instability-induced flow field with a one-roll mode observed in the horizontal cross-section of cylindrical geometries with an aspect ratio of ~1 [155]. The finding of an asymmetric convection pattern has particular significance to modeling approaches,

which should not universally assume axisymmetric 2D droplet evaporation behavior. It should be noted that similar asymmetric flow behavior was observed by Chang and Velev [11] for a spherical water droplet evaporating to ambient while floating on the surface of an oil bath.

The maximum velocity in the droplet evaporating on the superhydrophobic surface is on the order of 1000 μm/s. This flow velocity is an order of magnitude higher than the flow velocity in a droplet evaporating on a hydrophobic substrate, which is on the order of 100 μm/s. It is important to note that the magnitude of evaporation-induced velocity is higher in the case of the superhydrophobic surface compared to the hydrophobic surface despite the fact that the overall rate of evaporation is lower [143]. The high recirculation velocity in the former case can be related to the higher magnitude of Rayleigh number and the difference in the nature of the vortex structure in the case of a superhydrophobic substrate as compared to a hydrophobic substrate. The higher contact angle of a droplet on a superhydrophobic surface results in a larger height (length scale) and ΔT ($=T_{sub} - T_{interface}$) due to evaporative cooling across the droplet. The velocity magnitude inside the droplet increases with increase in substrate temperature (Figure 7.12). The rate of evaporation increases with substrate temperature, thereby increasing the extent of evaporative cooling and resulting temperature difference, ΔT, across the droplet.

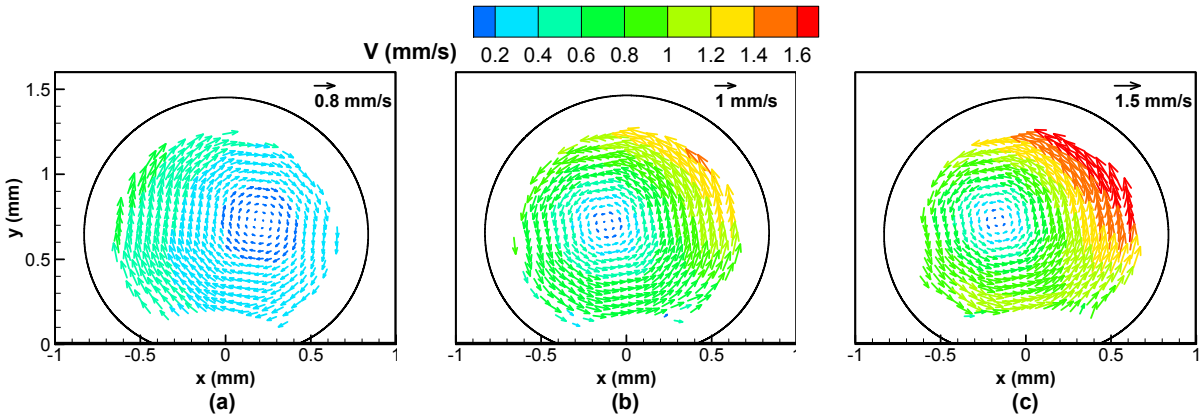

Figure 7.12. Velocity vectors in the central vertical plane of the evaporating droplet corresponding to superhydrophobic substrate temperature of (a) 40 °C (b) 50 °C, and (c) 60 °C.

The experiments reveal a consistent vertical distance of the vortex center above the substrate in all cases. When viewing along the rolling axis, it is observed that irrespective of the substrate temperature, the vortex center lies at a vertical height of 0.72 ± 0.02 mm from the base of the droplet for a 2 μL droplet. This corresponds to a nondimensional height, y/h = 0.496 ± 0.015. In the case of a droplet evaporating on a hydrophobic surface, the nondimensional height of the maximum velocity location, corresponding to the center of the toroidal convection pattern was observed at a nondimensional height, $y/h \approx 0.4$. This position remained unchanged for different instantaneous droplet volumes and surface temperatures. The physical characteristics of the vortex structures in droplets on the hydrophobic and superhydrophobic substrates show that the vortex center of the flow pattern is constant for a given surface wettability.

The recirculating flow pattern that develops inside a droplet evaporating on a superhydrophobic surface can be exploited in microfluidic devices to achieve efficient mixing in microliter-sized droplets. Under species-diffusion-dominated conditions, the

time required to homogenize the solution is dependent on the diffusion time scale, $\tau_d = r^2/D$, where r is the radius of the drop, and D is the diffusion coefficient. For a fluorescent dye (Rhodamine 6G; diffusion coefficient in water = 4.14 x 10^{-10} m^2/s [157]) mixing into a water droplet of volume ~2 μL, the diffusion time scale is ~24 min. The time scale for mixing due to evaporative recirculation motion inside the droplet can be estimated as $\tau_{circ} = n\left(2\pi/\omega\right)$ where ω is the angular velocity of the flow pattern and n is the number of rotations required for mixing. The angular velocity inside the droplet evaporating on a superhydrophobic surface increases with an increase in substrate temperature; ω = 0.75 ± 0.10 s^{-1}, 1.71 ± 0.28 s^{-1}, 2.21 ± 0.33 s^{-1} corresponding to T_{sub} = 40 °C, 50 °C, and 60 °C, respectively. The corresponding mixing time scales reduces with this increase in the angular velocity, and should be on the order of seconds, depending on the number rotations are required for mixing. The Peclet number for mass transport, given by $Pe = UL/D$, is ~3260 for a 2 μL droplet on a superhydrophobic surface. The high Peclet number signifies the dominance of the evaporative convection flow for mass transport or mixing within the droplet.

The reduction in mixing on the superhydrophobic substrate with increase in substrate temperature is demonstrated by proof-of-concept mixing experiments using fluorescent dye Rhodamine 6G (Figure 7.13). The droplet volume used in the mixing experiments is ~10 μL for easier visualization. The evaporative flow field inside the droplet undergoes multiple rotations (on the order of ten) to realize complete mixing within the droplet. On the superhydrophobic substrate, the mixing time reduces by a factor of 8 from ~9.7 s at 40 °C to ~1.2 s at 60 °C. This convection-aided mixing time is two to three orders of

magnitude less than the species-diffusion mixing time scale (~72 min for a 10 μL droplet), as anticipated from the scaling analysis which was based on velocity measurements in 2 μL droplets. At a fixed substrate temperature of 60 °C, the mixing time is reduced by ~15 times during droplet evaporation on the superhydrophobic substrate compared to the hydrophobic substrate (Figure 7.13). Since the rate of evaporation of water droplets on superhydrophobic surfaces is low [143], efficient mixing can be obtained without much loss of mass within a short time period.

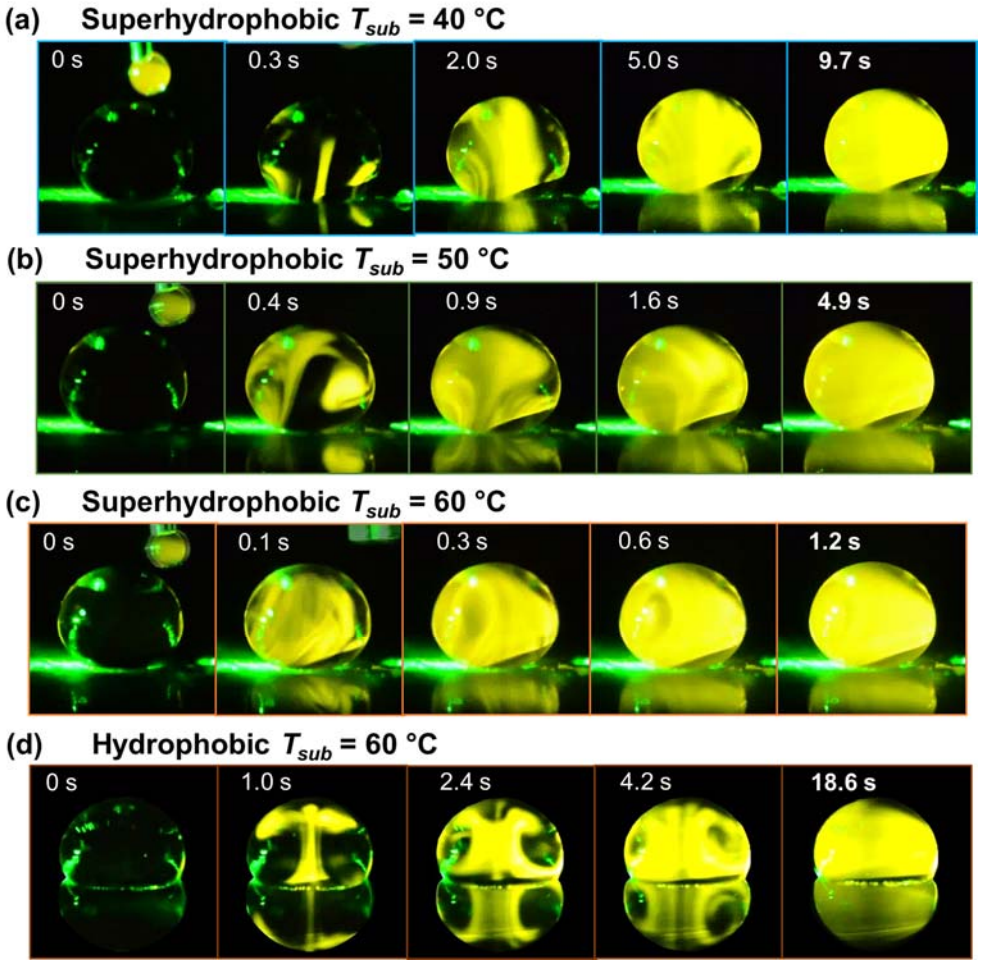

Figure 7.13. Time series images showing dye mixing in an evaporating droplet on a superhydrophobic substrate maintained at (a) 40 °C (b) 50 °C (c) 60 °C, and on (d) hydrophobic substrate maintained at 60 °C.

The flow behavior inside the droplet during evaporation on a superhydrophobic surface in conjunction with the sliding droplet contact line may be related to the evaporative deposition of particulate inclusions on such surfaces. The high internal flow velocity impedes the deposition of particulates on the substrate. The particulates remain suspended due to the bulk fluid motion within the droplet. During the final stages of evaporation, when the droplet contact angle reduces and the contact line becomes pinned, the particles are more prone to adhering to the substrate. This occurs in the mixed mode of evaporation, which occurs in the last 0.5 % of the evaporation time [116,143]. The final deposition area on superhydrophobic substrates with sliding contact line is therefore less than the footprint area of the droplet at onset of the mixed mode of evaporation [116].

7.3 Summary

The internal flow field of a droplet evaporating on a heated hydrophobic, and superhydrophobic surfaces is experimentally mapped. Particle Image Velocimetry is used to quantitatively determine the flow velocity inside the droplet. In the case of hydrophobic substrates, the presence of an axisymmetric, toroidal vortex structure with flow directed upwards along the vertical axis indicates a buoyancy-induced flow. This mechanism, along with the sliding contact line during evaporation, explains the localized deposition of particles previously observed on hydrophobic substrates. The representative flow velocity is shown to directly correspond to the thermal Rayleigh number, confirming that buoyancy-induced flow dominates.

On superhydrophobic substrates, asymmetric buoyancy driven evaporative flow pattern observed. The flow field is attributed to the high aspect ratio of droplets evaporating on superhydrophobic surfaces. The flow velocity is an order of magnitude

higher than that observed in the case of axisymmetric flow in a droplet evaporating on hydrophobic substrate. This illustrates the applicability of droplet evaporation on superhydrophobic surfaces for achieving efficient droplet mixing for microfluidics applications. The mixing rates are enhanced by increasing the substrate temperatures. The high flow velocity combined with a sliding contact line results in localized evaporative deposition on superhydrophobic surfaces.

CHAPTER 8. CONCLUSIONS AND FUTURE WORK

The primary outcome of the present doctoral thesis is a better understanding of the interdependence between surface morphology and interfacial interaction mechanism. The research work enabled a physics-based understanding of the droplet dynamics on smooth hydrophobic, and superhydrophobic surfaces under external electrical actuation, dynamic impact, and during evaporation. This chapter summarizes the key research outcomes of the present dissertation, and subsequently a few avenues of future research are proposed

8.1 Conclusions

The findings of the present work are as listed below:

In Chapter 3, the transient response of a droplet to step actuation, and time varying actuation during electrowetting is determined. The findings are important in applications such as electrowetting-based lens, and switch, which rely upon electrical actuation.

a. Irrespective of the applied step voltage, a droplet of a particular volume takes a characteristic time for attaining the maximum electrowetted radius. This characteristic time scale is proposed to be dependent on the radius, density, and surface tension of the droplet.

b. Analysis of the droplet dynamics in terms of the transient contact angle, and contact radius of the droplet, during time-varying actuation of a liquid droplet is used to identify the shape oscillation modes of the droplet during electrowetting with an alternating in-phase and out-of-phase behavior between contact angle and contact radius.
c. Sub-harmonic oscillation behavior is identified and explained in terms of the parametric excitation force acting on the droplet during electrowetting.

Chapter 4 includes a single-step fabrication technique for hierarchical superhydrophobic surfaces. A comparison between the characteristics of the hierarchical surface, and single-roughness surfaces shows a significant improvement in the characteristics of the former in terms of the contact angle hysteresis, roll-off angle, and robustness under dynamic impact conditions.

In Chapter 5, novel hybrid superhydrophobic surfaces, incorporating a combination of communicating and non-communicating air gaps, are designed and fabricated. Pressure-based analysis during droplet impingement experiments enables a better understanding of the Cassie-Wenzel transition mechanism.

a. The hybrid superhydrophobic surfaces increase the anti-wetting capillary pressure while retaining a high contact angle at the single roughness level.
b. The water hammer pressure acting during droplet impact is discovered to be dependent on the surface morphology, and significantly lower on superhydrophobic surfaces compared to flat surfaces.

In Chapter 6, evaporation characteristics of sessile droplets on unheated and heated hydrophobic and superhydrophobic surfaces are studied. The research work enabled

understanding of the dependence of the transport mechanisms affecting droplet evaporation on the droplet shape which is in turn dependent on the surface characteristics.

a. Evaporation on unheated and heated hydrophobic and superhydrophobic surfaces with minimal contact angle hysteresis follows a constant contact angle mode during evaporation.
b. A comparison with the vapor-diffusion model shows that although there is a good match between rate of evaporation obtained experimentally and the vapor-diffusion model for hydrophobic surfaces, there is a significant mismatch in the case of superhydrophobic surfaces. The deviation increases with increase in substrate temperature. The suppression in evaporation rate is attributed to the evaporative cooling across the droplet interface.
c. A simple model is developed to determine the interfacial temperature profile of a droplet during evaporation, taking into account thermal conduction through the droplet.
d. A generalized relationship between instantaneous volume of droplets and nondimensional time for droplets with contact angle greater than 90 deg under unheated conditions is proposed.

Chapter 7 includes visualization and analysis of evaporation-induced convection in droplets on hydrophobic and superhydrophobic surfaces. Particle Image Velocimetry, and a subsequent image correction algorithm to account for the lens effect of the droplet are used to quantitatively determine the flow velocity inside the droplet.

a. The presence of an axisymmetric, toroidal vortex structure with flow directed upwards along the vertical axis indicates a thermal buoyancy induced flow in a water droplet evaporating on a hydrophobic surface.
b. The flow structure, along with the sliding contact line, are proposed to be responsible for localized particle deposition on hydrophobic surface.
c. In the case of superhydrophobic surfaces, the convection is manifested as a single rotating vortex structure, analogous to the solid body rotation. The flow structure is attributed to the height to diameter aspect ratio of droplet on superhydrophobic surfaces.
d. The convection flow velocity inside droplets evaporating on superhydrophobic surface is determined to on the order of 1000 μm/s, which is an order of magnitude higher than on hydrophobic surfaces. The applicability of the recirculating flow in mixing applications in lab-on-chip devices is proposed.

8.2 Suggested Future Work

8.2.1 Wetting based Manipulation of Solute in an Evaporating Droplet

The work presented in this thesis demonstrates that evaporation-induced convection inside a droplet is dependent on the substrate properties. Droplet evaporation on a hydrophilic surface results in peripheral deposition. On the other hand, hydrophobic and superhydrophobic surfaces that are characterized by a low contact angle hysteresis are demonstrated to localize particulate deposition during evaporation. The work presented in this thesis has highlighted the importance of the nature of substrate and the accompanying convective flow on the evaporative deposition characteristics. The

dependence of the flow characteristics on surface wettability can be exploited to manipulate the evaporative deposition by implementing surfaces with differential wettability. The idea is to fabricate a hybrid superhydrophobic surface with specific hydrophilic areas for solute transport to a desired location by selective pinning of contact line and by means of convective control inside the droplet. The device for localized evaporative deposition can also implement substrate heating so as to minimize the total process time.

8.2.2 Efficient Mixing using Evaporation-induced Convection

Efficient mixing of small amounts of liquids is of extreme importance in microfluidics application. However, in small length scales, the viscous effects are dominant which makes mixing challenging. In lab-on-chip devices, the rate of chemical reactions is often limited by the mass diffusion. Different mixing mechanisms include flow past patterned features, magnetic stirrers, electrowetting, and acoustic waves. Obtaining on-the-spot mixing in static droplets is even more challenging. Recently, electrowetting-induced oscillation based internal convection inside droplet has been reported to enhance mixing inside droplets. Our work, as a part of this thesis, has revealed the significant magnitude of the evaporation-induced convection velocity inside droplets evaporating on superhydrophobic surfaces. The evaporation-induced flow velocity increases with increase in substrate temperature. One possible avenue for future work is to implement this evaporation-induced convection in microfluidics devices to obtain ‘on-spot’ and ‘on-the-go’ mixing. Superhydrophobic surfaces are characterized by a very low contact angle hysteresis and a low roll off angle. The idea is to implement this property to move droplets in microchannels with heated bottom wall so that both

transport and mixing of droplets can be attained simultaneously. The flow field inside the droplet undergoing simultaneous evaporation and rolling should be studied for this application.

LIST OF REFERENCES

LIST OF REFERENCES

[1] Mugele, F., and Baret, J. C., 2005, "Electrowetting: from basics to applications," J. Phys. Condens. Matter, **17**, p. R705.

[2] Koch, K., Bhushan, B., Jung, Y. C., and Barthlott, W., 2009, "Fabrication of artificial Lotus leaves and significance of hierarchical structure for superhydrophobicity and low adhesion," Soft Matter, **5**(7), pp. 1386–1393.

[3] Neinhuis, C., and Barthlott, W., 1997, "Characterization and distribution of water-repellent, self-cleaning plant surfaces," Ann. Bot., **79**(6), p. 667.

[4] He, B., Patankar, N. A., and Lee, J., 2003, "Multiple equilibrium droplet shapes and design criterion for rough hydrophobic surfaces," Langmuir, **19**(12), pp. 4999–5003.

[5] Lee, J., He, B., and Patankar, N. A., 2005, "A roughness-based wettability switching membrane device for hydrophobic surfaces," J. Micromechanics Microengineering, **15**, p. 591.

[6] Choi, C. H., Ulmanella, U., Kim, J., Ho, C. M., and Kim, C. J., 2006, "Effective slip and friction reduction in nanograted superhydrophobic microchannels," Phys. Fluids, **18**, p. 087105.

[7] Calvert, P., 2001, "Inkjet printing for materials and devices," Chem. Mater., **13**(10), pp. 3299–3305.

[8] Kumari, N., and Garimella, S. V., 2011, "Characterization of the heat transfer accompanying electrowetting or gravity-induced droplet motion," Int. J. Heat Mass Transf., **54**(17-18), pp. 4037–4050.

[9] Dhavaleswarapu, H. K., Migliaccio, C. P., Garimella, S. V., and Murthy, J. Y., 2009, "Experimental investigation of evaporation from low-contact-angle sessile droplets," Langmuir, **26**(2), pp. 880–888.

[10] Li, Q., Zhu, Y. T., Kinloch, I. A., and Windle, A. H., 2006, "Self-organization of carbon nanotubes in evaporating droplets," J. Phys. Chem. B, **110**(28), pp. 13926–13930.

[11] Chang, S. T., and Velev, O. D., 2006, "Evaporation-induced particle microseparations inside droplets floating on a chip," Langmuir, **22**(4), pp. 1459–1468.

[12] Deegan, R. D., Bakajin, O., Dupont, T. F., Huber, G., Nagel, S. R., and Witten, T. A., 2000, "Contact line deposits in an evaporating drop," Phys. Rev. E, **62**(1), pp. 756–765.

[13] Popov, Y. O., 2005, "Evaporative deposition patterns: spatial dimensions of the deposit," Phys. Rev. E, **71**(3), p. 036313.

[14] Jing, J., Reed, J., Huang, J., Hu, X., Clarke, V., Edington, J., Housman, D., Anantharaman, T. S., Huff, E. J., and Mishra, B., 1998, "Automated high resolution optical mapping using arrayed, fluid-fixed DNA molecules," Proc. Natl. Acad. Sci., **95**(14), p. 8046.

[15] Wu, A., Yu, L., Li, Z., Yang, H., and Wang, E., 2004, "Atomic force microscope investigation of large-circle DNA molecules," Anal. Biochem., **325**(2), pp. 293–300.

[16] Birdi, K. S., and Vu, D. T., 1993, "Wettability and the evaporation rates of fluids from solid surfaces," J. Adhes. Sci. Technol., **7**(6), pp. 485–493.

[17] Kulinich, S. A., and Farzaneh, M., 2009, "Effect of contact angle hysteresis on water droplet evaporation from super-hydrophobic surfaces," Appl. Surf. Sci., **255**(7), pp. 4056–4060.

[18] Anantharaju, N., Panchagnula, M., and Neti, S., 2009, "Evaporating drops on patterned surfaces: Transition from pinned to moving triple line," J. Colloid Interface Sci., **337**(1), pp. 176–182.

[19] Angelis, F. D., Gentile, F., Mecarini, F., Das, G., Moretti, M., Candeloro, P., Coluccio, M. L., Cojoc, G., Accardo, A., Liberale, C., Zaccaria, R. P., Perozziello, G., Tirinato, L., Toma, A., Cuda, G., Cingolani, R., and Fabrizio, E. D., 2011,

"Breaking the diffusion limit with super-hydrophobic delivery of molecules to plasmonic nanofocusing SERS structures," Nat. Photonics, **5**(11), pp. 682–687.

[20] Rakers, S., Chi, L. F., and Fuchs, H., 1997, "Influence of the Evaporation Rate on the Packing Order of Polydisperse Latex Monofilms," Langmuir, **13**(26), pp. 7121–7124.

[21] Park, J., and Moon, J., 2006, "Control of Colloidal Particle Deposit Patterns within Picoliter Droplets Ejected by Ink-Jet Printing," Langmuir, **22**(8), pp. 3506–3513.

[22] Whitesides, G. M., and Grzybowski, B., 2002, "Self-Assembly at All Scales," Science, **295**(5564), pp. 2418–2421.

[23] Maeki, M., Yamaguchi, H., Yamashita, K., Nakamura, H., Miyazaki, M., and Maeda, H., 2012, "A method for generating single crystals that rely on internal fluid dynamics of microdroplets," Chem. Commun., **48**(41), p. 5037.

[24] Wen, J. T., Ho, C.-M., and Lillehoj, P. B., 2013, "Coffee Ring Aptasensor for Rapid Protein Detection," Langmuir, **29**(26), pp. 8440–8446.

[25] Nahmias, Y., Schwartz, R. E., Verfaillie, C. M., and Odde, D. J., 2005, "Laser-guided direct writing for three-dimensional tissue engineering," Biotechnol. Bioeng., **92**(2), pp. 129–136.

[26] Cho, S. K., Moon, H., and Kim, C. J., 2003, "Creating, transporting, cutting, and merging liquid droplets by electrowetting-based actuation for digital microfluidic circuits," J. Microelectromechanical Syst., **12**(1), pp. 70–80.

[27] Pollack, M. G., Shenderov, A. D., and Fair, R. B., 2002, "Electrowetting-based actuation of droplets for integrated microfluidics," Lab Chip, **2**, pp. 96–101.

[28] Chatterjee, D., Hetayothin, B., Wheeler, A. R., King, D. J., and Garrell, R. L., 2006, "Droplet-based microfluidics with nonaqueous solvents and solutions," Lab Chip, **6**(2), pp. 199–206.

[29] Kumari, N., Bahadur, V., and Garimella, S. V., 2008, "Electrical actuation of dielectric droplets," J. Micromechanics Microengineering, **18**, p. 085018.

[30] Kumari, N., Bahadur, V., and Garimella, S. V., 2008, "Electrical actuation of electrically conducting and insulating droplets using ac and dc voltages," J. Micromechanics Microengineering, **18**, p. 105015.

[31] Kuiper, S., and Hendriks, B. H. W., 2004, "Variable-focus liquid lens for miniature cameras," Appl. Phys. Lett., **85**, p. 1128.

[32] Hayes, R. A., and Feenstra, B. J., 2003, "Video-speed electronic paper based on electrowetting," Nature, **425**(6956), pp. 383–385.

[33] Herbertson, D. L., Evans, C. R., Shirtcliffe, N. J., McHale, G., and Newton, M. I., 2006, "Electrowetting on superhydrophobic SU-8 patterned surfaces," Sens. Actuators Phys., **130**, pp. 189–193.

[34] Bahadur, V., and Garimella, S. V., 2007, "Electrowetting-based control of static droplet states on rough surfaces," Langmuir, **23**(9), pp. 4918–4924.

[35] Bahadur, V., and Garimella, S. V., 2008, "Electrowetting-based control of droplet transition and morphology on artificially microstructured surfaces," Langmuir, **24**(15), pp. 8338–8345.

[36] Shapiro, B., Moon, H., Garrell, R., and Kim, C., 2003, "Equilibrium behavior of sessile drops under surface tension, applied external fields, and material variations," J. Appl. Phys., **93**(9), pp. 5794–5811.

[37] Vallet, M., Vallade, M., and Berge, B., 1999, "Limiting phenomena for the spreading of water on polymer films by electrowetting," Eur. Phys. J. B - Condens. Matter Complex Syst., **11**, pp. 583–591.

[38] Roques-Carmes, T., Hayes, R. A., and Schlangen, L. J. M., 2004, "A physical model describing the electro-optic behavior of switchable optical elements based on electrowetting," J. Appl. Phys., **96**, p. 6267.

[39] Oh, J. M., Ko, S. H., and Kang, K. H., 2010, "Analysis of electrowetting-driven spreading of a drop in air," Phys. Fluids, **22**, p. 032002.

[40] Sen, P., and Kim, C., 2009, "Capillary Spreading Dynamics of Electrowetted Sessile Droplets in Air," Langmuir, **25**(8), pp. 4302–4305.

[41] Cooney, C. G., Chen, C. Y., Emerling, M. R., Nadim, A., and Sterling, J. D., 2006, "Electrowetting droplet microfluidics on a single planar surface," Microfluid. Nanofluidics, **2**(5), pp. 435–446.

[42] Kumar, A., Pluntke, M., Cross, B., Baret, J. C., and Mugele, F., 2006, "Finite conductivity effects and apparent contact angle saturation in AC electrowetting," Mater. Res. Soc. Symp. Proc, pp. 0899–N06–01.

[43] Jones, T. B., 2001, "Liquid dielectrophoresis on the microscale," J. Electrost., **51**, pp. 290–299.

[44] Berge, B., and Peseux, J., 2000, "Variable focal lens controlled by an external voltage: an application of electrowetting," Eur. Phys. J. E Soft Matter Biol. Phys., **3**(2), pp. 159–163.

[45] Mugele, F., Staicu, A., Bakker, R., and van den Ende, D., 2011, "Capillary Stokes drift: a new driving mechanism for mixing in AC-electrowetting," Lab. Chip, **11**(12), p. 2011.

[46] Paik, P., Pamula, V. K., and Fair, R. B., 2003, "Rapid droplet mixers for digital microfluidic systems," Lab. Chip, **3**(4), pp. 253–259.

[47] Miraghaie, R., Sterling, J. D., and Nadim, A., 2006, "Shape Oscillation and Internal Mixing in Sessile Liquid Drops using ElectroWetting-On-Dielectric (EWOD)," Technical Proceedings of the 2006 NSTI Nanotechnology Conference and Trade Show, pp. 610–613.

[48] Mugele, F., Baret, J. C., and Steinhauser, D., 2009, "Microfluidic mixing through electrowetting-induced droplet oscillations," Appl. Phys. Lett., **88**(20), p. 204106.

[49] Ko, S. H., Lee, H., and Kang, K. H., 2008, "Hydrodynamic flows in electrowetting," Langmuir, **24**(3), pp. 1094–1101.

[50] Blossey, R., 2003, "Self-cleaning surfaces-virtual realities," Nat. Mater., **2**(5), pp. 301–306.

[51] Fair, R. B., 2007, "Digital microfluidics: is a true lab-on-a-chip possible?," Microfluid. Nanofluidics, **3**(3), pp. 245–281.

[52] Nosonovsky, M., and Bhushan, B., 2009, "Superhydrophobic surfaces and emerging applications: non-adhesion, energy, green engineering," Curr. Opin. Colloid Interface Sci., **14**(4), pp. 270–280.

[53] Gulrajania, M. L., and Gupta, D., 2011, "Emerging techniques for functional finishing of textiles," Indian J. Fibre Text. Res., **36**, pp. 388–397.

[54] Mishchenko, L., Hatton, B., Bahadur, V., Taylor, J. A., Krupenkin, T., and Aizenberg, J., 2010, "Design of ice-free nanostructured surfaces based on repulsion of impacting water droplets," ACS Nano., 4, pp. 7699-7707.

[55] Chen, T. H., Chuang, Y. J., Chieng, C. C., and Tseng, F. G., 2007, "A wettability switchable surface by microscale surface morphology change," J. Micromechanics Microengineering, **17**, p. 489.

[56] Krupenkin, T. N., Taylor, J. A., Wang, E. N., Kolodner, P., Hodes, M., and Salamon, T. R., 2007, "Reversible wetting-dewetting transitions on electrically tunable superhydrophobic nanostructured surfaces," Langmuir, **23**(18), pp. 9128–9133.

[57] Bahadur, V., and Garimella, S. V., 2010, "Electrical actuation-induced droplet transport on smooth and superhydrophobic surfaces," Int. J. Micro-Nano Scale Transp., **1**(1), pp. 1–26.

[58] Bartolo, D., Bouamrirene, F., Verneuil, E., Buguin, A., Silberzan, P., and Moulinet, S., 2006, "Bouncing or sticky droplets: impalement transitions on superhydrophobic micropatterned surfaces," EPL Europhys. Lett., **74**, p. 299.

[59] Bhushan, B., Koch, K., and Jung, Y. C., 2009, "Fabrication and characterization of the hierarchical structure for superhydrophobicity and self-cleaning," Ultramicroscopy, **109**(8), pp. 1029–1034.

[60] Ma, M., and Hill, R. M., 2006, "Superhydrophobic surfaces," Curr. Opin. Colloid Interface Sci., **11**(4), pp. 193–202.

[61] Verplanck, N., Coffinier, Y., Thomy, V., and Boukherroub, R., 2007, "Wettability switching techniques on superhydrophobic surfaces," Nanoscale Res. Lett., **2**(12), pp. 577–596.

[62] Chen, L., Xiao, Z., Chan, P. C. ., and Lee, Y. K., 2010, "Static and dynamic characterization of robust superhydrophobic surfaces built from nano-flowers on silicon micro-post arrays," J. Micromechanics Microengineering, **20**, p. 105001.

[63] Deng, T., Varanasi, K. K., Hsu, M., Bhate, N., Keimel, C., Stein, J., and Blohm, M., 2009, "Nonwetting of impinging droplets on textured surfaces," Appl. Phys. Lett., **94**, p. 133109.

[64] Jung, Y. C., and Bhushan, B., 2009, "Dynamic effects induced transition of droplets on biomimetic superhydrophobic surfaces," Langmuir, **25**(16), pp. 9208–9218.

[65] Wier, K. A., and McCarthy, T. J., 2006, "Condensation on ultrahydrophobic surfaces and its effect on droplet mobility: Ultrahydrophobic surfaces are not always water repellant," Langmuir, **22**(6), pp. 2433–2436.

[66] Boreyko, J. B., and Chen, C. H., 2009, "Self-propelled dropwise condensate on superhydrophobic surfaces," Phys. Rev. Lett., **103**(18), p. 184501.

[67] Ming, W., Wu, D., and Van Benthem, R., 2005, "Superhydrophobic films from raspberry-like particles," Nano Lett, **5**(11), pp. 2298–2301.

[68] Northen, M. T., and Turner, K. L., 2005, "A batch fabricated biomimetic dry adhesive," Nanotechnology, **16**, p. 1159.

[69] Torkelli, A., 2003, "Droplet microfluidics on a planar surface," PhD Thesis, Department of Electrical Engineering, Helsinki University of Technology, Espoo, Finland.

[70] Kwon, Y., Patankar, N., Choi, J., and Lee, J., 2009, "Design of surface hierarchy for extreme hydrophobicity," Langmuir, **25**(11), pp. 6129–6136.

[71] Dash, S., Kumari, N., and Garimella, S. V., 2011, "Characterization of ultrahydrophobic hierarchical surfaces fabricated using a single-step fabrication methodology," J. Micromechanics Microengineering, **21**, p. 105012.

[72] Patankar, N. A., 2010, "Consolidation of hydrophobic transition criteria by using an approximate energy minimization approach," Langmuir, **26**(11), pp. 8941–8945.

[73] Park, Y. B., Im, M., Im, H., and Choi, Y. K., 2010, "Superhydrophobic cylindrical nanoshell array," Langmuir, **26**(11), pp. 7661–7664.

[74] Bahadur, V., and Garimella, S. V., 2009, "Preventing the Cassie- Wenzel Transition Using Surfaces with Noncommunicating Roughness Elements," Langmuir, **25**(8), pp. 4815–4820.

[75] Wang, Z., Lopez, C., Hirsa, A., and Koratkar, N., 2007, "Impact dynamics and rebound of water droplets on superhydrophobic carbon nanotube arrays," Appl. Phys. Lett., **91**, p. 023105.

[76] Bergeron, V., and Quéré, D., 2001, "Water droplets make an impact," Phys. World May, pp. 27–31.

[77] Malouin Jr, B. A., Koratkar, N. A., Hirsa, A. H., and Wang, Z., 2010, "Directed rebounding of droplets by microscale surface roughness gradients," Appl. Phys. Lett., **96**, p. 234103.

[78] Richard, D., and Quéré, D., 2000, "Bouncing water drops," EPL Europhys. Lett., **50**, p. 769.

[79] Cook, S. S., 1928, "Erosion by water-hammer," Proc. R. Soc. Lond. Ser. A, **119**(783), p. 481.

[80] Engel, O. G., 1955, "Waterdrop collisions with solid surfaces," J Res NBS, **5**, pp. 281–298.

[81] Dear, J. P., and Field, J. E., 1988, "A study of the collapse of arrays of cavities," J. Fluid Mech., **190**(1), pp. 409–425.

[82] Picknett, R. G., and Bexon, R., 1977, "The evaporation of sessile or pendant drops in still air," J. Colloid Interface Sci., **61**(2), pp. 336–350.

[83] McHale, G., Rowan, S. M., Newton, M. I., and Banerjee, M. K., 1998, "Evaporation and the Wetting of a Low-Energy Solid Surface," J Phys Chem B, **102**(11), pp. 1964–1967.

[84] Yu, Y. S., Wang, Z., and Zhao, Y. P., 2011, "Experimental and theoretical investigations of evaporation of sessile water droplet on hydrophobic surfaces," J. Colloid Interface Sci., **365**(1), pp. 254–259.

[85] David, S., Sefiane, K., and Tadrist, L., 2007, "Experimental investigation of the effect of thermal properties of the substrate in the wetting and evaporation of sessile drops," Colloids Surf. Physicochem. Eng. Asp., **298**(1), pp. 108–114.

[86] Dunn, G. J., Wilson, S. K., Duffy, B. R., David, S., and Sefiane, K., 2009, "The strong influence of substrate conductivity on droplet evaporation," J. Fluid Mech., **623**, pp. 329–351.

[87] Hu, H., and Larson, R. G., 2002, "Evaporation of a sessile droplet on a substrate," J. Phys. Chem. B, **106**(6), pp. 1334–1344.

[88] Deegan, R. D., Bakajin, O., Dupont, T. F., Huber, G., Nagel, S. R., and Witten, T. A., 1997, "Capillary flow as the cause of ring stains from dried liquid drops," Nature, **389**(6653), pp. 827–828.

[89] Ollesch, J., Drees, S. L., Heise, H. M., Behrens, T., Brüning, T., and Gerwert, K., 2013, "FTIR spectroscopy of biofluids revisited: an automated approach to spectral biomarker identification," The Analyst, **138**(14), p. 4092.

[90] Tekin, E., Smith, P. J., and Schubert, U. S., 2008, "Inkjet printing as a deposition and patterning tool for polymers and inorganic particles," Soft Matter, **4**(4), p. 703.

[91] Eral, H. B., Augustine, D. M., Duits, M. H. G., and Mugele, F., 2011, "Suppressing the coffee stain effect: how to control colloidal self-assembly in evaporating drops using electrowetting," Soft Matter, **7**(10), pp. 4954–4958.

[92] McHale, G., Aqil, S., Shirtcliffe, N. J., Newton, M. I., and Erbil, H. Y., 2005, "Analysis of droplet evaporation on a superhydrophobic surface," Langmuir, **21**(24), pp. 11053–11060.

[93] Erbil, H. Y., McHale, G., and Newton, M. I., 2002, "Drop evaporation on solid surfaces: Constant Contact Angle Mode," Langmuir, **18**(7), pp. 2636–2641.

[94] Shanahan, M. E. R., Sefiane, K., and Moffat, J. R., 2011, "Dependence of volatile droplet lifetime on the hydrophobicity of the substrate," Langmuir, **27**(8), pp. 4572–4577.

[95] Zhang, X., Tan, S., Zhao, N., Guo, X., Zhang, X., Zhang, Y., and Xu, J., 2006, "Evaporation of sessile water droplets on superhydrophobic natural lotus and biomimetic polymer surfaces," ChemPhysChem, **7**(10), pp. 2067–2070.

[96] Nguyen, T. A. ., Nguyen, A. V., Hampton, M. A., Xu, Z. P., Huang, L., and Rudolph, V., 2011, "Theoretical and experimental analysis of droplet evaporation on solid surfaces," Chem. Eng. Sci., **69**(1), pp. 522–529.

[97] Sobac, B., and Brutin, D., 2012, "Thermal effects of the substrate on water droplet evaporation," Phys. Rev. E, **86**(2), p. 021602.

[98] Gelderblom, H., Marin, A. G., Nair, H., van Houselt, A., Lefferts, L., Snoeijer, J. H., and Lohse, D., 2011, "How water droplets evaporate on a superhydrophobic substrate," Phys. Rev. E, **83**(2), p. 026306.

[99] Erbil, H. Y., 2012, "Evaporation of pure liquid sessile and spherical suspended drops: A review," Adv. Colloid Interface Sci., **170**(1), pp. 67–86.

[100] Ressine, A., Finnskog, D., Marko-Varga, G., and Laurell, T., 2008, "Superhydrophobic Properties of Nanostructured–Microstructured Porous Silicon for Improved Surface-Based Bioanalysis," NanoBiotechnology, **4**(1-4), pp. 18–27.

[101] Hu, H., and Larson, R. G., 2005, "Analysis of the effects of Marangoni stresses on the microflow in an evaporating sessile droplet," Langmuir, **21**(9), pp. 3972–3980.

[102] Ghasemi, H., and Ward, C. A., 2010, "Energy transport by thermocapillary convection during sessile-water-droplet evaporation," Phys. Rev. Lett., **105**(13), p. 136102.

[103] Ristenpart, W. D., Kim, P. G., Domingues, C., Wan, J., and Stone, H. A., 2007, "Influence of substrate conductivity on circulation reversal in evaporating drops," Phys. Rev. Lett., **99**(23), p. 234502.

[104] Yunker, P. J., Still, T., Lohr, M. A., and Yodh, A. G., 2011, "Suppression of the coffee-ring effect by shape-dependent capillary interactions," Nature, **476**(7360), pp. 308–311.

[105] Savino, R., and Fico, S., 2004, "Transient Marangoni convection in hanging evaporating drops," Phys. Fluids, **16**(10), pp. 3738–3754.

[106] Sefiane, K., and Ward, C. A., 2007, "Recent advances on thermocapillary flows and interfacial conditions during the evaporation of liquids," Adv. Colloid Interface Sci., **134–135**, pp. 201–223.

[107] Hu, H., and Larson, R. G., 2006, "Marangoni effect reverses coffee-ring depositions," J. Phys. Chem. B, **110**(14), pp. 7090–7094.

[108] Trouette, B., Chénier, E., Doumenc, F., Delcarte, C., and Guerrier, B., 2012, "Transient Rayleigh-Bénard-Marangoni solutal convection," Phys. Fluids, **24**(7), pp. 074108–074108–25.

[109] Selva, B., Daubersies, L., and Salmon, J.-B., 2012, "Solutal convection in confined geometries: enhancement of colloidal transport," Phys. Rev. Lett., **108**(19), p. 198303.

[110] Kang, K. H., Lee, S. J., Lee, C. M., and Kang, I. S., 2004, "Quantitative visualization of flow inside an evaporating droplet using the ray tracing method," Meas. Sci. Technol., **15**(6), pp. 1104–1112.

[111] Chamarthy, P., Dhavaleswarapu, H. K., Garimella, S. V., Murthy, J. Y., and Wereley, S. T., 2007, "Visualization of convection patterns near an evaporating meniscus using μPIV," Exp. Fluids, **44**(3), pp. 431–438.

[112] Squires, T. M., and Quake, S. R., 2005, "Microfluidics: fluid physics at the nanoliter scale," Rev. Mod. Phys., **77**(3), pp. 977–1026.

[113] Bringer, M. R., Gerdts, C. J., Song, H., Tice, J. D., and Ismagilov, R. F., 2004, "Microfluidic systems for chemical kinetics that rely on chaotic mixing in droplets," Philos. Trans. R. Soc. Lond. Ser. Math. Phys. Eng. Sci., **362**(1818), pp. 1087–1104.

[114] Rida, A., and Gijs, M. A. M., 2004, "Manipulation of self-assembled structures of magnetic beads for microfluidic mixing and assaying," Anal. Chem., **76**(21), pp. 6239–6246.

[115] Frommelt, T., Kostur, M., Wenzel-Schäfer, M., Talkner, P., Hänggi, P., and Wixforth, A., 2008, "Microfluidic mixing via acoustically driven chaotic advection," Phys. Rev. Lett., **100**(3), p. 034502.

[116] Dicuangco, M., Dash, S., Weibel, J. A., and Garimella, S. V., 2014, "Effect of superhydrophobic surface morphology on evaporative deposition patterns," Appl. Phys. Lett., **104**(20), p. 201604.

[117] Tam, D., von Arnim, V., McKinley, G. H., and Hosoi, A. E., 2009, "Marangoni convection in droplets on superhydrophobic surfaces," J. Fluid Mech., **624**, pp. 101–123.

[118] Dash, S., Kumari, N., and Garimella, S. V., 2012, "Frequency-dependent transient response of an oscillating electrically actuated droplet," J. Micromechanics Microengineering, **22**(7), p. 075004.

[119] Incorporation, M. W., 2007, "MATLAB user manual version 7.4. 0 (R2007a)," MathWorks Inc. Natick MA.

[120] Ren, H., Fair, R. B., Pollack, M. G., and Shaughnessy, E. J., 2002, "Dynamics of electro-wetting droplet transport," Sens. Actuators B Chem., **87**(1), pp. 201–206.

[121] Annapragada, S. R., Dash, S., Garimella, S. V., and Murthy, J. Y., 2011, "Dynamics of Droplet Motion under Electrowetting Actuation," Langmuir, **27**(13), pp. 8198–8204.

[122] Richard, D., Clanet, C., and Quéré, D., 2002, "Surface phenomena: Contact time of a bouncing drop," Nature, **417**(6891), p. 811.

[123] Wang, K. L., and Jones, T. B., 2005, "Electrowetting Dynamics of Microfluidic Actuation," Langmuir, **21**(9), pp. 4211–4217.

[124] Ko, S. H., Lee, S. J., and Kang, K. H., 2009, "A synthetic jet produced by electrowetting-driven bubble oscillations in aqueous solution," Appl. Phys. Lett., **94**, p. 194102.

[125] Oh, J. M., Ko, S. H., and Kang, K. H., 2008, "Shape Oscillation of a Drop in ac Electrowetting," Langmuir, **24**(15), pp. 8379–8386.

[126] Baret, J. C., Decre, M. M. ., and Mugele, F., 2007, "Self-excited drop oscillations in electrowetting," Langmuir, **23**(9), pp. 5173–5179.

[127] Jordan D W., and Smith P., 1977, Nonlinear ordinary differential equations Clarendon Press Oxford.

[128] Miles, J., and Henderson, D., 1990, "Parametrically forced surface waves," Annu. Rev. Fluid Mech., **22**(1), pp. 143–165.

[129] Noblin, X., Buguin, A., and Brochard-Wyart, F., 2009, "Vibrations of sessile drops," Eur. Phys. J.-Spec. Top., **166**(1), pp. 7–10.

[130] Lamb, H., 1932, "Hydrodynamics (6th ed)," Cambridge University Press: Cambridge UK.

[131] Lai, M. F., Lee, C. P., Liao, C. N., and Wei, Z. H., 2009, "Oscillation spectrums and beat phenomenon of a water droplet driven by electrowetting," Appl. Phys. Lett., **94**(15), p. 154102.

[132] Kim, H.-Y., 2004, "Drop fall-off from the vibrating ceiling," Physics of Fluids, **16**(2), pp. 474–477.

[133] Bhushan, B., and Chae Jung, Y., 2007, "Wetting study of patterned surfaces for superhydrophobicity," Ultramicroscopy, **107**(10-11), pp. 1033–1041.

[134] Patankar, N. A., 2004, "Transition between superhydrophobic states on rough surfaces," Langmuir, **20**(17), pp. 7097–7102.

[135] Okumura, K., Chevy, F., Richard, D., Quéré, D., and Clanet, C., 2003, "Water spring: A model for bouncing drops," EPL Europhys. Lett., **62**, p. 237.

[136] Li, X., Ma, X., and Lan, Z., 2010, "Dynamic Behavior of the Water Droplet Impact on a Textured Hydrophobic/Superhydrophobic Surface: The Effect of the Remaining Liquid Film Arising on the Pillars' Tops on the Contact Time," Langmuir, **26**(7), pp. 4831–4838.

[137] Dash, S., Alt, M. T., and Garimella, S. V., 2012, "Hybrid Surface Design for Robust Superhydrophobicity," Langmuir, **28**(25), pp. 9606–9615.

[138] Barbieri, L., Wagner, E., and Hoffmann, P., 2007, "Water wetting transition parameters of perfluorinated substrates with periodically distributed flat-top microscale obstacles," Langmuir, **23**(4), pp. 1723–1734.

[139] Liu, B., and Lange, F. F., 2006, "Pressure induced transition between superhydrophobic states: Configuration diagrams and effect of surface feature size," J. Colloid Interface Sci., **298**(2), pp. 899–909.

[140] Kwon, H. M., Paxson, A. T., Varanasi, K. K., and Patankar, N. A., 2011, "Rapid Deceleration-Driven Wetting Transition during Pendant Drop Deposition on Superhydrophobic Surfaces," Phys. Rev. Lett., **106**(3), p. 36102.

[141] Wu, J., Ma, R., Wang, Z., and Yao, S., 2011, "Do droplets always move following the wettability gradient?," Appl. Phys. Lett., **98**, p. 204104.

[142] Dash, S., and Garimella, S. V., 2013, "Droplet Evaporation Dynamics on a Superhydrophobic Surface with Negligible Hysteresis," Langmuir, **29**(34), pp. 10785–10795.

[143] Dash, S., and Garimella, S. V., 2014, "Droplet evaporation on heated hydrophobic and superhydrophobic surfaces," Phys. Rev. E, **89**(4), p. 042402.

[144] Incropera, F. P., and Dewitt, D. P., 2002, Fundamentals of Mass and Heat Transfer, New York: John Wiley & Sons.

[145] Girard, F., Antoni, M., Faure, S., and Steinchen, A., 2008, "Influence of heating temperature and relative humidity in the evaporation of pinned droplets," Colloids Surf. Physicochem. Eng. Asp., **323**(1–3), pp. 36–49.

[146] Nguyen, T. A. H., and Nguyen, A. V., 2012, "On the Lifetime of Evaporating Sessile Droplets," Langmuir, **28**(3), pp. 1924–1930.

[147] Marín, Á. G., Gelderblom, H., Lohse, D., and Snoeijer, J. H., 2011, "Order-to-disorder transition in ring-shaped colloidal stains," Phys. Rev. Lett., **107**(8), p. 085502.

[148] Pan, Z., Dash, S., Weibel, J. A., and Garimella, S. V., 2013, "Assessment of water droplet evaporation mechanisms on hydrophobic and superhydrophobic substrates," Langmuir, **29**(51), pp. 15831–15841.

[149] Pope, R. M., and Fry, E. S., 1997, "Absorption spectrum (380-700 nm) of pure water. II. Integrating cavity measurements," Appl. Opt., **36**(33), pp. 8710–8723.

[150] Minor, G., Oshkai, P., and Djilali, N., 2007, "Optical distortion correction for liquid droplet visualization using the ray tracing method: further considerations," Meas. Sci. Technol., **18**(11), pp. L23–L28.

[151] Gelderblom, H., Bloemen, O., and Snoeijer, J. H., 2012, "Stokes flow near the contact line of an evaporating drop," J. Fluid Mech., **709**, pp. 69–84.

[152] Xu, X., Luo, J., and Guo, D., 2010, "Criterion for reversal of thermal Marangoni flow in drying drops," Langmuir, **26**(3), pp. 1918–1922.

[153] Kang, K. H., Lim, H. C., Lee, H. W., and Lee, S. J., 2013, "Evaporation-induced saline Rayleigh convection inside a colloidal droplet," Phys. Fluids, **25**(4), p. 042001.

[154] Müller, G., Neumann, G., and Weber, W., 1984, "Natural convection in vertical Bridgman configurations," J. Cryst. Growth, **70**(1–2), pp. 78–93.

[155] Touihri, R., Hadid, H. B., and Henry, D., 1999, "On the onset of convective instabilities in cylindrical cavities heated from below. I. Pure thermal case," Phys. Fluids 1994-Present, **11**(8), pp. 2078–2088.

[156] Neumann, G., 1990, "Three-dimensional numerical simulation of buoyancy-driven convection in vertical cylinders heated from below," J. Fluid Mech., **214**, pp. 559–578.

[157] Culbertson, C. T., Jacobson, S. C., and Michael Ramsey, J., 2002, "Diffusion coefficient measurements in microfluidic devices," Talanta, **56**(2), pp. 365–373.

APPENDICES

Appendix A. Hierarchical Superhydrophobic Surfaces

Figure A.1 shows the different hierarchical superhydrophobic surfaces fabricated in using the single step methodology reported in Chapter 5.

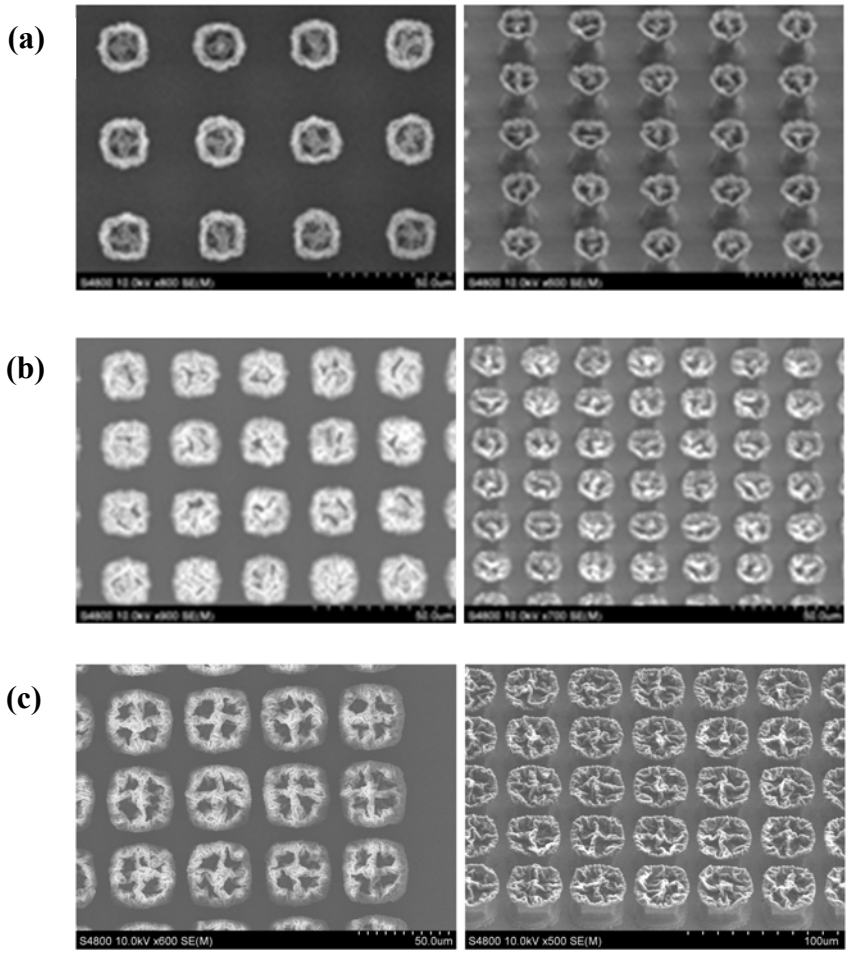

Figure A.1. Hierarchical superhydrophobic surfaces with (a) width 19.5 µm, pitch = 41 µm (b) width 17 µm, pitch = 27 µm (c) width 35.5 µm, pitch = 44 µm

Appendix B. Mathematica Algorithm to Determine Evaporation Flux at Droplet Interface using Vapor-Diffusion Model

```
ClearAll["Global`*"]
theta =160*Pi/180;     % Contact angle of droplet
Vol = 3;
R0=(3*Vol/(Pi*(1-Cos[theta])^2*(2+Cos[theta])))^1/3*10^-3//N;        % Radius of droplet
Cs = 1/57.3;              % Saturation concentration
Dif = 0.2541*10^-4;
H = 0.36;
delC = (1-H)*Cs
R = R0*(Sin[theta]);
hmax = N[R/Sin[theta]*(1-Cos[theta])];
Nu =500;
deltah = hmax/Nu;
htND = hmax/R;

csa[z_] :=Sin[theta]/z- Cos[theta]
r[z_] :=R*Sqrt[-z^2 +1-2z]  % Radial location on the droplet interface as a function of height
f[tau_]:=tau*Cosh[theta *tau]/Cosh[Pi *tau] *Tanh[tau*(Pi-theta)]
Jr[z_] :=
delC/(R/Dif)*(Sin[theta]/2+(√2*(csa[z]+Cos[theta])^3/2)*(NIntegrate[f[tau]*LegendreP[-
0.5+I*tau,csa[z]],{tau,0,20}]))          % Evaporation flux at the droplet interface as
function of corresponding height
J = {};
hND = {};
r1 = {};
csa1 = {};
J2={};
For[i = 1,i <=(Nu-1),i++,
          h = hmax-i*deltah;
          z = h/R;
          AppendTo[J,Re[Jr[z]]];
          AppendTo[r1,r[z]/R];
          AppendTo[hND,h/R];
          AppendTo[csa1,csa[z]];
    ]
dmbydtfin = Pi* R * Dif*delC*((Sin[theta]/(1+Cos[theta])) +
4*NIntegrate[(1+Cosh[2*theta*tau])/Sinh[2*Pi*tau]*Tanh[(Pi-theta)*tau],{tau,0,20}])
Mfunctionz=Re[NIntegrate[Jr[z]*R/Sin[theta]*(2 Pi )*R,{z,htND,0.0000001}]] % Evaporation rate
```

Appendix C. Matlab Code Implementing Conduction Heat Transfer through the Droplet

```
clear all; close all; clc;
Vol=2;   % in µL
theta = 150*pi/180;     % Contact angle
Rad = (3*Vol/pi/(1-cos (theta))^2/(2+ cos (theta)))^(1/3)*1e-3; % Radius of droplet (in m)
Rc = Rad*sin(theta);  %Contact radius of droplet (in m)
height = Rad-Rad*cos(theta);  %height of the droplet in m
V0 = Vol*1e-9; %in m3
h0 = height ; %(ht in m)
Tot_SurfAr = 2*pi*(Rad)*h0;

R = 8.3145; %J/mol.K
M =0.018 ;  %kg/mol

H = 0.36; N = 500; % number of discretization

Tamb = 24  + 273.15;
Tref = 300;  %in K
% Tref = 315;
Tsub = 40 + 273.15;
Dref = 2.6262e-005; %diffusion coeff at 300K
% Dref = 2.8256e-005; % diffusion coeff at 315 K
Psat_ref = 0.03531*10^5; %Psat at 300K in Pascal
% Psat_ref = 0.08132*10^5;   %Psat at 315K in Pascal
kliq = 0.58;      %conductivity of water

%% Reading the functional dependence on CA of Flux from the excel sheet containing
evaporation flux at the droplet interface corresponding to a particular contact angle

Jre = xlsread('f_theta_in_expression_J_r',2, 'c6:c504');  %for 150 deg CA
% Jre = xlsread('f_theta_in_expression_J_r',3, 'c6:c504'); %for 110 deg CA,

deltah = h0/500;

h_r(:,1) = h0 - (1:499)*deltah;
r = real(sqrt(-h_r.^2 + Rc.^2 - 2*h_r.*Rc./tan(theta)));

% Parameters at ambient conditions
hfg_Ta= 2.7554*10^6 - 3.46*Tamb^2;          % latent heat
```

```
Psat_Ta = Psat_ref*exp(M*hfg_Ta/R*(1/Tref - 1/Tamb)); % saturation pressure
Cs_Ta = Psat_Ta/(R*Tamb) * M;      % saturated concentration at Ta
Damb = Dref.*(Tamb/Tref)^(3/2);     % diffusion coefficient

% Parameters at substrate temperature
hfg_Tsub = 2.7554*10^6 - 3.46.*(Tsub)^2; %J/kg
Psat_Tsub = Psat_ref*exp(M*hfg_Tsub/R*(1/Tref - 1/Tsub));
Cs_Tsub = Psat_Tsub/(R*Tsub) * M;
Dsub = Dref.*(Tsub/Tref)^(3/2);

J_diff = Jre*(Cs_Tsub - H*Cs_Ta)/(Rc/Dsub);
r(N) = Rc; h_r(N) = 0;

%% calculating stripe area
delS(1:500) = Tot_SurfAr/N;  % since delS is equal for same thickness strips on spherical
cap
area_ratio = sum(delS)/(2*pi*Rad*h0);

T(1:N) = Tsub;  %Initializing temperature

%% Iterations
delT = 100; n=0;
for n = 1:1000000
        n = n+1

        D(1) = Dref*(T(1)/Tref)^(3/2);
        hfg(1) = 2.7554*10^6 - 3.46.*(T(1))^2; %J/kg
        Psat(1) = Psat_ref*exp(M*hfg(1)/R*(1/Tref - 1/T(1)));
        Cs_Ti(1) = Psat(1)/(R*T(1)) * M ; % vap molar conc * vap mol. wt

        delC(1) = Cs_Ti(1) - H*Cs_Ta;
        J(1) = Jre(1)* delC(1)/(Rc/D(1));
        S = J(1) *delS(1)*hfg(1);
        Ab(1) = pi*(r(1))^2;
        J(1) = Jre(1)* delC(1)/(Rc/D(1));
        h_top = h_r(1)+deltah/2;
        h_bot = h_r(1)-deltah/2;
        r_top = real(sqrt(-h_top^2 + Rc^2 - 2*h_top*Rc/tan(theta)));
        r_bot = real(sqrt(-h_bot^2 + Rc^2 - 2*h_bot*Rc/tan(theta)));
        A_top(1) = pi*r_top^2;
        A_bot(1) = pi*r_bot^2;

        T(1) = T(2) - S*deltah/(kliq*A_bot(1));
        for i = 2: N-1
```

```
                D(i) = Dref*(T(i)/Tref)^(3/2);
                hfg(i) = 2.7554*10^6 - 3.46.*(T(i))^2; %J/kg
                Psat(i) = Psat_ref*exp(M*hfg(i)/R*(1/Tref - 1/T(i)));
                Cs_Ti(i) = Psat(i)/(R*T(i)) * M ; % vap molar conc * vap mol. wt
                delC(i) = Cs_Ti(i) - H*Cs_Ta;
                J(i) = Jre(i)* delC(i)/(Rc/D(i));
                S(i) = J(i) *delS(i)*hfg(i);
                h_top = h_r(i)+deltah/2;
                h_bot = h_r(i)-deltah/2;
                r_top = real(sqrt(-h_top^2 + Rc^2 - 2*h_top*Rc/tan(theta)));
                r_bot = real(sqrt(-h_bot^2 + Rc^2 - 2*h_bot*Rc/tan(theta)));

                A_top(i) = pi*r_top^2;
                A_bot(i) = pi*r_bot^2;

                T(i) = (T(i-1)*A_top(i) + T(i+1)*A_bot(i))/(A_top(i)+A_bot(i)) -
                S(i)*deltah/(kliq*(A_top(i)+A_bot(i)));

        end

        T(N) = Tsub; hfg(N) = hfg_Tsub; J(N)= 0; h_r(N) = 0; Ab(N) = pi*(r(N))^2 ;
end

r(N) = Rc; J_diff(N)= J_diff(N-1);
figure (2); plot(r/Rad,T-273.15)
figure (3); plot(r/Rad, J_diff,'r'); hold on; plot(r/Rad, J)

sum1 = 0;
for i = 1: N
        sum1 = sum1 + T(i)*delS(i);
end
Ti_avg = sum1/sum(delS);

hfg_Ti_avg = 2.7554*10^6 - 3.46.*(Ti_avg)^2; %J/kg
Psat_Ti_avg = Psat_ref*exp(M*hfg_Ti_avg/R*(1/Tref - 1/Ti_avg));
Cs_Ti_avg = Psat_Ti_avg/(R*Ti_avg) * M;
D_Ti_avg = Dref.*(Ti_avg/Tref)^(3/2);
delC_diff = (Cs_Tsub - H*Cs_Ta);
delC_Ti_avg = Cs_Ti_avg - H*Cs_Ta;

Ratio = (D_Ti_avg*delC_Ti_avg)/(Dsub*delC_diff)
```

Appendix D. Numerical Diffusion Model for Droplet Evaporation

In this section, a numerical model (using software package ANSYS 12.0 (FLUENT solver)) to help understand the evaporation mechanism is presented. The model was developed with the help of Dr. Zhenhai Pan. This is addition to the simple diffusion model assuming parallel control volume described in Chapter 6. In this model, the assumptions are: (1) the convection in both the liquid and gas phases may be ignored; (2) the silicon substrate remains at ambient temperature since the thermal conductivity of the silicon substrate is much higher than both the structured layer and the liquid droplet; and (3) the temperature is continuous across all interfaces. With the first assumption, the energy equation in the droplet, gas phase and structured layer is described by $\nabla^2 T = 0$, and the resulting evaporation flux is given in Eq. (6.1). An isothermal boundary condition is assumed at the bottom of the structured layer (T = 20.5°C). The third assumption leads to the same temperature on both sides of the droplet-gas interface and droplet-substrate interface, and the latent heat for evaporation is supplied from both the liquid and the gas side. At the outer boundary of the gas domain (200 times the droplet radius (R) away from the droplet interface), T = 20.5°C. The evaporation results in a heat sink at the droplet interface. To model the heat sink at the evaporating interface, a heat source (S_h) is added to the mesh cells adjacent to the liquid side of the interface

$$S_h = \frac{q(r) A_{cell}}{V_{cell,g}}. \tag{A.1}$$

where $q(r)$ is the heat flux absorbed at the interface, A_{cell} is the interface area of a specified cell adjacent to the interface, and V_{cell} is the cell volume. The heat flux absorbed by the interface, $q(r)$ is given as

$$q(r) = h_{fg} \cdot J(r). \tag{A.2}$$

where h_{fg} is the latent heat (h_{fg} = 2.46×10^6 J/kg at 20.5°C for water) and $J(r)$ is the evaporation flux (as given by Eq. (6.1)).

The thermal diffusion model is solved by employing the software package ANSYS 12.0 (FLUENT solver). The mesh is shown in Figure D.1. A total of 81080 (for the hydrophobic substrate) or 108440 (for the superhydrophobic substrate) quadrilateral cells are used across the computational domain. The mesh is locally refined at the liquid-gas interface. A mesh-independence check was performed to confirm that the simulation results are insensitive to further refinement of the mesh. The variation of the interfacial temperature is smaller than 0.5% for a mesh with twice as many cells for each case. A hemispherical simulation boundary is selected for the gas domain as shown in Figure D.1. The distance from the droplet to the outer boundary is 200 times the droplet radius; the interfacial temperature was confirmed to be independent of the boundary location for this domain size.

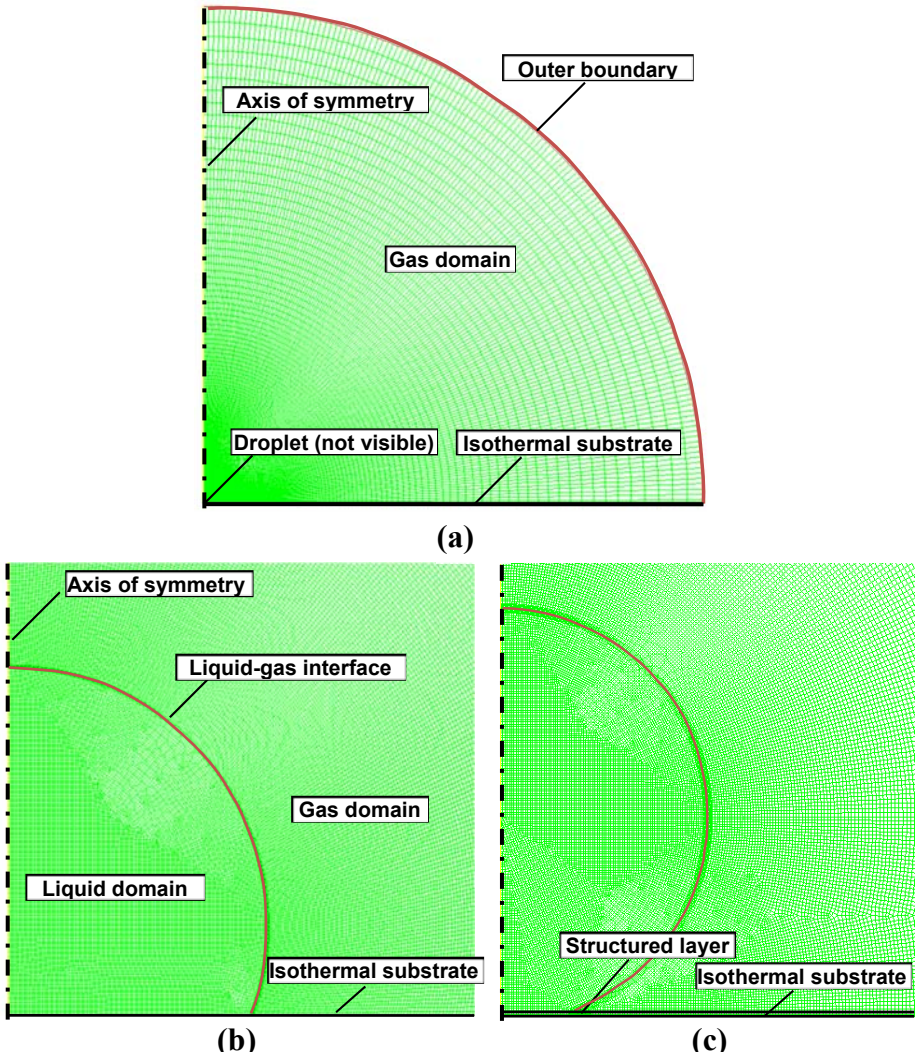

Figure D. 1. Schematic diagram of the numerical simulation domains and boundary conditions (with mesh overlay) for (a) the full domain; (b) detailed view near the droplet on a hydrophobic substrate; (c) detailed view near the droplet on a superhydrophobic substrate.

The computed temperature fields around a 2 μL droplet with different substrates are shown in Figure D.2. The calculated temperature distribution along the droplet interface is shown in Figure D.3. A large temperature drop is induced along the droplet interface by the evaporative cooling effect for the superhydrophobic substrate. The area-weighted average interfacial temperature of the droplet is 15.55°C, which is ~ 5°C lower than the

ambient temperature. The saturation pressure $p_{sat}\,(T_{lv})$ is calculated from the Clausius-Clapeyron equation:

$$p_{sat}(T_{lv}) = p_{sat\_ref} \exp\left(\frac{Mh_{fg}}{R}\left(\frac{1}{T_{sat\_ref}} - \frac{1}{T_{lv}}\right)\right) \tag{A.3}$$

The saturated vapor density at the evaporating interface (c_s) decreases by ~ 27.8%, leading to a reduced rate of evaporation. Therefore, the assumption of uniform temperature throughout the system in the diffusion-only model is not applicable to a superhydrophobic substrate and the evaporation rate is significantly over-estimated.

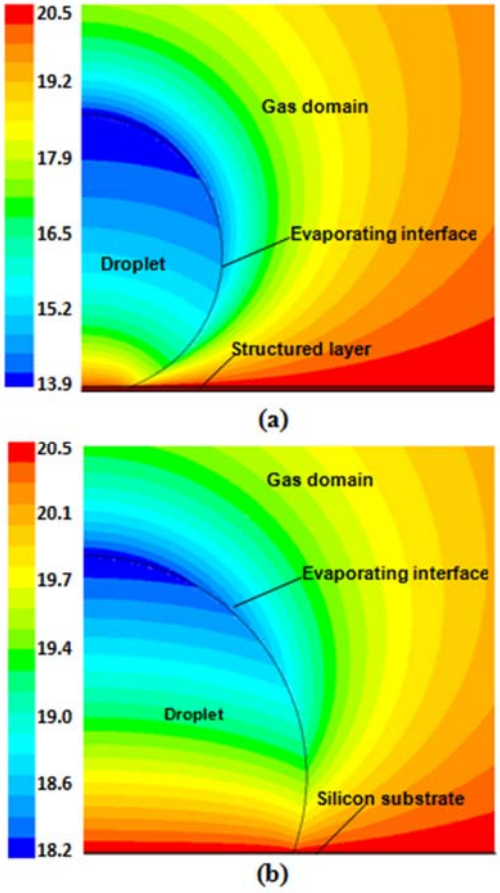

Figure D. 2. Temperature field in and around an evaporating 2 μL droplet resting on: (a) the structured superhydrophobic substrate (θ = 160 deg); and (b) the smooth hydrophobic substrate (θ = 110 deg). The color legend on the left indicates the calculated temperature in °C (the scale is different for the two cases).

A significant temperature drop occurs along the height of the evaporating droplet (~ 6.7°C) while the temperature drop across the structured layer is ~ 0.5°C, which means that the thermal resistance of the droplet is the primary factor contributing to the high evaporative cooling effect for a superhydrophobic surface. This result is not surprising because although the structured layer has a thermal conductivity (~ 0.54 *W/mK*) comparable to that of water, it has a much smaller thickness (~ 23 μm) compared to the water droplet (h ~ 1.7 mm). If the structured layer were removed, *i.e.* the bottom of the droplet was held isothermal at 20.5°C, the suppression of the saturated vapor density at the evaporating interface (c_s) reduces slightly from ~ 27.8% to ~ 24.4%.

The temperature distribution along the evaporating interface is found to be dependent on CA of the droplet, and independent of droplet volume (Figure D.3). This behavior can be explained using a simple scaling analysis. The evaporation flux, $q(r)$, and the corresponding cooling flux along the droplet interface, are inversely proportional to the droplet contact radius (Eq. (6.1)). The temperature drop across the droplet, $\Delta T \sim \left(\frac{h}{k_{liq}}\right) q(r) \sim \frac{h}{R_c} f_1(\theta) \sim \frac{1-\cos(\theta)}{\sin(\theta)} f_1(\theta)$ (k_{liq} is the thermal conductivity of the droplet and $f_1(\theta)$ represents the functional dependence of evaporation flux on CA), is independent of the length scale (or volume for fixed CA) of the droplet. This explains why a single correction factor 0.8 in Eq. (6.16) could be employed to account for the evaporative suppression in almost all the experimental cases on the superhydrophobic surface.

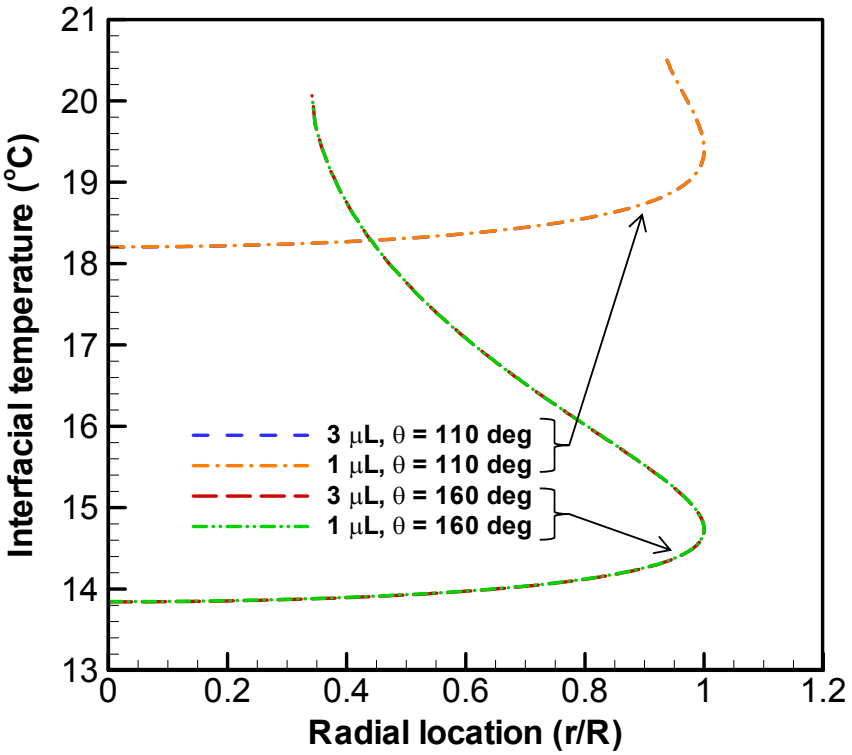

Figure D. 3. Interfacial droplet temperature for both hydrophobic (θ = 110 deg) and superhydrophobic substrate (θ = 160 deg). The radial location (r) is normalized by the droplet radius (R).

For a smooth hydrophobic substrate, the temperature drop across the droplet is much smaller. The average interfacial temperature is 19.01°C and the saturated vapor density at the evaporating interface is suppressed by ~ 8.9%. It should be noted that in the present analysis, the convection in both liquid and gas phases, which usually increases the evaporation rate, was neglected. The weak suppression of the evaporation by the cooling effect in case of a smooth hydrophobic surface could be partly compensated by the fluid convection on either side of the evaporating interface. Ongoing research efforts are targeted at full-scale modeling of the evaporation, including the evaporative cooling

effect, thermal conduction of the underlying substrate, and fluid flows in the droplet and surrounding air domains

Appendix E. Matlab Code to Correct Vector Distortion Due to Lens Effect of the Droplet

```
f = uigetfile('.dat');

%% Droplet Parameters

fid = fopen(f, 'rt');
A = textscan(fid, '%f', 'HeaderLines', 3);

M=4;          % Number of columns in the original file
scale = 3.86e-03;   % millimeters to pixels correction
vector_scale = 10;

N = length(A{1,1})./M;
B = reshape(A{1,1}, M, N);
C = transpose(B);

%% User Input (Contact radius, height, coordinates of the center of the droplet base line
obtained from experimental images)

R = 108.5;                    % in pixels % Contact radius
h = 376;                 % in pixels
y_0 = 702;      %pixel distance from the top of the image to the bottom of droplet
x_0 = 513.5;

na = 1;
nd = 1.33;
filename = 'Enter File Name containing Corrected Vectors';
%% PIV Data

b = h-R;                              %in pixels
x = C(:,1)/scale;                     % in pixels
x = x - x_0;
y = C(:,2)/scale;
y = y_0-y;
u_old = C(:,3)/(scale/1000);          %convert m/s to pixel/s ((m/s*pixel/mm)/1000)
v_old = -C(:,4)/(scale/1000);
r = 1/2*(R+sqrt(R^2+4*b.*y));
z = sqrt(r.^2 - x.^2-y.^2);

%% Delete Points Outside Droplet
```

```
u_old(imag(z)~=0)  = 0;
v_old(imag(z)~=0)  = 0;

Nu = sqrt(x.^2+(y-h/2).^2);
u_old(Nu > 0.95*h/2) = 0;
v_old(Nu > 0.95*h/2) = 0;

%% Ray Tracing

sintheta = sqrt(x.^2+z.^2)./r; costheta = y./r;
sinphi = x./sqrt(x.^2+z.^2);  cosphi = z./sqrt(x.^2+z.^2);
f = 1./sqrt(((r+b.*costheta).^2.*(sintheta.*sinphi).^2) + ((r.*costheta-b.*sintheta.^2).^2));

psia = acos((r+b.*costheta).*sintheta.*cosphi./sqrt(r.^2 + b.^2 *sintheta.^2)); %angle of
incidence
psid = asin(na/nd*sin(psia));                          %Snell's Law

Bx = -f.*tan(psia-psid).*(r+b.*costheta).*sintheta.*sinphi;
By = -f.*tan(psia-psid).*(r.*costheta-b.*sintheta.^2);
Bz = -1;

dBxdx =diff(Bx, x);          %partial differential of Bx with respect to x. The command
                             requires a symbolic toolbox
dBxdy=diff(Bx, y);

%% New Velocity and Position

corr_u = u_old.*dBxdx + v_old.*dBxdy;
corr_v = u_old.*dBydx + v_old.*dBydy;

u_new = u_old + corr_u;
v_new = v_old + corr_v;

x_new = x;
y_new = y;
x_new((Nu <= 0.95*h/2)) = x((Nu <= 0.95*h/2))-z((Nu <= 0.95*h/2)).*Bx((Nu <=
0.95*h/2))/Bz;
y_new((Nu <= 0.95*h/2)) = y((Nu <= 0.95*h/2))-z((Nu <= 0.95*h/2)).*By((Nu <=
0.95*h/2))/Bz;
x_new(y<0) = x(y<0);
y_new(y<0) = y(y<0);

%% Convert back to meters
x_new = scale*x_new;
y_new = scale*y_new;
```

```
u_new = scale*u_new;
v_new = scale*v_new;
x = scale*x;
y = scale*y;
u_old = scale*u_old;
v_old = scale*v_old;
corr_u = scale*corr_u;
corr_v = scale*corr_v;
magnitude_old = sqrt(u_old.^2 + v_old.^2);
magnitude = sqrt(u_new.^2+v_new.^2);
velocity = [u_new,v_new];

% %% Comparison of magnitudes.
%% Droplet Boundary
theta = -90:0.01:90;
r = R+b*cosd(theta);
yr = r.*cosd(theta)*scale;
xr = r.*sind(theta)*scale;

%% Plotting Comparison
figure(1)
quiver(x_new,y_new,u_new,v_new);
hold on;
plot(xr, yr, 'k');
axis equal;

figure(2)
quiver(x,y,u_old, v_old, 'r');
hold on;
plot(xr, yr, 'k');
% contourf(x,y,sqrt(u_old.^2+v_old.^2));
axis equal;

%% Output Data File
fid = fopen(filename, 'wt');
fprintf(fid,'x_old[mm] \t y_old[mm] \t u_old[mm/s] \t v_old[mm/s] \t x_new[mm] \t
y_new[mm] \t u_new[mm/s] \t v_new[mm/s]\n');
for i = 1:length(x_new)
    fprintf(fid, '%0+7.7f \t %0+7.7f \t %0+7.7f \t %0+7.7f \t %0+7.7f \t %0+7.7f
\t %0+7.7f \t %0+7.7f \n', x(i), y(i), u_old(i), v_old(i),  x_new(i), y_new(i), u_new(i),
v_new(i));
end
fclose(fid);
dlmwrite(filename, [], '-append', 'delimiter',',')
```

VITA

VITA

Susmita Dash
Graduate School, Purdue University

Susmita Dash received a Bachelor of Technology in Mechanical Engineering from National Institute of Technology, Rourkela, India in 2008. Following her graduation, she worked for a year at Schlumberger, India as a Mechanical Engineer. She is currently pursuing her Ph.D. in the School of Mechanical Engineering at Purdue University under the advisement of Prof. Suresh V. Garimella. The primary area of her doctoral research is to explore the interdependence between surface morphology and interfacial interaction mechanisms. This includes tailoring robust bio-inspired superhydrophobic surfaces at micro- and nano-scales for specific applications, as well as studying fluid dynamics and phase-change characteristics of liquids on textured surfaces. She is a recipient of the Ross Doctoral Fellowship, 2009 – 2010, and Bilsland Dissertation Fellowship, 2013 – 2014, at Purdue University. She received the 2012 EPPD Student Member of the Year award from the Electronic and Photonic Packaging Division of the ASME, and 2013 Outstanding Graduate Student Research Award at Purdue University.

PUBLICATIONS

PUBLICATIONS

1. **Dash, S.**, and Garimella, S. V., 2014, "Droplet evaporation on heated hydrophobic and superhydrophobic surfaces," Phys. Rev. E, **89**(4), p. 042402.
2. Dicuangco, M., **Dash, S.**, Weibel, J. A., and Garimella, S. V., 2014, "Effect of superhydrophobic surface morphology on evaporative deposition patterns," Appl. Phys. Lett., **104**(20), p. 201604.
3. **Dash, S.**, Chandramohan A., Weibel J A and Garimella S V, 2014, "Efficient On-the-Spot Mixing in Droplets Evaporating on Non-Wetting Surfaces," (submitted).
4. **Dash, S.**, and Garimella, S. V., 2013, "Droplet Evaporation Dynamics on a Superhydrophobic Surface with Negligible Hysteresis," Langmuir, **29**(34), pp. 10785–10795.
5. Pan, Z., **Dash, S.**, Weibel, J. A., and Garimella, S. V., 2013, "Assessment of Water Droplet Evaporation Mechanisms on Hydrophobic and Superhydrophobic Substrates," Langmuir, **29**(51), pp. 15831–15841.
6. Ebrahimi, A., Dak, P., Salm, E., **Dash, S.**, Garimella, S. V., Bashir, R., and Alam, M. A., 2013, "Nanotextured superhydrophobic electrodes enable detection of attomolar-scale DNA concentration within a droplet by non-faradaic impedance spectroscopy," Lab. Chip, **13**(21), p. 4248.
7. **Dash, S.**, Alt, M. T., and Garimella, S. V., 2012, "Hybrid Surface Design for Robust Superhydrophobicity," Langmuir, **28**(25), pp. 9606–9615.

8. **Dash, S.**, Kumari, N., and Garimella, S. V., 2012, "Frequency-dependent transient response of an oscillating electrically actuated droplet," J. Micromechanics Microengineering, **22**(7), p. 075004.
9. **Dash, S.**, Kumari, N., and Garimella, S. V., 2011, "Characterization of ultrahydrophobic hierarchical surfaces fabricated using a single-step fabrication methodology," J. Micromechanics Microengineering, **21**, p. 105012.
10. Annapragada, S. R., **Dash, S.**, Garimella, S. V., and Murthy, J. Y., 2011, "Dynamics of Droplet Motion under Electrowetting Actuation," Langmuir, **27**(13), pp. 8198–8204.
11. **Dash, S**., Chandramohan, A., Weibel, J. A., and Garimella, S. V., 2014, "Visualization of Buoyant Convection in Droplets on Superhydrophobic Surfaces," 67th Annual Meeting of the APS Divison of Fluid Dynamics, San Francisco, California, November 23-25, 2014.
12. **Dash, S.**, Chandramohan, A., and Garimella, S. V., 2014, "Flow Visualization of Droplet Evaporation on Hydrophobic and Superhydrophobic Surfaces," J. Heat Transfer, **136**, p. 080917 (Photogallery).
13. Dicuangco, M., **Dash, S.** and Garimella, S. V., 2013, "Evaporative Deposition on Superhydrophobic Surfaces," J. Heat Transfer, **135**, p. 080904 (Photogallery).
14. **Dash, S.**, Chandramohan, A., Weibel, J. A., and Garimella, S. V., "Flow Visualization of Droplet Evaporation on Hydrophobic and Superhydrophobic Surfaces," Proceedings of the ASME 2013 International Mechanical Engineering Congress & Exposition IMECE2013, San Diego, California, November 13-21, 2013 (Photogallery entry).
15. **Dash, S.**, Chandramohan, A., Weibel, J. A., and Garimella, S. V., "Flow Visualization of Droplet Evaporation on a Hydrophobic Surface," Proceedings of the ASME 2013 International Mechanical Engineering Congress & Exposition IMECE2013, San Diego, California, November 13-21, 2013 (Poster).
16. Dicuangco, M., **Dash, S.**, Weibel, J. A., and Garimella, S. V., "Evaporative Solute Deposition on Superhydrophobic Surfaces," IMECE2013-63928, Proceedings of the

ASME 2013 International Mechanical Engineering Congress & Exposition IMECE2013, San Diego, California, November 13-21, 2013.

17. Pan, Z., **Dash, S.**, Weibel, J. A. and Garimella, S. V., "Numerical Study of Water Droplet Evaporation on a Superhydrophobic Surface," HT2013-17697, Proceedings of the ASME 2013 Summer Heat Transfer Conference, MN, 2013.
18. Annapragada, S. R., **Dash, S.**, Garimella, S. V., and Murthy, J. Y., "Dynamics of Droplet Motion under Electrowetting Actuation," InterPACK2011-52061, Proceedings of the ASME 2011 Pacific Rim Technical Conference & Exposition on Packaging and Integration of Electronic and Photonic System, Portland, Oregon, July 6-8, 2011.
19. Dash, S., Kumari, N., Dicuangco, M., and Garimella, S. V., "Single-Step Fabrication and Characterization of Ultrahydrophobic Surfaces with Hierarchical Roughness," InterPACK2011-52046, Proceedings of the ASME 2011 Pacific Rim Technical Conference & Exposition on Packaging and Integration of Electronic and Photonic Systems, Portland, Oregon, July 6-8, 2011.